Indirect conversion amorphous selenium photodetectors for medical imaging applications

by

Shiva Abbaszadeh

A thesis

presented to the University of Waterloo

in fulfillment of the

thesis requirement for the degree of

Doctor of Philosophy

in

Electrical and Computer Engineering

Waterloo, Ontario, Canada, 2014

© Shiva Abbaszadeh 2014

AUTHOR'S DECLARATION

I hereby declare that I am the sole author of this thesis. This is a true copy of the thesis, including any required final revisions, as accepted by my examiners.

I understand that my thesis may be made electronically available to the public.

Abstract

The innovative design of flat panel volume computed tomography (CT) systems has recently led to the emergence of a wide spectrum of new applications for both diagnostic and interventional purposes, such as ultra-high resolution bone imaging, image guided interventions, dynamic CT angiography, and interventional neuroradiology. Most of these applications require low X-ray dose to limit potential harm to the patient. One of the main challenges of low dose imaging is to maintain a quantum noise limited system to achieve the highest possible signal to noise ratio (SNR) at a given dose. One potential method to achieve a quantum noise limited system is to employ a high gain detector. Current flat panel CT technology is based on indirect conversion detectors that contain a scintillator and hydrogenated amorphous silicon (a-Si:H) p-i-n photodetectors which have a gain below unity and require a specialized p-layer.

In this thesis, an alternative detector to the p-i-n photodetector, which can achieve gain above unity and thus aid in achieving quantum noise limited systems is investigated for large area flat panel imaging. The proposed detector is based on amorphous selenium (a-Se). Amorphous selenium is the most highly developed photoconductor for large area direct conversion X-ray imaging and is still the only commercially available large area direct conversion flat panel X-ray detector. However, the use of a-Se for indirect conversion imaging has not been significantly explored. Amorphous selenium has field dependent mobility and conversion efficiency, which increase with increasing electric field. It is also the only large area compatible avalanche-capable material; a property that was discovered more than 30 years ago. This unique property could be leveraged to provide the gain necessary for low dose medical imaging applications.

The only current commercial avalanche capable a-Se optical detector uses electron beam readout in vacuum, which is not large area compatible and makes integration with pixelated readout electronics challenging. The detector structure proposed in this research seeks to address the challenges associated with integration of an avalanche capable a-Se detector with large area X-ray imager. One important aspect in the development of a-Se avalanche detectors is reducing the dark current and preventing a-Se breakdown as the electric field across the device is increased. A high dark current reduces the dynamic range of the detector, it increases the noise level, and it can lead to crystallization of the detector due to joule heating. To overcome the dark current problem, different blocking layers that allow for integration with large area flat panel imagers were investigated. Experimental results from fabricated devices provided the basis for the choice of the most suitable

blocking layer. Two device structures are proposed using the selected blocking layer, a vertical structure and a lateral structure, each having associated benefits and drawbacks. It was shown that introducing a polyimide blocking layer brought down the dark current more than four orders of magnitude at high electric fields and does not deteriorate the charge transport properties of the detectors. The polyimide blocking layer also greatly minimizes physical stress related crystallization in a-Se improving reliability. Gain above unity was observed in the vertical structure and the initiation of impact ionization was verified by performing time-of-flight experiments. Although impact ionization was not verified in the lateral structure, this device structure was found to be highly sensitive to ultraviolet light due to the absence of a top contact layer. Devices were fabricated on several different substrates, including a CMOS substrate, to demonstrate their integration compatibility with large area readout electronics. The exhibited performance of the vertical device structure demonstrates that it is a suitable alternative to the p-i-n photodetector for low dose imaging applications.

Acknowledgements

First of all, I would like to express my sincere gratitude to my supervisor, Dr. Karim S. Karim, for his non-stop support, for pointing me in the right direction, for letting me explore my ideas, and for always being there for me. Dr. Karim has been an excellent mentor and he helped me to accomplish many achievements throughout my PhD.

I have a lack of vocabulary for thanking Dr. Vassili Karanassios for his unconditional support. My collaboration with Dr. Vassili was one of the best times of my PhD. He was always there for me to discuss all of my new ideas, to encourage me, and to cheer me up. He truly is a good role model and always has many insightful comments and suggestions.

I would like to express the deepest appreciation to my committee members, Dr. Bo Cui, Dr. John Yeow, Dr. John Boone, and especially Dr. Hany Aziz who always supported me and was very generous with his time for discussions related to my project.

I would like to thank Dr. Alla Reznik and Dr. John Rowlands for hosting me at the Thunder Bay Regional Research Institute (TBRRI) to conduct various experiments, and for their guidance and advice. Thanks also go to Dr. Bernard Weinstein and Dr. Safa Kasap and their students for running specialized experiments on several fabricated devices. Special thanks go to Richard Barber and Robert Mullins for helping with G2N lab maintenance. Truly, without them this work would not have been possible. I would like to thank all G2N lab members, especially Jian Zhang and Graeme Williams, for their help in the lab.

I would like to thank all members of the Silicon Thin-Film Applied Research (STAR) group, past and present, for their friendship and advice and for always bringing a smile to my face. Special thanks go to Dr. Kai Wang, Dr. Feng Chen, and Dr. Michael Adachi for training me in the G2N lab. I am grateful to Sina Ghanbarzadeh and Chris Scott for all the late night work in the G2N lab and helping me with the DALSA project.

Many thanks go to my officemates Melissa Chow for good company and Ryan Mann for all his positive energy. Thanks also go to Anita, Bita, and James for their friendship and support.

Lastly and most importantly, I thank my parents for their unconditional love and support and thank my husband, who never complained about me talking non-stop about my project, who always encouraged me, believed in my ability, and was always there for me. Nick you are the best.

Dedication

This thesis is dedicated to my parents, Farah and Abbas, and Nick for their ongoing love and support.

Table of Contents

AUTHOR'S DECLARATION ii
Abstract iii
Acknowledgements v
Dedication vi
Table of Contents vii
List of Figures x
List of Tables xv
Chapter 1 Introduction 1
1.1 X-ray Detection 1
1.2 Direct vs. indirect conversion 2
1.2.1 Direct conversion photoconductor 3
1.2.2 Indirect conversion scintillator 4
1.2.3 Indirect conversion photodetector 6
1.3 Medical imaging modalities 7
1.4 Thesis organization 10
Chapter 2 Amorphous selenium as a photoconductor 13
2.1 Introduction 13
2.2 Photogeneration efficiency 13
2.3 Dark current 16
2.4 Charge transport 19
2.5 Temporal response 21
2.6 Avalanche in amorphous selenium 22
Chapter 3 Fabrication and characterization of a-Se films 25
3.1 Introduction 25
3.2 Substrates and substrate preparation 25
3.3 Deposition of a-Se 26
3.4 Characterization of amorphous selenium film 27
3.4.1 X-ray Diffraction (XRD) 27
3.4.2 Electrical properties of a-Se 28
Chapter 4 Development of high conversion gain a-Se photodetectors: Blocking contacts 31

4.1 Introduction 31
4.2 Methods and materials 32
4.3 Results 36
4.4 Conclusion 40
Chapter 5 Development of high conversion gain a-Se photodetectors: Vertical structure 41
5.1 Introduction 41
5.2 Experimental details 42
5.3 Photoresponse 44
5.4 Transient response 47
5.5 Linearity 49
5.6 TOF measurement 49
5.7 Vertical a-Se structure on CMOS substrates 52
5.8 Conclusion 54
Chapter 6 Development of high conversion gain a-Se photodetectors: Lateral structure 55
6.1 Introduction 55
6.2 Methods 56
6.3 Dark current 60
6.4 Photoresponse 61
6.5 Comparison of lateral and vertical structures 66
6.6 Lateral a-Se structure on flexible substrates 69
6.7 Conclusion 71
Chapter 7 Development of high conversion gain a-Se photodetectors: Stability 72
7.1 Introduction 72
7.2 Experimental details 74
7.3 Results 76
7.3.1 Photo-induced darkening 76
7.3.2 Photo-induced crystallization 80
7.4 Conclusion 81
Chapter 8 UV detection of microplasma emission by a lateral a-Se based detector 82
8.1 Introduction 82
8.2 Experimental 83
8.3 Results and discussion 85

8.3.1 Spectral response 85
8.3.2 Signal response 86
8.4 Conclusion 88
Chapter 9 Summary, contribution, and future considerations 89
9.1 Summary 89
9.2 Contributions 90
9.3 Future considerations 91
Appendix A Onsager formulation 93
Appendix B Calculating electric field when charge accumulates at PI/a-Se interface 95
Appendix C Additional notes for electric field simulation 98
References 100

List of Figures

Figure 1: Radiographic image acquisition. 1
Figure 2: Cross-sectional view of (left) direct conversion detector, (right) indirect conversion detector [2]. 2
Figure 3: Avalanche multiplication process for (left) αe ≅ αh, and (right) αe ≫ αh. 7
Figure 4: Schematic of a third generation CT scanner [23]. 9
Figure 5: The experimental photogeneration efficiency of holes in a-Se versus applied electric field with different light wavelengths [34]. 14
Figure 6: Photogeneration efficiency as a function of applied field for blue (468 nm) and green (520 nm) wavelengths. Obtained using Onsager theory formalism as outlined in [34]. The X-ray photogeneration efficiency of a-Se is also shown (empirical equation obtained from [37] indicating that operating at higher electric fields is also beneficial for direct X-ray imaging).... 15
Figure 7: The current density 3000 s after applying 2000 V (across 500 µm thick selenium) plotted against the work function of the metal used for the electrode [43]. 18
Figure 8: Images that demonstrate the appearance of lag and ghosting after an exposure of a circular region. 22
Figure 9: Schematic of HARP camera structure [56]. 23
Figure 10: Selenium evaporator in G2N lab (left); the evaporation assembly inside the vacuum chamber (right). 26
Figure 11: XRD pattern of a-Se obtained under ambient condition. Inset from [68] for comparison. 28
Figure 12: Field dependence of electron mobility for samples deposited at two different temperatures. 29
Figure 13: Field dependence of hole mobility for samples deposited at two different temperatures. . 29
Figure 14: Fraction of recovered electron signal vs. interruption time from samples deposited at 19°C (left) and 65°C (right). 30
Figure 15: Fraction of recovered hole signal vs. interruption time from samples deposited at 19°C (left) and 65°C (right). 30
Figure 16: Energy level schematic for the investigated devices with hole-blocking contacts. Devices have the following hole-blocking contacts: (a) CeO_2 [81], (b) TiO_2 [82], (c) PTCBI [83], and (d) PI [84]. The energy levels for CeO_2 and TiO_2 are theoretical values and do not take into account

the existence of defect levels which lower the potential barrier for holes. (e) Device structure used for the experiments....33
Figure 17: Dark current density transients for a sample (ITO-PI-a-Se-Au) biased at different voltages. R1 stands for the first measurements and R2 stands for a second run, i.e., repeating the experiments. The dark current decays more than one order of magnitude in 160 s. 35
Figure 18: Dark current I-t curve for S1 (ITO-a-Se-Cr), S2 (ITO-CeO_2-a-Se-Cr), and S3 (ITO-TiO_2-a-Se-Cr) for different applied electric fields....36
Figure 19: Dark current I-t curve for S4 (Au-a-Se-ITO) and S5 (Au-PTCBI-a-Se-ITO) for different applied electric fields....37
Figure 20: Dark current as a function of electric field for S1-S5 sampled at 140 s. 37
Figure 21: Dark current I-t curve for S6 (ITO-PI-a-Se-Au) for different applied electric fields. 38
Figure 22: Dark current as a function of electric field for two different thickness of PTCBI....39
Figure 23: Dark current of a vertical device with a16 μm thick a-Se layer as a function of voltage. ..39
Figure 24: Vertical device structure (illustration not to scale). 42
Figure 25: Transmission of light trough different layers (indicated in the legend) as a function of wavelength....43
Figure 26: Measured photocurrent of S6 biased at different electric fields. 44
Figure 27: Gain of S6 (black square) and additional verification sample (red triangle) for different applied electric fields....45
Figure 28: Photoresponse of S6 exposed to consecutive light pulses for different applied electric fields. 46
Figure 29: Photoresponse of S6 exposed to a light pulse lasting more than 10 hours. 47
Figure 30: Transient response experimental setup. 47
Figure 31: Transient response of vertical devices to 100 µs pulse of light. The light response is the same for both thicknesses....48
Figure 32: Transient response of the 5 µm thick a-Se vertical device to a 10 µs pulse of light. Note that the gain of the amplifier was one order of magnitude smaller than the gain used to acquire Figure 31....48
Figure 33: Photoresponse of S6 for two different applied electric fields over a wide range of light intensities. The data was fit to a linear fit and slopes near unity were observed, indicating good linearity of the device. 49

Figure 34: Schematic of TOF experimental setup used in Thunder Bay Research Institute for measurement of transient behavior in a-Se device with PI blocking layer. 50

Figure 35: TOF signal from the 16.5 µm PI/a-Se detector biased at electric fields below avalanche regime. *E* refers to the energy of the laser pulse and *Attn.* refers to the transmission of the attenuator.. 50

Figure 36: TOF signal from the 16.5 µm PI/a-Se detector biased at electric fields above avalanche regime. *E* refers to the energy of the laser pulse and *Attn.* refers to the transmission of the attenuator.. 51

Figure 37: Extracted hole mobility over a range of electric fields applied to the 16.5 µm PI/a-Se detector (red circle) and 15 µm modified HARP structure. The difference in maximum value of the mobility in HARP and our device could be due to different quality of a-Se. The electric field values quoted were simulated based on partial capacitances of the PI/a-Se structure (Appendix C). 52

Figure 38: CMOS backplane prototype before (left) and after (right) detector layer coating. 53

Figure 39: Dark current I-t curve for a vertical structure on CMOS substrate for different applied biases. The vertical structure consists of a 2 µm PI layer for planarization, 55 µm thick a-Se, 100 nm of PTCBI as a hole blocking layer and 50 nm thick Au as a top contact. The reference device is also a vertical structure on CMOS without any PTCBI as a hole blocking layer. All the measurements were done while Au contact was positively biased. 54

Figure 40: Lateral device structure (illustration not to scale). 56

Figure 41: (a) Lateral a-Se device structure with blocking layer, (b) electrode schematic showing comb structure, and (c) photo of a total of 10 different device samples fabricated on the same substrate. 56

Figure 42: Simulated distribution of the electric field inside the detector using Medici, Synopsis Inc. The arrow length represents the field strength and it points in the direction of the field. The red dashed line represents the device region where the electric field in Figure 43 was calculated. .. 58

Figure 43: Simulated electric field across the surface of the detector for different samples (different electrode width and spacing). The troughs correspond to the area on top of the center of the electrodes. 58

Figure 44: Photogeneration efficiency of a-Se at 468 nm wavelength using Onsager theory [9] and exponential fit. 59

Figure 45: Dark current for devices (S1 and S2) with and without a blocking layer (PI). 61

Figure 46: Response of S2 from periodically pulsed light at two different electric fields 61
Figure 47: Photoresponse of (a) S1 and (b) S2 for different electric fields.. 63
Figure 48: Photoresponse of (a) S3 and (b) S4 for different electric fields.. 63
Figure 49: Photoresponse of S2, S3, and S4 at 30, 29, and 30 V/μm, respectively. 64
Figure 50: Photocurrent for different samples as a function of electric field in linear and logscale (inset)... 64
Figure 51: Simulated photocurrent for different samples as a function of electric field. 65
Figure 52: External quantum efficiency (EQE) for a vertical a-Se detector with a PI blocking contact exposed by a 468 nm wavelength source and Onsager theory photogeneration efficiency as a function of electric field. The EQE is given by dividing the photocurrent by the incident photon rate. 66
Figure 53: Photoresponse of the 5 μm thick a-Se vertical device for different electric fields. The light intensity was 96 $\mu W/cm^2$. 67
Figure 54: Photoresponse of the lateral and vertical devices, biased at 40 V/μm, exposed to green (G, 91 $\mu W/cm^2$) and blue (B, 96 $\mu W/cm^2$) light. 68
Figure 55: Lateral a-Se devices on a Kapton substrate. 69
Figure 56: Photoresponse of the lateral device on glass and Kapton for different bias voltages, 50, 75, and 100 V. The blue light intensity was 96 $\mu W/cm^2$ 70
Figure 57: Photoresponse of the lateral devices on Kapton and glass substrates for different blue light intensities at a bias voltage of 100 V. 71
Figure 58: An image of permanent defects (white spots) region on a 25 μm HARP target[98]. 73
Figure 59: Structures of the different samples tested. Amorphous selenium was deposited on glass, ITO glass, and a PI-coated ITO glass. 74
Figure 60: Experimental apparatus used to carry out the PD experiment. 75
Figure 61: Normalized transmission as a function of time for the three samples at room temperature. 76
Figure 62: The recovery (upper part) and the decay (lower part) of the optical transparency for a resting/pumping cycles at room temperature... 77
Figure 63: Energy-configuration diagram illustrating the energy barrier of transitions from metastable configuration back to initial ground state configuration.. 78
Figure 64: Normalized transmission as a function of time for two samples at 35 °C. 79

Figure 65: Onset time plots for PiC from 285 K to 343 K for a ~16.5 μm thick a-Se film grown directly on glass. 80

Figure 66: Sample spectra for the PiC results at the most active temperature. (a) Shows growth of PiC in the.......... 80

Figure 67: Experimental set-up of the UV experiment. (a) Micro-sample introduction system, (b) detector system, (c) spectrometer, (d) micro plasma device, (e) CCD spectrometer, (f) typical transient emission signal from data acquisition. 84

Figure 68: Microplasma background emission signals of (a) Ar-H_2 and (b) Ar only. 85

Figure 69: Emission signals from Zn (10 ng), Mg (5 ng), Cu (10 ng), Ag (10 ng), Cd (5 ng), and Mn (90ng). 87

Figure 70: Precision (three consecutive analytical runs). 88

Figure 71: Electric field within the vertical device structure. Note that the curves in this figure are not to scale, they are approximations for visualization purposes. 96

Figure 72: Electric field within vertical device structure, indicating the field within the a-Se bulk, F_b. 97

List of Tables

Table 1: Selected properties of several photoconductor candidates for direct conversion detectors [2]. 4

Table 2: Summary of typical scintillator's characteristics. [a]Measured at 662 keV, [b]measured at about 60-80 keV [13-15]. 6

Table 3: Digital X-ray imaging system properties [21]....... 8

Table 4: Summary of CT detectors. Note that among the three technologies, gas ionization chambers are not considered indirect conversion since X-rays cause ionization of gas molecules in the chambers where the generated free carriers drift to the anode/cathode, leading to a measurable signal [25]....... 9

Table 5: Summary of characteristics of a prototype flat-panel volumetric CT (PaxScan 4030CB; Varian Medical Systems) [29]....... 10

Table 6: The electrode work function, the exponent n (here shown with N) in the power law relation, and the ratio of current at t=3000 s and t=3 s with 2000 V applied for each metal studied [43]. 18

Table 7: Selected properties of undoped and stabilized a-Se photoconductive layers [50]. 21

Table 8: Procedure for cleaning ITO glass substrates. 26

Table 9: Deposition conditions for a-Se films using thermal evaporator in G2N lab. 26

Table 10: Carrier properties for a-Se films deposited at the University of Waterloo. Mobility was measured at 10 V/μm....... 30

Table 11: Description of prepared samples. 34

Table 12: Spin-coating and curing parameter of the PI layer. 34

Table 13: Prepared lateral a-Se samples....... 57

Table 14: Medici a-Se model parameters. 60

Table 15: Relaxation parameters for different substrates using different models: single state model (single exponential and stretched exponential) and two state model (double exponential). The goodness of fit is included using R^2, where a value closer to unity indicates a better fit. 79

Table 16: Light parameters....... 95

Table 17: a-Se parameters. 95

Table 18: Bulk electric field in a-Se for different light exposure times. 97

Table 19: Parameters used for resistance calculation....... 98

Chapter 1

Introduction

1.1 X-ray Detection

X-ray imaging is among the most important medical imaging procedures used today. The high energy of the radiation allows it to penetrate through the body and provide an image of the interior of the body, which is otherwise not visible by the human eye. A typical image acquisition using X-ray imaging is shown in Figure 1. The object, or patient, to be imaged is placed between the radiation source and the detector that acquires the image.

The variation of X-ray attenuation within the body, due to varying tissues for example, causes the variation in the acquired image. An exposure of uniform intensity exposes the body and the intensity is modulated by the differential attenuation within the body. The modulated intensity that exits the body contains the internal structure information and is sensed by the detector to form the image. Therefore, regions having a greater difference in X-ray attenuation will have greater contrast.

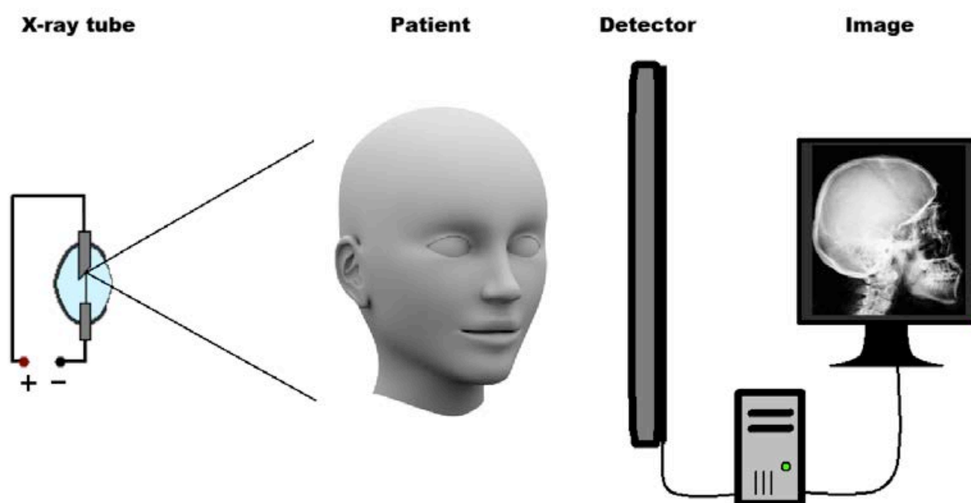

Figure 1: Radiographic image acquisition.

Since X-rays are a form of ionizing radiation, they are potentially harmful and can cause damage to living tissues. It is for this reason that the amount of radiation that the body is exposed to should be kept as low as reasonably achievable.

1.2 Direct vs. indirect conversion

Before digital radiography, a photosensitive film was used for X-ray imaging. The film was coupled to a scintillator that would convert X-rays into optical photons. The optical photons would expose the film and change its properties, which would lead to the formation of an image after the development of the film with a chemical solution. The disadvantages of film are that storage is bulky, information retrieval and transfer are time consuming, image processing is not practical, and real-time imaging is not possible.

The availability of large area electronics allowed the acquisition of digital images that addressed the disadvantages of film technology. Digital X-ray detectors can be divided into two classes: direct conversion and indirect conversion [1]. Direct conversion detectors contain a photoconductive material, such as a-Se, which converts X-ray photons directly into electrical charges. In contrast, indirect conversion detectors have a scintillation layer that converts the X-ray photons into optical photons. These optical photons are then converted into electrical charges using photodetectors, such as amorphous silicon p-i-n photodiodes. The charges are stored in a capacitor and read out using amorphous silicon thin film transistors (TFTs). Figure 2 shows the schematic of direct and indirect structures [2].

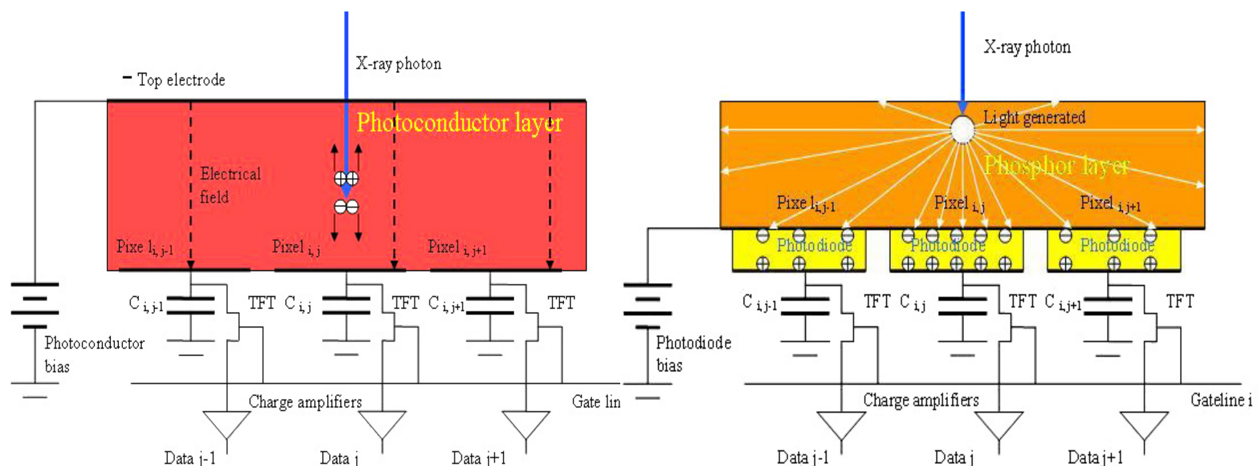

Figure 2: Cross-sectional view of (left) direct conversion detector, (right) indirect conversion detector [2].

Most currently available flat panel imagers are based on indirect conversion. However, there is ongoing interest on direct conversion for higher spatial resolution [3-6]. Using a direct detector eliminates the need for the p-i-n photodiode layer that requires a p-layer of amorphous silicon, which only a few specialized companies can manufacture [2].

In a direct conversion detector, a voltage is applied across the photoconductor layer to collect the charged generated by absorbed X-ray photons. Due to creation of a uniform electric field across the photoconductor, all of the generated charges will be transported to the pixel underneath the generation position. The lack of light scattering in the direct conversion process allows this method to have an increased spatial resolution compared to indirect conversion. However, the requirement of a high voltage supply and the deposition of a uniform thick layer of photoconductor over a large area are drawbacks of this type of detector.

1.2.1 Direct conversion photoconductor

At present, only a-Se based direct conversion detectors are commercially available and direct conversion imagers based on other photoconductors such as HgI_2, PbI_2, and CdZnTe are still in experimental stages [7]. Table 1 summarizes some important physical parameters of popular candidates for direct conversion detectors.

A high atomic number is desirable since it leads to a greater probability to absorb the photons incident on the detector. Photoconductors with small atomic numbers need to have thicker layers to absorb the same amount of photons as materials with higher atomic numbers. The amount of energy required to form a detectable electron-hole pair is given by W. As the amount of energy required per pair decreases, the number of detectable pairs for a given X-ray energy increases. The mobility lifetime products for both types of carriers are also of importance since they give an indication of the charge transport properties of the material. Other important properties include low dark current and the possibility for large area deposition.

Table 1: Selected properties of several photoconductor candidates for direct conversion detectors [2].

	Poly-HgI_2	Poly-PbI_2	a-Se	Poly-CdZnTe
Atomic Number (Z)	80, 53	82, 53	34	48, 30, 52
Energy Band Gap (eV)	2.1	2.3	2.2	1.5-1.7
Charge Pair Energy Formation (W) (eV)	5	5.5	50 (eff)	4.5
Mobility Life-Time Product (cm^2/V)	10^{-5}	(h) 1.8×10^{-6} (e) 7×10^{-8}	10^{-6} -10^{-5}	(h) 3×10^{-5} (e) 8×10^{-3}
Operational Electric Field (V/mm)	0.2-1	0.2-1	10	1-2

1.2.2 Indirect conversion scintillator

A scintillator is a material that emits visible light when it is struck by X-ray or energetic particles. There are many materials that have this property. An ideal scintillator should have the following properties [8-10]:

- High X-ray quantum efficiency
- High light yield
- Fast scintillation response
- Good spectral matching with photodetector
- Limited light spreading

Quantum efficiency is a quantity that defines the fraction of X-ray photons with energy *E* that are attenuated by a material, in this case a scintillator having a thickness of *L*, and can be expressed as:

$$\eta(E) = 1 - \exp(-\mu_E L) \tag{1}$$

where μ_E is the linear attenuation coefficient of the scintillator. The linear attenuation coefficient not only depends on the energy of X-ray photons but also depends on the atomic number and density of the material. High-density scintillator materials have high quantum efficiency due to their good stopping power. They can also decrease the volume of scintillator and reduce the cost as well.

The light yield of a scintillator is defined as the ratio of the number of optical photons produced by an incident X-ray photon, N_{ph}, to the amount of energy of that X-ray photon, E_{x-ray}. This parameter

is usually reported with the unit of photons/keV. It indicates how efficient a scintillator is at converting X-ray energy to the generation of optical photons. This parameter is important in order to reduce the radiation dose to patients as safety concerns [10]. It is desirable to produce the most amounts of optical photons possible using the least amount of X-ray energy.

Fast scintillator response is another important feature that a scintillator should have. In an integration mode type detector, the collection must take place within an integration time. The integration time is limited by factors such as dark current of the photodetector. Therefore, the scintillation should occur within the integration time. If there is any afterglow, it is going to affect following images. The interaction of a high-energy photon with a scintillator material and the subsequent generation of electron-hole pairs occur less than one picosecond [11]. However, the light response of the scintillator is limited by the time prior to the charge carrier's arrival to the luminescent centers and the decay time associated with their radiative recombination. The latter mechanism is by far slower with respect to initial conversion. In the simplest description, the decay of light intensity with time can be described by an exponential relationship with the characteristic decay time of τ [11]:

$$I(t) \sim \exp[-t/\tau] \quad (2)$$

The characteristic decay time, typically in the range of several tens of microseconds up to milliseconds, is often quoted in a scintillator's description and can aid in the proper choice of scintillator based on the application.

Although obvious, it should be stated that the spectral response of the photodetector should match that of the scintillator emission. There are numerous scintillator materials that may be used and have different emission spectrum. For example CsI:Tl has a response more catered for green absorbent photodetectors while CsI:Na has a spectrum more suited for blue absorption.

The last parameter considered here which is related to the spatial resolution of the detector is the light spreading within the scintillator. The light emitted within the scintillator is generally isotropic meaning that an equal amount of photons are emitted in all directions. This is problematic because light generated above one pixel may get stored on an adjacent pixel. To lessen the effect of light spreading, needle-like structures (such as those for CsI) are fabricated which confine the light and thus limit the lateral spread of the scintillation light [12]. Table 2 summarizes some characteristics for typical scintillators used for X-ray medical imaging applications.

Table 2: Summary of typical scintillator's characteristics. [a]Measured at 662 keV, [b]measured at about 60-80 keV [13-15].

Material	Density (g/cm3)	Emission max (nm)	Light yield (ph/keV)	Decay time (μs)	After glow $\%/ms$
NaI:Tl	3.67	410	41[a]	0.23	0.5-5/3
CsI:Tl	4.5	550	66[a]	0.8 to >6	0.1-0.8/6
$CdWO_4$	7.9	495	20[b]	5	0.005/3
Gd_2O_2S:Pr,Ce, F	7.3	510	35[b]	4	0.1/3

1.2.3 Indirect conversion photodetector

An optical photodetector is a device that absorbs optical photons and converts them to electric charge. This device comes in different structures such as photodiodes (p-i-n photodiode), avalanche photodiodes (APD), and photomultiplier tubes (PMT). Amorphous silicon p-i-n photodiodes provide the benefit of large area deposition and are typically used in indirect conversion flat panel detectors. The drawback of these devices is that they require a specialized p-layer [2] and do not provide gain above unity. Avalanche photodiodes provide gain however they are made of crystalline silicon and are thus not suitable for large area imaging. A typical PMT consists of a photocathode, focusing electrodes, electron multiplier dynodes, and an anode sealed in a vacuum tube. This device is not suitable for large area imaging due to the requirement of a vacuum tube, making it quite bulky.

An ideal photodetector for indirect conversion would provide large area fabrication, low dark current, fast response time, low cost, simple integration with TFT or CMOS processes, and gain. There are different mechanisms responsible for the creation of gain in photoconductors, such as photoconductive gain, avalanche gain, and other photocurrent multiplication phenomena like tunneling of carriers arising from the redistribution of the electric field [16].

The basic mechanism responsible for photoconductive gain is successive reinjection of the faster carrier to maintain charge neutrality [17]. For a photoconductive gain larger than unity the difference between electron and hole mobilities should be large and also the contact-material junction in the photodetector should be capable of supplying the extra carriers as required [18]. However, the persistence of the slower carrier in the photoconductor will increase the response time of the device. Thus, there is a tradeoff between the speed of response and quantum efficiency.

The avalanche process that is faster in nature is due to impact ionization. At very high electric fields, the primary electron-hole pairs generated by the incident light drift in opposite directions and can acquire enough energy during their transition from the field to produce an ionizing collision and secondary electron-hole pairs. These secondary electron-hole pairs again drift in opposite directions and some of them may produce new carriers. This process is known as impact ionization that leads to carrier multiplication and gain. Due to the different electron and hole mobilities in most materials, the avalanche process is asymmetric and the probability of avalanche initiation is greater for one type of carrier (Figure 3). Since the process of impact ionization occurs in the high electric field, keeping the current of the photodetector low in dark is challenging.

In contrast with crystalline material, initiation of the impact ionization in amorphous material with small mean free path was initially unexpected. Surprisingly, the avalanche phenomenon was observed in amorphous selenium more than thirty years ago [19]. The commercialization of avalanche amorphous selenium will be further discussed in Section 2.6.

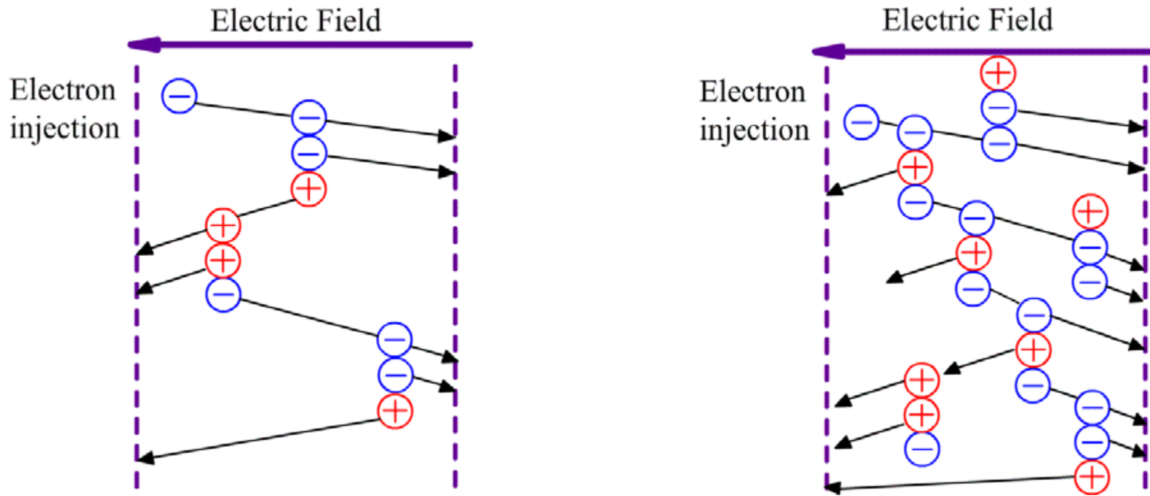

Figure 3: Avalanche multiplication process for (left) $\boldsymbol{\alpha_e} \cong \boldsymbol{\alpha_h}$, and (right) $\boldsymbol{\alpha_e} \gg \boldsymbol{\alpha_h}$.

1.3 Medical imaging modalities

There are several modalities used to meet the various needs in the field of medical imaging. X-ray imaging modalities include chest radiography, mammography, fluoroscopy, and computed tomography (CT). Each of these modalities serves a different purpose. Properties for three of the modalities are summarized in Table 3. Note that the X-ray spectrum is quoted in terms of kVp, which is the X-ray tube voltage, and the exposure is expressed in Roentgen (R).

CT differs from the other modalities in that projection images are taken at different angles with respect to the body and are reconstructed to form a three-dimensional image. Because of the added complexity, CT scanners are comparatively expensive. However due to their usefulness they are frequently used in practice. As an example of the prevalence of CT, in 2010-2011, there were 126 CT exams per 1000 population in Canada, in contrast to 47 magnetic resonance imaging (MRI) exams for the same population [20].

Table 3: Digital X-ray imaging system properties [21].

Clinical task	Chest radiography	Mammography	Fluoroscopy
Detector size	35 cm × 43 cm	18 cm × 24 cm	25 cm × 25 cm
Pixel size	200 μm × 200 μm	50 μm × 50 μm	250 μm × 250 μm
Number of pixels	1750 × 2150	3600 × 4800	1000 × 1000
Readout time	< 5 s	< 5 s	1/30 s
X-ray spectrum	120 kVp	30 kVp	70 kVp
Mean exposure	300 μR	12 mR	1 μR
Noise level	6 μR	60 μR	0.1 μR

CT systems have been developed dramatically from early 1970 when the first practical CT instrument was developed by Dr. Hounsfield to image the brain. A schematic of a third-generation scanner introduced in 1976 [22] is shown in Figure 4. In this type of scanner the source and detector array are rotated around the body. Transmission images, or projections, are acquired over different angles and reconstructed using mathematical methods to form a cross-sectional image, also known as a slice. A three-dimensional image may be formed by merging a set of contiguous slices.

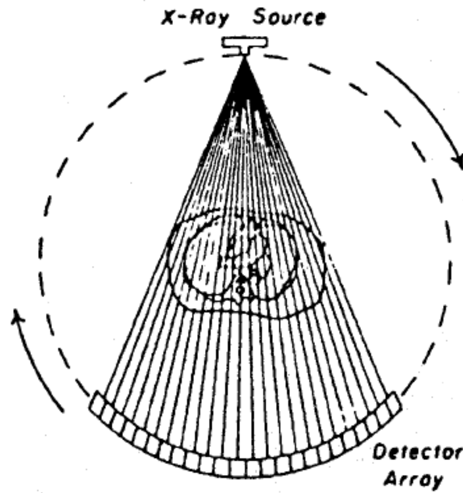

Figure 4: Schematic of a third generation CT scanner [23].

In 1993, a 2-slice CT scanner, known as a multi-slice CT (MSCT) scanner was introduced [24] and from then until around 2003 a slice war began between different vendors to achieve a greater number of slices. Throughout the development of CT technology several detector types have been used [25]. Table 4 presents a summary of different detector technologies that have been used in CT applications, along with their benefits and drawbacks.

Table 4: Summary of CT detectors. Note that among the three technologies, gas ionization chambers are not considered indirect conversion since X-rays cause ionization of gas molecules in the chambers where the generated free carriers drift to the anode/cathode, leading to a measurable signal [25].

Technology	Benefits	Drawbacks
PMT (only used in early CT scanners)	• High quantum efficiency • Fast response time	• Low packing density
Gas ionization chamber (replaced PMT)	• High packing density	• Low quantum efficiency • Slow response time
Photodiode (current technology)	• High quantum efficiency • Very fast response time • High packing density	• Maximum gain of unity

Around the same time that the MSCT scanners were being developed, the first flat panel X-ray detectors were introduced in 1995 [26]. The properties of the flat panel X-ray detectors such as high

resolution and large area were well suited for volumetric CT. In 1998 research began on CT systems using a flat panel imager to characterize its performance for different applications [27, 28]. As an example, the properties of a flat panel volumetric CT system are shown in Table 5. In flat panel volume CT scanners, a large area flat panel detector that allows imaging of a large volume in one rotation has replaced the detector rows used in MSCT scanner. Volumetric CT systems led to the emergence of a wide spectrum of new applications for both diagnostic and interventional purposes, such as ultra-high resolution bone imaging, image guided interventions, and dynamic CT angiography [29-31]. Most of these applications require low X-ray dose to limit potential harm to the patient. One of the main challenges of low dose imaging is to maintain a quantum noise limited system to achieve the highest possible signal to noise ratio (SNR) at a given dose. One potential method to achieve a quantum noise limited system is to employ a high gain detector. Current flat panel CT technology is based on indirect conversion detectors that contain a scintillator and hydrogenated amorphous silicon (a-Si:H) p-i-n photodetectors which have a gain below unity. In this thesis, an alternative detector to the p-i-n photodetector, which can achieve gain above unity and thus aid in achieving quantum noise limited systems is investigated for large area flat panel imaging.

Table 5: Summary of characteristics of a prototype flat-panel volumetric CT (PaxScan 4030CB; Varian Medical Systems) [29].

Receptor Type	Amorphous Silicon
Conversion Screen	CsI:Tl
Detector size	40×30 cm
Pixel pitch	194 µm
Number of pixcels	2048×1536
X-ray spectrum	40-150 kVp
Maximum entrance dose/frame	4mR
Limiting resolution	2.58 lp/mm @7.5 fps
Fast gantry rotation	20 to 0.4 s per 360 °

1.4 Thesis organization

The primary research objective is to develop a large-area compatible amorphous selenium (a-Se) based photodetector that can be easily integrated with TFT and CMOS processes. The secondary objective is to design and test a device structure that can provide high gain while maintaining low

dark current. The properties of the proposed detector, when integrated in a flat panel CT system will allow for low dose large area imaging.

Chapter 2 discusses different properties of a-Se as a photoconductor such as photogeneration efficiency, dark current, charge transport, and temporal response. The significance of increasing the electric field within the a-Se device to improve signal is shown. The presence of avalanche gain in a-Se is also discussed.

Chapter 3 discusses the fabrication and characterization aspects of a-Se films. Specifically, deposition conditions are described, including the substrate preparation method. X-ray diffraction measurements results for film characterization are discussed. In addition, the electrical properties of the films (charge carrier mobility and lifetime) are presented.

Chapter 4 highlights the challenges of dark current in a-Se detectors and describes the properties of a proper hole blocking layer. Different inorganic and organic layers are deposited in a multilayer structure with a-Se in the investigation of a proper hole blocking contact. The dark current behavior of the different structures is tested and compared to determine the most appropriate layer to use.

Chapter 5 presents the vertical a-Se device structure. Device performance properties such as photoresponse, linearity, transit time, and gain are shown. Time-of-flight (TOF) measurements are conducted in order to experimentally verify the avalanche nature of the gain observed in the vertical structure. Integration of the proposed device structure on a CMOS substrate is also presented.

Chapter 6 presents the lateral a-Se device structure. The device is optimized by varying the electrode width and spacing, given the same device area, for better dark current and photocurrent performance. The performance of the lateral and vertical device structures is compared. Finally, the performance of the lateral devices on flexible and rigid (glass) substrates is compared.

Chapter 7 describes the investigation of stability of a-Se detectors on different substrates against photo-induced darkening (PiD) and photo-induced crystallization (PiC). Results are presented of the photodarkening and Raman spectroscopy experiments on the fabricated devices.

Chapter 8 demonstrates the developed indirect conversion lateral detector in an example application, as a UV detector for potential use in spectrochemistry. The UV spectral response of the lateral a-Se detector is documented using a microplasma as a spectral lamp. The spectral lines of ng-amounts of diluted single element standards observed using the a-Se detector are presented.

Chapter 9 concludes this research. A summary of contributions is presented along with ideas for future work.

Chapter 2
Amorphous selenium as a photoconductor

2.1 Introduction

Amorphous selenium is one of the best photoconductors that was used in the photocopy industry more than thirty years before being replaced by modern inexpensive organic material. Xerox 914, the first commercial office copier, used a 50-60 μm thick a-Se film coated on an Al drum as a photoreceptor [32]. As a consequence, the photogeneration efficiency was extensively studied during the sixties and seventies and research laboratories in Xerox Corporation had an outstanding contribution to investigating the photoconductive properties of a-Se [32]. Photogeneration efficiency, dark current, charge transport and memory effects are among important subjects of photoconductivity and will be further discussed in the following sections.

2.2 Photogeneration efficiency

One feature present in a-Se based detectors is that some of the electron-hole pairs recombine before they can separate into free electrons and holes. Generally this is quantified by the photogeneration efficiency, defined as the fraction of electron-hole pairs that do not recombine relative to all the electron-hole pairs created [33]. This definition applies to both X-ray and optical photons. The term photogeneration efficiency can also be called internal quantum efficiency, η_{int}. The measurement of optical photogeneration efficiency has been done using two different techniques [34]. One is based on measuring the rate of photoinduced discharge of a corna-charged a-Se film under steady illumination known as the xerographic discharge technique. The other is based on the measurement of the transient photoconductivity of an electroded a-Se sample under illumination of a short light pulse known as time of flight technique.

It was found that the optical photogeneration efficiency in a-Se depends on the photon energy, the applied electric field and temperature [35]. This dependency has been observed to some degree in a

variety of low mobility materials and organic polymer. Figure 5 shows the photogeneration efficiency measurements on a-Se films of two different thicknesses as a function of the applied electric field for different exciting wavelength of light using xerographic technique [34]. It has been shown that the photogeneration efficiency from the absorption region into the bulk of a-Se for electric fields higher than 10 V/μm become closer to unity when the wavelength of incident light is shorter. The photogeneration efficiency decreases with increasing wavelength, however the photon energies of some of the studied wavelengths are still greater than the band gap, which means the absorption is complete at these wavelengths. The solid lines in Figure 5 are the theoretical Onsager dissociation efficiencies for different initial separations of an electron-hole pair due to thermalization, r_0, indicated in the figure.

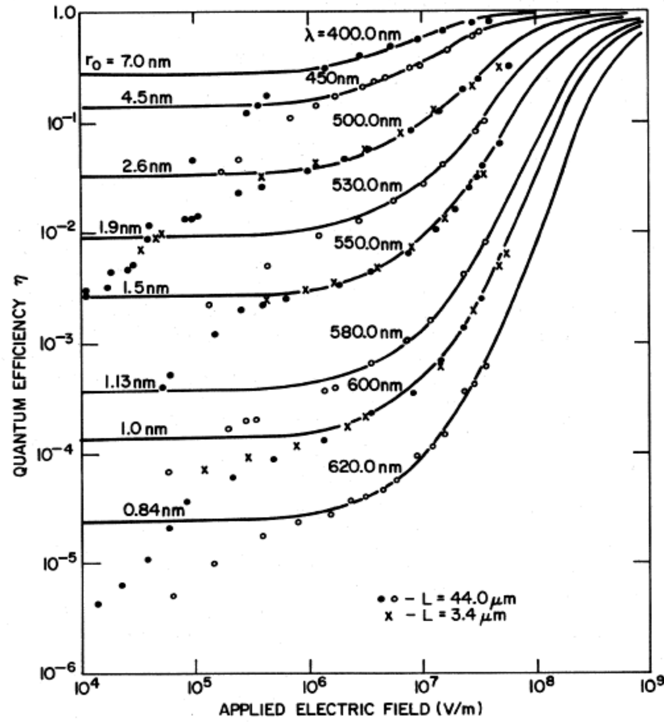

Figure 5: The experimental photogeneration efficiency of holes in a-Se versus applied electric field with different light wavelengths [34].

The Onsager approach has been used to explain the dependency of photogeneration efficiency in a-Se to the applied electric field, incident wavelength and temperature [34, 35]. It has been shown that at longer wavelengths, the initial distance between carriers is smaller which leads to smaller dissociation efficiency and as a result the quantum efficiency is lower at these long wavelengths. In

the presence of an electric field, the probability of dissociation of electron-hole pairs increases and higher photogeneration efficiency can be achieved at higher electric fields. The discrepancy between experimental data Figure 5 and theoretical model at low electric field (≤10 V/μm) can be attributed to the non-ideal collection efficiency at these fields.

We calculated the theoretical photogeneration efficiency based on the Onsager dissociation efficiency for blue and green LEDs with wavelengths of 468 nm and 520 nm, respectively. The details of the calculations are presented in Appendix A. For the calculations, we used $\Phi_0 = 1$ (Φ_0 is defined as the efficiency of production of thermalized electron-hole pairs per absorbed photon and here is assumed to be independent of the electric field). Initial separations of electron-hole pairs due to thermalization, r_0, for blue and green light were assumed to be 4 nm and 2.52 nm, respectively. The result of calculation is shown in Figure 6. In Figure 6, we also included the photogeneration efficiency for X-ray as a function of electric field [7, 36, 37]. As it is shown in Figure 6, for instance, photogeneration efficiency improves by more than a factor of 2 for blue light, more than a factor of 4 for green light and more than a factor of 2 for X-ray as field strength increases from 10 V/μm to 50 V/μm.

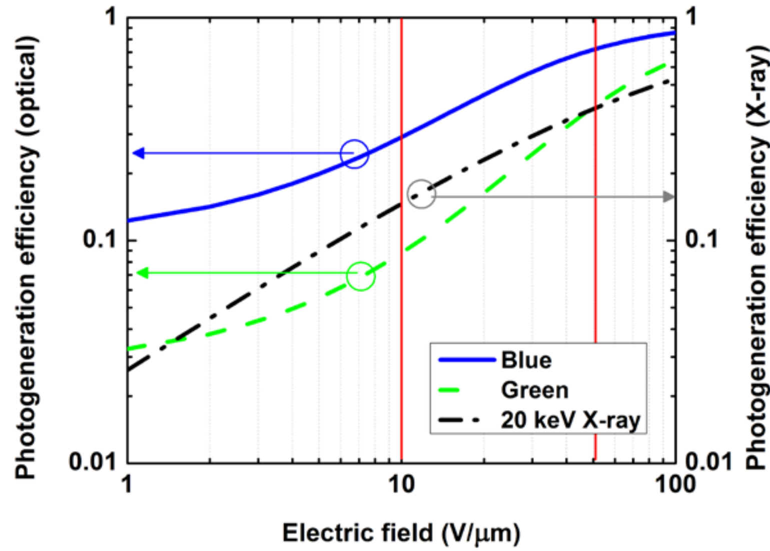

Figure 6: Photogeneration efficiency as a function of applied field for blue (468 nm) and green (520 nm) wavelengths. Obtained using Onsager theory formalism as outlined in [34]. The X-ray photogeneration efficiency of a-Se is also shown (empirical equation obtained from [37] indicating that operating at higher electric fields is also beneficial for direct X-ray imaging).

As a result, an a-Se based photodetector has to be operated at high electric fields (commercial detectors are currently operated at 10 V/μm). One problem associated to applying a high-applied field is the problem of the dark current minimization in the a-Se photodetector structure.

There is also external quantum efficiency, η_{ext}, which is defined as the number of carrier collected to produce the photocurrent, I_{ph}, divided by the number of the incident photons on the device and is given by [38]:

$$\eta_{ext} = \frac{I_{ph}/q}{P_{in}/h\nu} \quad (3)$$

where P_{in} is the incident optical power, $h\nu$ is the energy of the incident photon, and I_{ph} is the photocurrent which can be measured as the difference in the current of photodetector after illumination and before illumination (dark current).

Similar to the quantum efficiency in the scintillator, the external quantum efficiency of the photodetector depends on the absorption coefficient of the photodetector material (α) and the thickness of the absorption region (d):

$$\eta_{ext} \propto (1 - e^{-\alpha d}) \quad (4)$$

2.3 Dark current

The junction between metal and a-Se and its effects on the minimization of the dark current and device performance has received less attention in comparison to the well-studied charge transport and photogeneration mechanism in a-Se. Due to the device structure used in xerographic applications (singly-electroded device) this was not an important issue. The majority of studies reported in the sixties and seventies interpreted the dependence of the current on voltage at high fields as Space Charge Limited Current (SCLC) [39, 40]. A requirement of the observation of dark SCLC in a solid is an ohmic contact with metal to ensure a reservoir of carriers that can be injected into the solid [18]. When an ohmic contact is made between a metal and an insulator or a high-resistivity semiconductor, the injection of carriers from contact may result in current that exceeds ohmic currents. Assuming that dielectric relaxation happens much faster than recombination, a charge density of ρ_0 is diminished exponentially by $\rho = \rho_0 \exp(-\frac{t_T}{\tau_d})$, where τ_d is dielectric relaxation time and t_T is the transit time. When $t_T \gg \tau_d$, the space charge is negligible as far as the transport is concerned. The SCLC regime will reach as $t_T = \tau_d$ [41].

In order to examine the SCLC nature of electrons and holes in a-Se, researchers illuminated one or both contacts with an intense source of light with an appropriate wavelength (to confine generation of carriers close to the contact and much smaller than sample thickness). The generation region acts as a reservoir of carrier into the bulk from both contacts. For example, Pfister and Lakatos [42] deposited different thicknesses of selenium (from 0.83 to 42 μm) on a NESA substrate (glass slide coated with transparent electrode). A thin layer of gold electrode (100 A) was used as top contacts and a source of light with a wavelength of 399 nm was used as illumination source. They studied I-V characteristic and it was found that the steady-state photogenerated currents obey SCLC theories with $J \propto \frac{V^2}{L^3}$ when one electrode was illuminated and $J \propto \frac{V^3}{L^5}$ when two electrodes were illuminated (two carrier injection).

The shift from xerographic application to electroded applications such as medical imaging detectors attracted interest to measure and understand the properties of metal to a-Se junction and some studies have reported measurements on metal/a-Se/metal structure [43, 44]. From these studies, there is no general conclusion on the behaviour and observed I-V characteristic of contact formed between metal and a-Se. As an example, Johanson et al. deposited 500 μm stabilized a-Se on ITO-coated glass and studied the effect of different top contact metals (Ca, Mg, In, Bi, Al, Zn, Sn, Cr, Ag, Cu, Au, Pd, Ni, and Pt) on the I-V characteristics. Since the work function of selenium (about 5.9 eV) is larger than the metal work function for all of the studied metals, it was expected that a reversed biased schottky barrier would be formed for holes when the top electrodes were positively biased [43]. It was concluded that the I-V characteristic do not conform to specific models. As it is clear from Figure 7 no trend was observed between the metal work function and measured current, which implies that the interface between metal and a-Se is important.

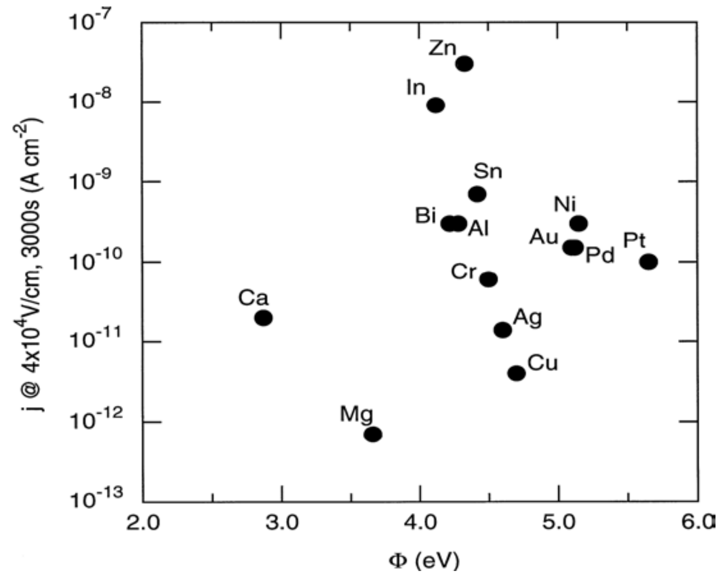

Figure 7: The current density 3000 s after applying 2000 V (across 500 µm thick selenium) plotted against the work function of the metal used for the electrode [43].

There is a power law dependence that can be observed at high fields. However, it does not follow a simple power law. The value of n in power law relation ($I \propto V^n$) with the work function of the metal investigated in this study is listed in Table 6.

Table 6: The electrode work function, the exponent n (here shown with N) in the power law relation, and the ratio of current at t=3000 s and t=3 s with 2000 V applied for each metal studied [43].

Metal	Φ (eV)	N	$I(3000\text{ s})/I(3\text{ s})$
Ca	2.9	3.8	0.25
Mg	3.65	–	3×10^{-4}
In	4.1	1.3	0.8
Bi	4.2	3.8	8×10^{-3}
Al	4.25	0.8	1
Zn	4.3	4.9	4×10^{-3}
Sn	4.4	2.4	0.3
Cr	4.5	2	8×10^{-2}
Ag	4.6	2.1	0.16
Cu	4.7	2.8	2×10^{-2}
Au	5.1	1.7	3×10^{-2}
Pd	5.1	4.0	1.4×10^{-2}
Ni	5.2	3.8	0.1
Pt	5.65	1.8	3×10^{-2}

It was found that the I-V characteristic of all samples were similar when the metals were negatively biased which suggests that the current was controlled by the ITO to a-Se junction and dominant conduction mechanism is controlled by the injection of holes from positively biased electrode rather than injection of electron from negatively biased electrode.

The space charge limited current as a main mechanism responsible for changing the current was questioned in this study based on following reasons:

- It was found that there was a dependence of I-V characteristic on the contact metal at high electric field. However, if only SCLC was assumed there should be no dependence on the metals.
- The TOF measurement was done on a sample with applying 1500 V across the sample one hour before triggering of the pulse excitation light source. The result showed only a few percent changes from the signal with no pervious bias applied before the TOF measurement. This suggests that the amount of space charge in a-Se after one hour is not considerable for changing the current by SCLC mechanism at this bias.

Although there remain theories that are not fully agreed upon, there are several important conclusions that are widely accepted by the community which are summarized below:

1. The choice of contact metal has a profound effect on the observed dark current level.
2. The dark current level decays as a function of time. However the decay characteristic differs from device to device.
3. The hole injection from the positive electrode was found to be the dominant source of dark current.

The third conclusion is the most relevant to this research as it highlights the importance of hole blocking contact to reduce the dark current. Recently, Kabir et al. described a theoretical model for the bias dependent transient behaviour of the dark current in multilayer (n-i-p) amorphous selenium based on the schottky emission of holes from the metal to a-Se junction that further confirmed the importance of hole injection from the junction to the bulk of the selenium [45].

2.4 Charge transport

In order to collect the generated carrier inside photoconductor, the photoconductor should be biased properly. In a photoconductor with both shallow and deep traps where the shallow traps

modify the mobility of carriers and deep traps control the lifetime of carriers, the electric field should satisfy the μτF condition (μτF≫L) to assure collection efficiency close to unity. The μτF is the *schubweg* of carriers, which correspond to the average distance that a carrier drifts before getting trapped [46]. Time-of-Flight (TOF) and Interrupted-Field Time-of-Flight (IFTOF) are used to measure the charge transport properties of a-Se. TOF measurement is a well-established method to measure the drift mobility in low mobility materials [47]. In TOF experiment a narrow sheet of charge becomes injected from the transparent electrode of an electroded sample using a strongly absorbed short laser pulse. The transport of carriers in a-Se is classified as non-dispersive [48], so the width of the charge sheet does not change significantly as it drifts within the thickness of the electrode sample. The intensity of the laser pulse is kept relatively low to prevent distortion of the external electric field (small-signal condition). The transient drift of charge carrier across the thickness of the sample due to applied electric field is time-resolved and is captured on an oscilloscope. The carrier drift velocity is constant under small signal condition and the mobility can be calculated using the measured transit time (t_T) from TOF experiment and the following equation:

$$\mu = \frac{L^2}{t_T V} \tag{5}$$

where L is the thickness of the sample and V is the biased voltage.

IFTOF measurement is a method to measure the carrier lifetime. The principle of this technique is similar to TOF measurement while in IFTOF, the applied bias is removed temporarily after some time t_1 and before the carrier reach the collecting electrode, i.e. $0 < t_1 < t_T$ and reapplied again. By removing the applied bias the drift of the carrier during transient is interrupted and photocurrent drops to zero. The charge carriers resume their transit by reapplying the bias at time t_2. However, some of the carrier will be lost due localized to deep traps during the interruption time $t_i = t_2 - t_1$. If the transit time t_T is much larger than the capture time t_c, the charge carrier concentration after reapplying the bias $p\,(t_2)$ and charge carrier concentration before interrupting the bias $p\,(t_1)$ are related by:

$$\frac{p(t_2)}{p(t_1)} = \exp\left(-\frac{t_i}{t_c}\right) \tag{6}$$

Since the charge carrier concentration is proportional to the amplitude of the photocurrent, the carrier lifetime can be determined from the slope of a semi-logarithmic plot of $i(t_2)/\,i(t_1)$ versus t_i.

Table 7 summarizes selected properties of undoped and stabilized a-Se. For an electric field of 10 V/μm, the electron schubweg is larger than 400 μm and the hole schubweg is larger than 1300 μm. Thus, both the electron and hole schubweg are much longer than typical photoconductor thickness. Increasing the electric field improve the carrier mobilities. For example, hole mobility becomes saturated to 1 $cm^2V^{-1}s^{-1}$ at 100 V/μm [49].

Table 7: Selected properties of undoped and stabilized a-Se photoconductive layers [50].

Property	Value	Comment
E_g(eV)	2.0	Optical transmission through thin film
$\mu_h(cm^2V^{-1}s^{-1})$	0.13-0.14[a,b]	Very reproducible, independent of thickness and source of a-Se
τ_h(μs)	10-100[a] 50-500[b]	Depends on the substrate temperature and impurities
$\mu_e(cm^2V^{-1}s^{-1})$	5-7$\times 10^{-3}$[a] 2-4$\times 10^{-3}$[b]	Depends on the source of a-Se and As content
τ_e(μs)	10-100[a] 200-1000[b]	Depends on impurities, independent of the substrate temperature. Increases with As content
$\sigma_{dc}(\Omega cm^{-1})$	10^{-17}-10^{-14}	Very sensitive to impurities. 10^{-17} is for deoxygenated sample

[a] Undoped a-Se; [b] stablized a-Se: a-Se alloyed with 0.2−0.5% As and doped with 10−40 ppm Cl)

2.5 Temporal response

For applications such as fluoroscopy with a high frame rate and CT with a high projection rate the temporal response is more important than other modalities. The temporal response can be characterized by two main components namely ghosting and lag. Charge trapping and the release of trapped charge can be considered as the main sources of ghosting and lag [51]. Ghosting is used to describe the decrease in the detector sensitivity with exposure to radiation. This type of effect can be caused by the recombination of generated free carriers with charge trapped from previous exposures. Lag is used to describe the carry-over of an image from previous exposures into subsequent images. This type of effect can be caused by the thermal release of charge trapped from previous exposures.

In addition, charge injection from biasing electrodes can increase during exposure and contribute to image lag [52]. The time constant for a charge carrier to be released from a deep trap is faster for holes (on the order of minutes) than electrons (on the order of hours). The trapped electrons are the dominant mechanism for ghosting. As shown in Figure 8, ghosting appears as reduced pixel values from previously exposed areas in a subsequent image, while lag appears as increased pixel values from previously exposed regions in a subsequent dark image.

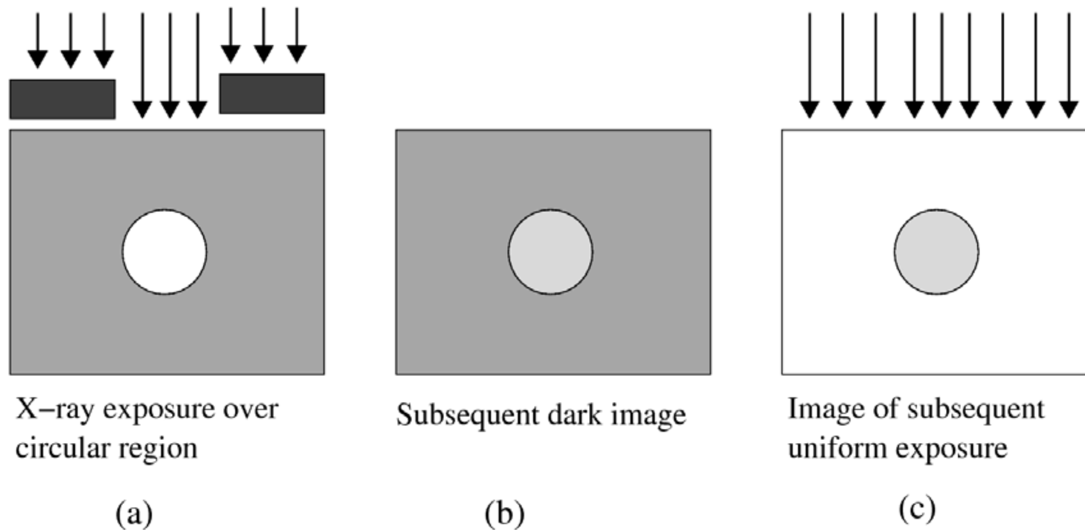

Figure 8: Images that demonstrate the appearance of lag and ghosting after an exposure of a circular region.

2.6 Avalanche in amorphous selenium

Juska et al. first observed the avalanche multiplication in a-Se in 1980 while they were studying the photogeneration efficiency and electron and hole mobility of a-Se at high electric fields [19]. They measured transient photocurrent in a-Se (20-200 μm) sandwiched between two insolating layers using the time of flight technique. It was observed that at fields higher than 80 V/μm the photogeneration efficiency increased sharply. Photogeneration efficiency larger than unity is due to photocurrent multiplication phenomena. Photocurrent multiplication in Juska's structure has been attributed to the avalanche phenomena, which entails the generation of secondary electron-hole pairs by holes at high electric fields, based on following reasons [53]:

- The shape of hole transient current changes from its usual rectangular shape at lower fields to one that increases exponentially with time due to the hole multiplication, falls sharply, and ends with a tail due to the drift of slower electrons ionized by holes;

- The photogeneration efficiency depends on the thickness of the selenium and thicker samples show a higher avalanche gain.

Soon after that, a-Se was used in commercial ultrasensitive High-gain Avalanche Rushing Photoconductor (HARP) TV camera tubes [54]. Figure 9 shows the basic structure of the HARP camera. In order to apply a high electric field across the a-Se, a multilayer vertical a-Se structure with proper electron and hole blocking material has been used. In the HARP structure, a-Se, which can vary in thickness, is sandwiched between cerium oxide, CeO_2 (several tens of nm), and the porous di-antimony tri-sulfide, Sb_2S_3 (about 100 nm) that act as blocking layers for holes and electrons, respectively. Cerium oxide is an n-type wide bandgap material that prevents injection of holes from the anode by forming a large potential barrier to holes. The di-antimony tri-sulfide layer has a large number of electron traps that become filled and form a negative space-charge barrier that stops injection of electrons from cathode [55]. In Ref [54] it is mentioned that these layers are deposited using an ordinary vacuum-evaporation method.

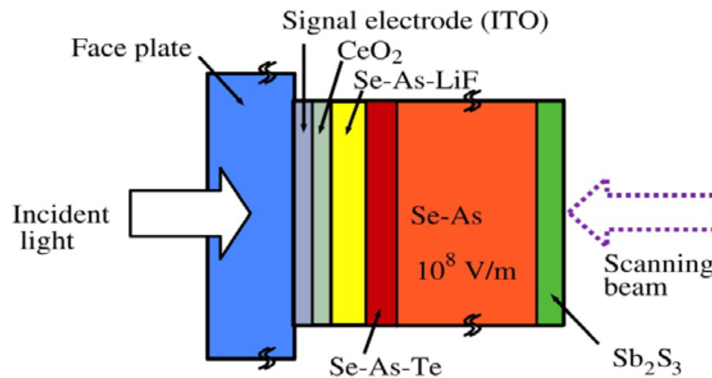

Figure 9: Schematic of HARP camera structure [56].

The selenium layer used in the HARP structure is doped with arsenic and tellurium to suppress crystallization and to increase the sensitivity for red light, respectively [55]. A thin region of the selenium layer next to the signal electrode was doped with a small amount of lithium fluoride to decrease the white blemishes [56]. A transparent indium tin oxide (ITO) or tin dioxide (SnO_2) electrode, deposited on a glass substrate, provides a contact for a positive electrostatic bias to be applied. However, there is no physical contact or electrode at the other side of the structure. This side is kept at the cathode potential of the electron gun by a scanning electron beam. This free surface is capable of supporting a latent charge image.

The incident light creates electron and holes that move toward opposite surfaces. Holes undergo impact ionization during their transit and create more free carriers. When holes reach the back surface they produce an immobile charge image that is neutralized by the electron beam. The resulting signal is read out through a coupling capacitor at the ITO electrode and used to form video images [57]. Research has been ongoing to improve the readout part of the HARP camera to a more practical way and recently there is research to adapt the HARP technology for X-ray imaging [58-62].

Although the impact ionization in a-Se was found a long time ago and led to commercialization of HARP cameras, the underlying physics of this phenomena and the theoretical understanding of its origin remained a topical research field. In amorphous materials, the typical mean free paths are smaller than the crystalline material due to inherent disorder potential inside amorphous structure [63, 64]. In addition, one surprising point is the fact that impact ionization in a-Si:H p-i-n structure happens at a higher applied electric field than for a-Se. This is interesting because the charge carrier mobility in a-Si:H is much higher than that in a-Se. Also the amount of energy needed for ionization of secondary carriers in a-Si:H is lower than that in a-Se. It has been reported for a thickness of 10 μm, the onset of avalanche occurs at 80 V/μm for a-Se and at 110 V/μm for a-Si:H [65]. Up until now, the modified lucky-drift model has provided the most successful explanation of impact ionization in amorphous material [66].

While extensive work has been done on the HARP structure, much of the research is carried out internally by companies, and thus much of the information is confidential and the specifics of the final products are not fully known by the general public. Although promising, this device has several drawbacks, including the readout mechanism, which in the current form requires a vacuum tube. Research is still ongoing to provide a more suitable readout mechanism.

Chapter 3

Fabrication and characterization of a-Se films

3.1 Introduction

The a-Se thermal evaporator located in the G2N lab at the University of Waterloo was installed in March 2010. The first step of this project involved depositing a-Se layers and characterizing them to assure the reproducibility and the quality of the films. The properties of the starting material and deposition conditions have a huge effect on properties of the a-Se layer. The initial deposition conditions, which include the level of pressure in the vacuum chamber, substrate temperature, and deposition rate were taken from previous work of Prof. Kasap's group at the University of Saskatchewan, who have extensive experience depositing a-Se films. One of the most helpful studies was done by Dr. George Belev, who studied the effect of substrate temperature on the electronic properties of a-Se [67]. The deposition parameters were modified from their initial values to better suit our system, which differs from the system used at the University of Saskatchewan.

3.2 Substrates and substrate preparation

Deposition of high quality a-Se films requires that the films be deposited on a clean substrate surface. To avoid any contamination, including contamination due to dust particles landing on the substrate surface during transport, the substrates were always cleaned just before loading them to the a-Se thermal evaporator in the course of this work. Two different types of glass were used during this project. I used uncoated Corning 7059 glass or Corning 1737F glass with one surface coated with 50 nm of indium tin oxide (ITO glass). The uncoated corning glass substrates were used for the lateral device configuration and they were cleaned using the RCA1 cleaning procedure prior to deposition and patterning of the metal. ITO glass substrates were used for the vertical device configuration

where the ITO acted as the bottom electrodes. These ITO glass substrates were cleaned using the ultrasonic bath, following the procedure outlined in Table 8.

Table 8: Procedure for cleaning ITO glass substrates.

Step #	Step Description
1	Wash substrates ultrasonically in acetone for 10 min.
2	Wash substrates ultrasonically in iso-propanol for 10 min.
3	Wash substrates with deionized water.
4	Blow dry substrates via nitrogen flow.

3.3 Deposition of a-Se

The selenium source material used in this work was supplied by New Metals and Chemicals Corporation in Japan. The material was pelletized by the manufacturer and alloyed with 0.2 % arsenic (As) and 10 ppm chlorine (Cl) with 5N purity. The a-Se films were prepared by thermal evaporation of selenium pellets from a molybdenum boat using the vacuum system shown in Figure 10. The finalized deposition parameters that suit our system are summarized in Table 9. After deposition, a-Se films were kept in vacuum and dark for at least 10 hours prior to measurements or post-processing.

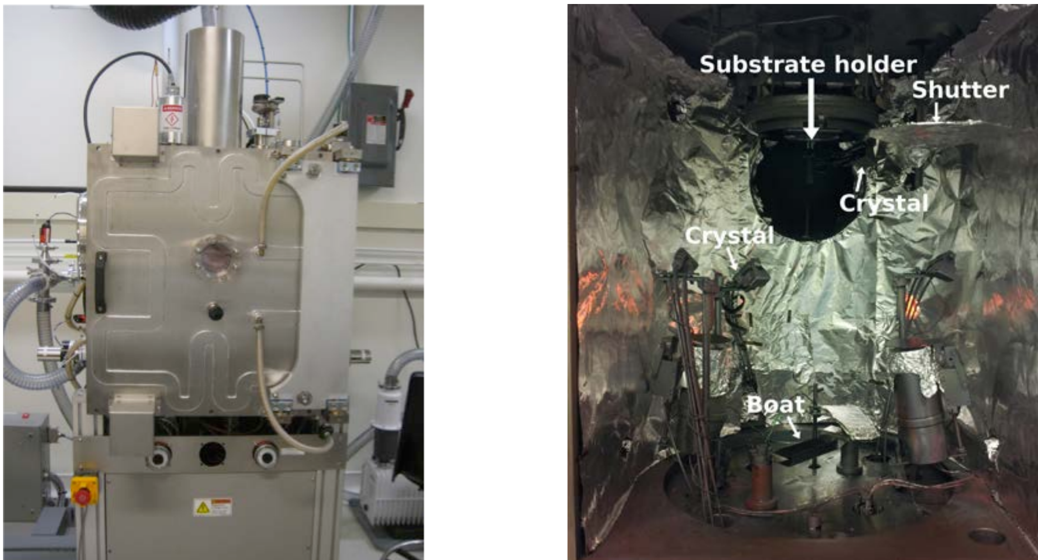

Figure 10: Selenium evaporator in G2N lab (left); the evaporation assembly inside the vacuum chamber (right).

Table 9: Deposition conditions for a-Se films using thermal evaporator in G2N lab.

Chamber Pressure (torr)	5×10^{-7}
Substrate temperature (°C)	65
Deposition rate (A/s)	110 (for ≤ 40 μm) and 170-180 (for > 40 μm)
Boat temperature (°C)	300-400
Platen rate (RPM)	50

3.4 Characterization of amorphous selenium film

The deposited a-Se films were characterized to determine their material and electrical properties. Since a-Se can crystallize due to improper deposition conditions, the first step in characterization was to determine whether the deposited films were indeed amorphous.

3.4.1 X-ray Diffraction (XRD)

X-ray diffraction (XRD) and Raman spectroscopy measurements were performed on the deposited films and the results were found to match previously reported a-Se studies. The XRD pattern of a-Se contains a broad halo at 2θ = 20-30º and the Raman spectrum of a-Se illuminated with a HeNe laser having a 633 nm wavelength contains a broad band with a peak close to 250 cm^{-1} [68, 69]. Figure 11 shows the measured XRD of deposited a-Se on a glass substrate (two different samples) and of the glass substrate by itself. The inset of the Figure 11 was taken from reference [68] for comparison. The substrate deposition temperature for sample 1 was 19°C and 65°C for sample 2.

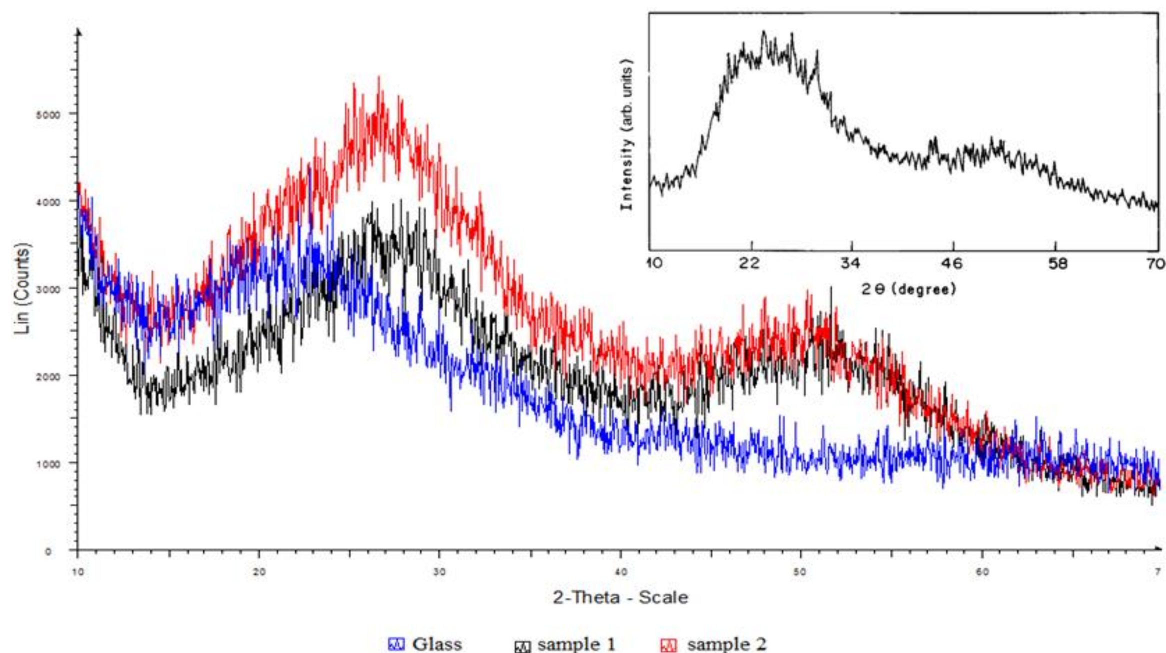

Figure 11: XRD pattern of a-Se obtained under ambient condition. Inset from [68] for comparison.

3.4.2 Electrical properties of a-Se

In order to measure the charge carrier mobility and lifetime of our deposited a-Se films, two samples were made and sent to Prof. Kasap for TOF and IFTOF measurements. The mobility and carrier lifetime were extracted from the TOF and IFTOF measurements. ITO glass was used for the substrates for the two samples. The substrate deposition temperature was 19°C for one of the samples and 65°C for the other one. The thickness of the a-Se film for both samples was approximately 45 μm. A thin layer of gold was deposited as a top contact for each sample. Figure 12 and Figure 13 show the electron mobility and hole mobility over a range of applied fields for samples fabricated at different substrate temperature, respectively. As it was discussed in Chapter 2, lifetime was determined using IFTOF method. Equation (6) was used to calculate lifetime from the slope of the fractional recovered signal versus interruption time graph. Figure 14 and Figure 15 show the ratio of the signal after interruption to the signal before interruption $\left(\frac{\mathrm{i}(\mathrm{t}_2)}{\mathrm{i}(\mathrm{t}_1)}\right)$ as a function of interruption time (t_i). The calculated carrier lifetime derived from the slope of Figure 14 and Figure 15 is summarized in Table 10. The product of mobility and carrier lifetime is called carrier range. In a *p*-like layer, the carrier range for holes is more than the carrier range for electrons. On the other hand, in an *n*-like layer, the carrier range for electrons is larger than the carrier range for holes. Comparing the values of

carrier range for electrons and holes for the sample deposited at room temperature (19°C) with the one deposited at (65°C), it can be concluded that a-Se deposited at room temperature can act as an *n*-like layer even without doping it with an alkali (Na) material. This property was previously reported [67].

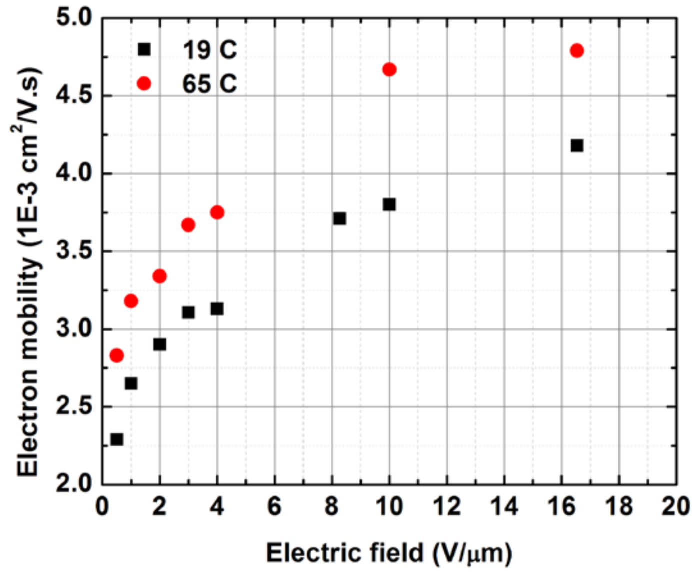

Figure 12: Field dependence of electron mobility for samples deposited at two different temperatures.

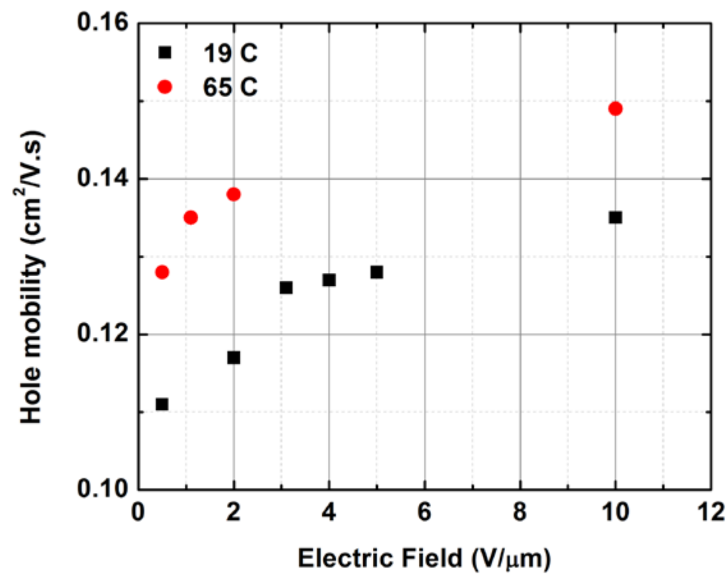

Figure 13: Field dependence of hole mobility for samples deposited at two different temperatures.

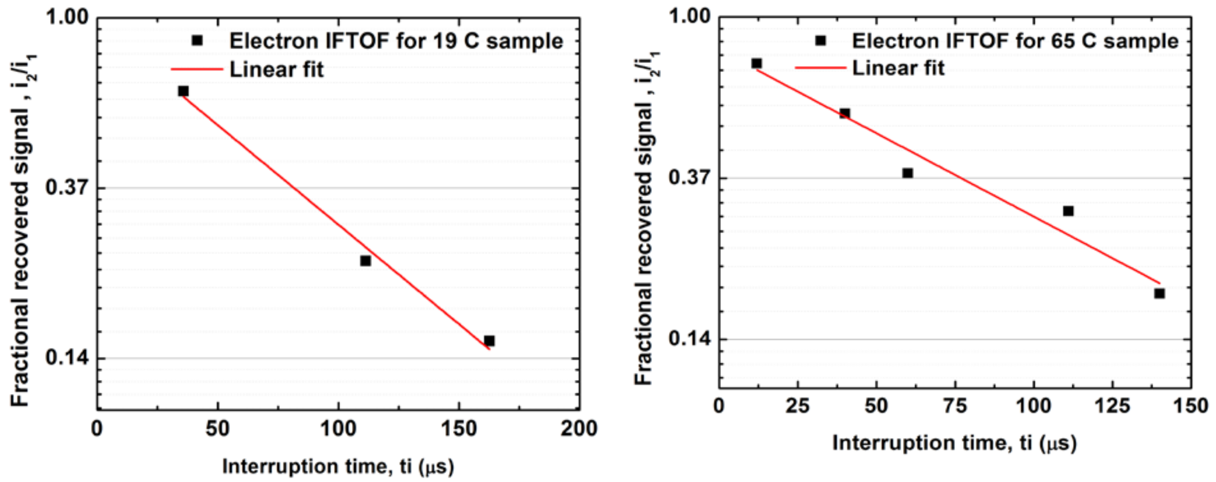

Figure 14: Fraction of recovered electron signal vs. interruption time from samples deposited at 19°C (left) and 65°C (right).

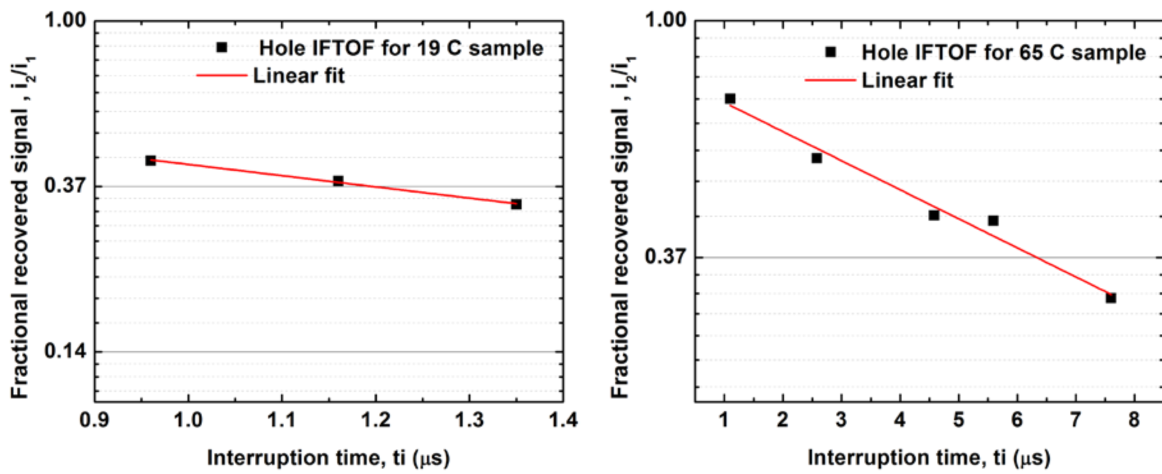

Figure 15: Fraction of recovered hole signal vs. interruption time from samples deposited at 19°C (left) and 65°C (right).

Table 10: Carrier properties for a-Se films deposited at the University of Waterloo. Mobility was measured at 10 V/μm.

Electron	Mobility (cm^2/V.s)	Lifetime (μs)	Range (1E-6 cm^2/V)	Hole	Mobility (cm^2/V.s)	Lifetime (μs)	Range (1E-6 cm^2/V)
19°C	0.0038	84	0.319	19°C	0.135	1.2	0.16
60 °C	0.00467	95	0.415	60 °C	0.149	8.2	1.22

Chapter 4

Development of high conversion gain a-Se photodetectors: Blocking contacts

4.1 Introduction

Previous studies of dark current on a simple metal/a-Se/metal structure showed that dark current is dependent on time and voltage. The dark current also depends on the nature of metal contacts, especially the positively biased contact. The simple metal/a-Se/ metal structure has a high dark current and is not practical for X-ray detector applications. A high dark current reduces the dynamic range of the device. It increases noise levels, thus degrading signal to noise ratio (SNR) and detective quantum efficiency (DQE) and can lead to crystallization of the detector due to Joule heating. Typically, the dark current density for medical imaging detector applications is reported to be approximately 1-10 pA/mm^2 [70, 71]. In commercialized a-Se detectors, different multilayer structures are used to maintain the dark current at the acceptable range for X-ray detector applications at operating fields of 5-10 V/μm.

The two main technologies currently used for dark current reduction in a-Se direct conversion flat panel imagers were established and patented by Anrad and Hologic companies [72, 73]. Anrad uses *n*-like and *p*-like layers, which are doped a-Se, as hole and electron blocking contacts, respectively. This approach is not effective at high electric fields (>10 V/μm) due to the drifting of dopant ions into the intrinsic layer (*i*-layer) at such high fields. This changes the properties of the *i*-layer and creates long-term stability problems [67]. On the other hand, Hologic uses parylene, which is an insulating layer, as a hole blocking layer and an undisclosed material as an electron blocking layer. The Hologic detector is not suitable for real time imaging because charge accumulation at the interface of parylene and a-Se requires the detector to be discharged after each illumination.

In order to make a-Se reach its full potential, higher electric fields are required. Higher electric fields within the a-Se layer improve the detector performance by increasing carrier motilities and photogeneration efficiency that leads to better dose efficiency. Researchers started modifying the multilayer structure to maintain the dark current at the same low-level while allowing the device to operate at higher fields. Recently, Hamamatsu Photonics and Fujifilm have demonstrated a-Se based detector capable of working at higher electric fields between 20-40 V/μm while keeping the dark current density as low as 5 pA/mm^2 [74-76]. The materials used as the hole and electron blocking layers are undisclosed. As it was discussed in Chapter 2, the main component of dark current in a-Se devices is due to hole injection from positively biased electrodes. This research investigates the use of a proper hole-blocking material to develop an a-Se based detector capable of working at high electric fields (> 40 V/μm).

4.2 Methods and materials

A proper hole blocking contact should have either a large potential barrier for holes between the positively biased metal contact and the a-Se layer or a large number of hole traps and a very low hole mobility. In addition, electrons should be able to flow freely through this hole-blocking layer. Most importantly, the layer should be compatible with the large area electronics semiconductor fabrication process.

Different blocking layers are tested, and their behavior as a function of electric field was investigated. The band energy diagram of devices with the four hole blocking layers investigated are shown in Figure 16. Since it has been previously used for the HARP device and has a large potential barrier for holes, CeO_2 is included in this investigation. In addition to CeO_2, TiO_2 was also tested since, like CeO_2, it is a wide band gap semiconductor and slightly *n*-type. Aside from inorganic materials, there are numerous organic materials that have attractive properties for hole blocking layers. Previously organic materials have found use in a-Se detectors by improving their spectral response [77] and stability [76, 78-80]. Two organic materials as hole blocking layers were investigated: perylene tetracarboxylic bisbenzimidazole (PTCBI) and polyimide (PI). Introducing PTCBI as a hole-blocking layer increases the potential barrier for holes from the positively biased electrode. Also PTCBI has a very low hole mobility. PI is commonly used as an insulator and when used as a blocking layer should create a significant potential barrier for holes. To avoid electric field reduction in the a-Se layer due to charge accumulation, the electrons should flow through the PI/a-Se

interface and within the PI layer.

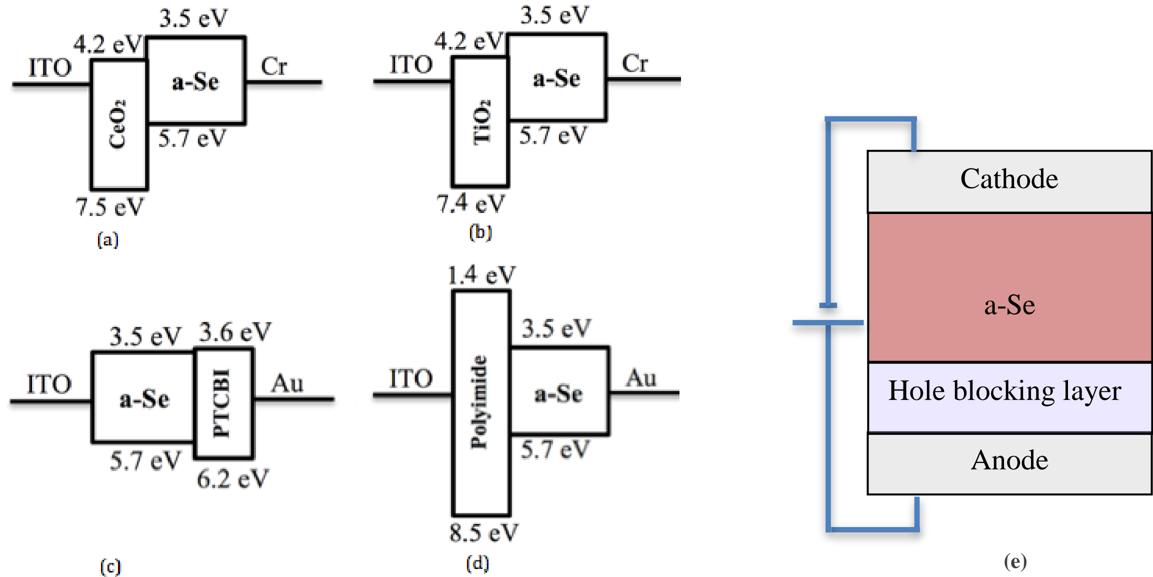

Figure 16: Energy level schematic for the investigated devices with hole-blocking contacts. Devices have the following hole-blocking contacts: (a) CeO_2 [81], (b) TiO_2 [82], (c) PTCBI [83], and (d) PI [84]. The energy levels for CeO_2 and TiO_2 are theoretical values and do not take into account the existence of defect levels which lower the potential barrier for holes. (e) Device structure used for the experiments.

Six different samples were prepared for this study, as indicated in Table 11. The structure of the samples is shown in Figure 16 and consists of an a-Se layer sandwiched between an ITO covered glass substrate and a top contact. A blocking layer was placed between the anode and the a-Se layer. Two samples (S1 and S4) used as reference devices and did not contain blocking layers. For all samples, the a-Se layer was a thermally evaporated 16-µm thick stabilized a-Se alloy (containing 0.2% As and 10 ppm Cl), where the thickness is comparable to that of the HARP device (15 µm) [59].

Oxygen ion assisted e-beam evaporation (IBAE) was used to deposit CeO_2 and TiO_2 to achieve good stoichiometry. Optical and electrical properties of CeO_2 and TiO_2 are very dependent on full oxidation of CeO_2 and TiO_2. The detail of deposition of CeO_2 and TiO_2 can be found in [85]. The PTCBI layer was deposited using thermal evaporation on top of the a-Se (i.e., after the a-Se deposition). The deposition rate for PTCBI was kept at 1 A/s.

For the last sample, a commercially available PI (HD Microsystems PI-2610) was spin-coated on the ITO coated substrate and subsequently baked. As can be seen from Table 11, the PI layer is quite thick when

compared to the other blocking layers. Although it is possible to obtain a thinner PI layer (~100 nm) with the use of an additional thinning solution (HD Microsystems T9038), such a solution was not used in this study.

Table 12 shows the spin coating and curing parameter of the PI layer.

Table 11: Description of prepared samples.

Sample #	Anode (+Bias)	Hole-blocking layer	a-Se layer	Cathode (-Bias)
S1	ITO	None	16 μm	Cr
S2	ITO	CeO_2 (30 nm)	16 μm	Cr
S3	ITO	TeO_2 (20 nm)	16 μm	Cr
S4	Au	None	16 μm	ITO
S5	Au	PTCBI (50 nm)	16 μm	ITO
S6	ITO	PI (1000 nm)	16 μm	Au

Table 12: Spin-coating and curing parameter of the PI layer.

Spin-coating polyimide	**Parameter**		**Curing**	**Parameter**
Initial spin-speed (RPM)	500	500	Initial temperature (°C)	20
Initial spin-time (sec)	7	7	Temperature ramp-rate (°C)	4
Final spin-time (RPM)	5000	3000	Final temperature (°C)	340
Final spin-time (sec)	35	35	Total cure time (hours)	2
Approximate thickness (μm)	1	2	Cooling time (hours)	4

Generally dark current in a-Se is decreasing with time from the instant that the bias is applied. It has been shown that during the first few hundreds of seconds, it reduces up to two orders of magnitude [70]. Figure 17 shows the dark current decay for a 16.5 μm thick a-Se layer sandwiched

between 800 nm of PI spin-coated on ITO glass and using Au as a top contact. Using gold as top contact in this structure is beneficial since it was reported that Au/a-Se junction acts as a electron blocking contact [86]. To be consistent, for all the samples studied on Table 11 the value of dark current versus time is recorded starting after 100 s for a total duration of 40-60 s. An Agilent semiconductor parameter analyzer (4156C) and a low-noise microprobe station were used to measure the device current and a Stanford Research Systems PS350 high-voltage power supply was used to bias the devices.

For the samples containing CeO_2, TiO_2, and PTCBI the electric field is assumed to be uniform and is obtained by dividing the applied bias voltage by the a-Se layer thickness since these blocking layers are thin and conductive. The electric field is obtained in a similar manner for the reference devices. For the PI device, since the blocking layer is quite thick with very high resistivity, the device was simulated (using MEDICI, Synopsis Inc.) to estimate the electric field within the a-Se layer. Note that the simulation does not consider the variation of mobility with electric field, as discussed in Appendix C.

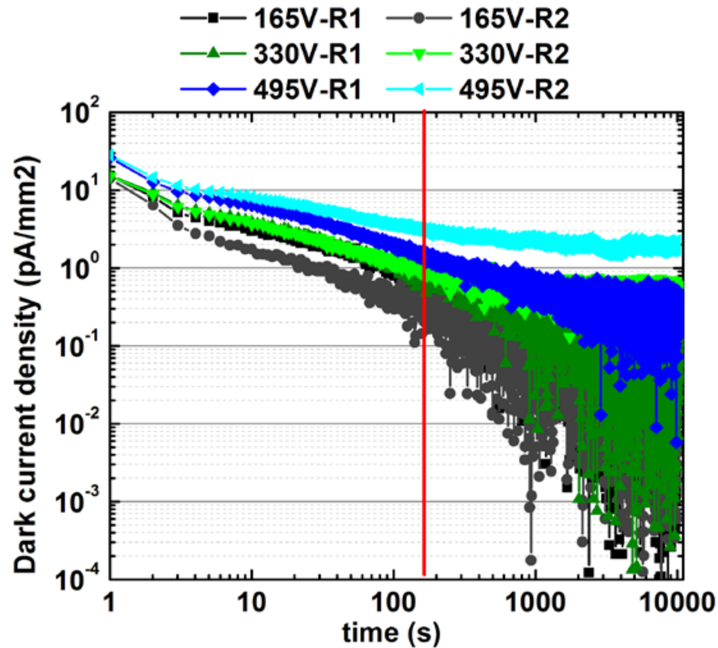

Figure 17: Dark current density transients for a sample (ITO-PI-a-Se-Au) biased at different voltages. R1 stands for the first measurements and R2 stands for a second run, i.e., repeating the experiments. The dark current decays more than one order of magnitude in 160 s.

4.3 Results

The dark current of the different samples were tested under different applied electric field strengths to determine their effectiveness. The results are summarized in Figure 18 to Figure 23. From Figure 18, it can be seen that S2 (CeO_2) and S3 (TiO_2) have comparable behavior. The dark current for both S2 and S3 is reduced significantly (e.g., greater than one order of magnitude at 30 V/µm) compared to the reference device. However the dark current reaches unacceptably high levels when the applied field is increased past approximately 40 V/µm. Hole blocking capabilities of CeO_2 and TiO_2 depend strongly on the number of defect levels generated from oxygen vacancies in these materials. This makes the dark current of a-Se very sensitive to the deposition conditions. Our results significantly differ than the results using 10-30 nm CeO_2 in the HARP samples [81]. One cause of the difference may be due to the quality of our CeO_2 and TiO_2 with respect to defect levels. Although it may be intuitive to expect that the dark current would decrease with a thicker CeO_2 layer, this is not found to be the case. It was previously reported that increasing the CeO_2 layer thickness leads to more defect levels in the layer, which lowers the potential barrier for holes and as a consequence increases the dark current [81]. Figure 19 shows that PTCBI (S5) provides less blocking ability compared to CeO_2 (S2) and TiO_2 (S3) when these devices are compared to their respective reference devices. From Figure 18 and Figure 19, it can be seen that the dark current is relatively constant after 140 s. For better comparison, the dark currents sampled at 140 s for S1-S5 are summarized in Figure 20.

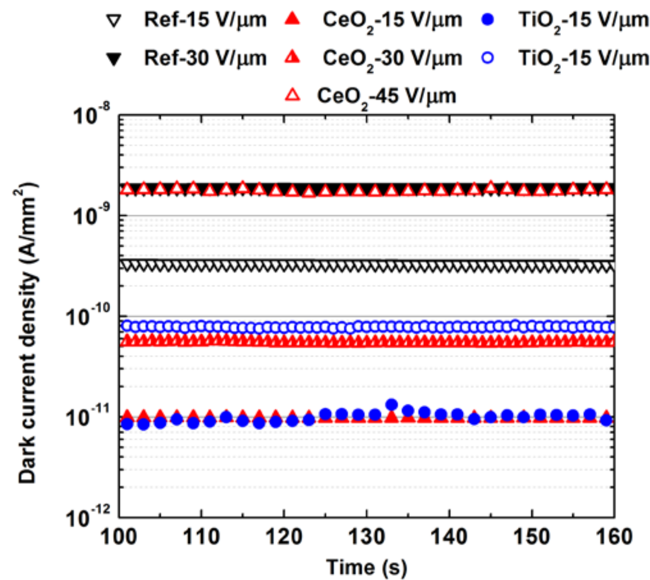

Figure 18: Dark current I-t curve for S1 (ITO-a-Se-Cr), S2 (ITO-CeO_2-a-Se-Cr), and S3 (ITO-TiO_2-a-Se-Cr) for different applied electric fields.

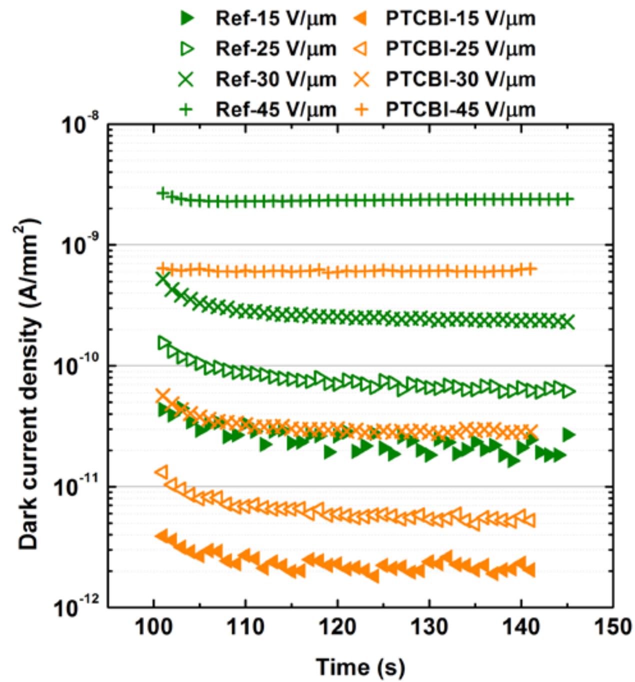

Figure 19: Dark current I-t curve for S4 (Au-a-Se-ITO) and S5 (Au-PTCBI-a-Se-ITO) for different applied electric fields.

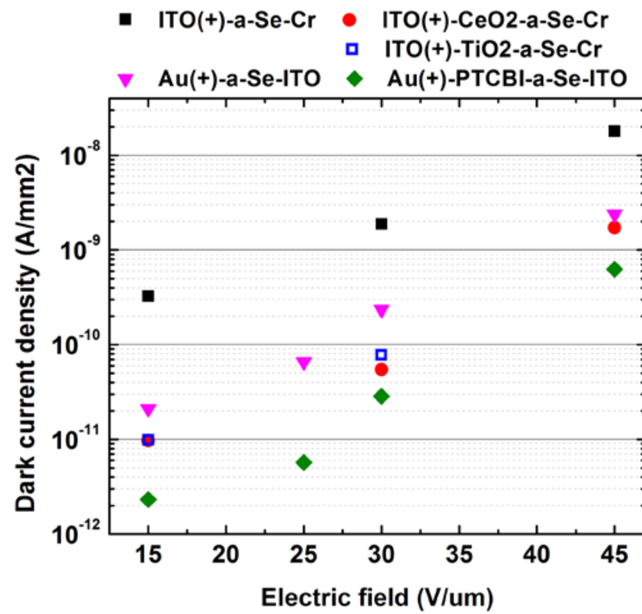

Figure 20: Dark current as a function of electric field for S1-S5 sampled at 140 s.

From Figure 21 it can be seen that a single spin-coated PI layer can maintain comparatively lower dark current at significantly higher electric fields across the a-Se layer. It should be noted that the large variation of the dark current at 15 V/μm is due to the limitation of the measurement equipment, which is approximately 100 fA. From these results, it is evident that using CeO_2, TiO_2, or PTCBI as the only blocking contact is not sufficient to keep the dark current low at the high applied electric fields required for signal amplification in emerging imaging applications. Unlike CeO_2 where the dark current is increasing with increasing the CeO_2 thickness, a thicker PTCBI layer may further reduce the dark current as it can be seen in Figure 22. The reasons one might choose not to use a thick PTCBI layer in place of polyimide are mostly practical. PTCBI is considerably more expensive (>$300 today for a 800 nm layer) compared to PI (<$10 today for a 800 nm layer) although economies of scale and in-house production can change this. Moreover, PI is deposited by spin-coating, a simpler and less capital intensive process when compared to thermal evaporation used for depositing PTCBI layers. Again, large-scale adoption of the PTCBI process can remove the cost advantage of polyimide. Lastly, in contrast to PTCBI, PI is already in use as an inter-level dielectric in the integrated circuits manufacturing industry. This is perhaps the biggest advantage PI layers possess.

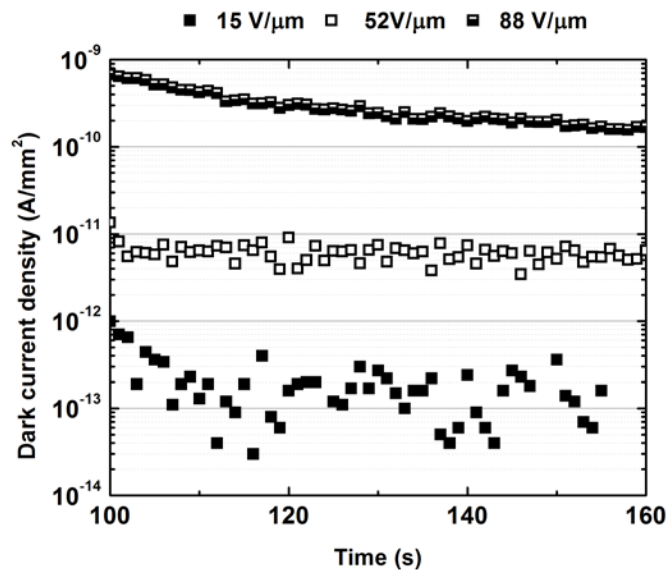

Figure 21: Dark current I-t curve for S6 (ITO-PI-a-Se-Au) for different applied electric fields.

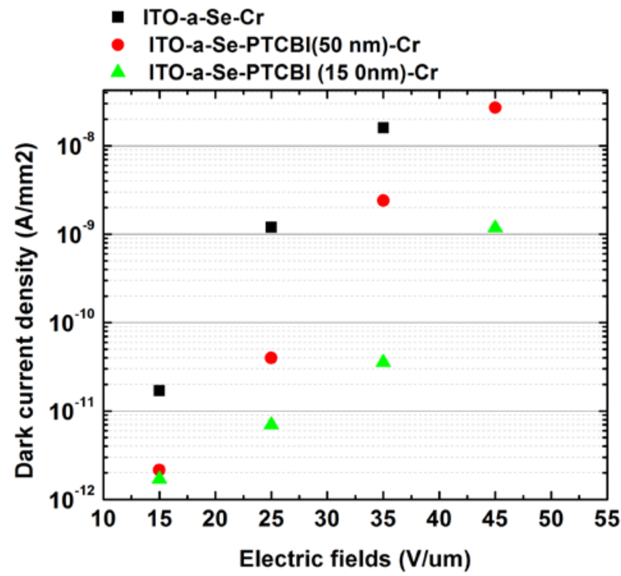

Figure 22: Dark current as a function of electric field for two different thickness of PTCBI.

To show the significance of hole injection from the positively biased electrode as the dominant part of the dark current [71], as was discussed in Chapter 2, Figure 23 shows the dark current of S6 (ITO-PI-a-Se-Au) when ITO is positively biased and when Au is positively biased. As it can be seen from Figure 23, the dark current is approximately three orders of magnitude larger when Au is positively biased.

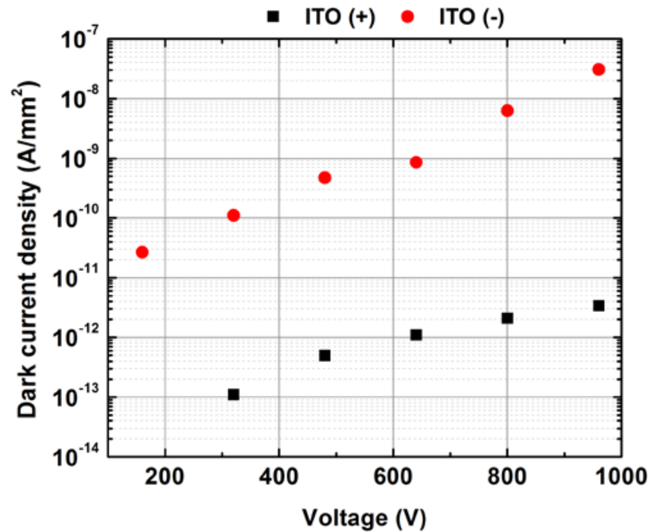

Figure 23: Dark current of a vertical device with a16 µm thick a-Se layer as a function of voltage.

4.4 Conclusion

Different hole blocking contacts in an a-Se device were studied and their dark current behavior with increasing applied electric fields was compared. It was found that a PI blocking layer permits operation at high electric fields greater than 80 V/μm while maintaining a dark current density below 200 pA/mm^2. The detectors using PI layer utilize a simple fabrication process based on widely available semiconductor materials that can be easily integrated into current large area digital imager manufacturing processes. Since achieving gain requires operating the a-Se at a high electric field, the proper choice of blocking contact for device implemented in a flat panel CT system is of great importance. The superior blocking properties of the PI layer, in addition to its ease of fabrication and compatibility with both TFT and CMOS technologies make it appealing for flat panel CT.

Chapter 5

Development of high conversion gain a-Se photodetectors: Vertical structure

5.1 Introduction

Due to the promising dark current performance of the PI layer as a hole blocking contact discussed in Chapter 4, the device with a PI blocking contact was further investigated. The vertical structure, as shown in Figure 24, gets its name from the fact that it is comprised of a vertical stack of different layers on top of each other. This structure is similar to commercially available a-Se direct conversion flat panel detectors. In the vertical structure, the electric field is uniform throughout the a-Se layer so that the electron-hole pairs are separated and the charge carriers reach the collecting electrodes at the same point in the x-y plane as they were generated (i.e., no lateral movement). This is why direct conversion detectors based on a-Se layers offer better resolution (compared to their indirect conversion counterparts). For indirect conversion applications, a thin layer of a-Se (approximately 1-2 µm) is more than enough to absorb the visible range photons (generated by the scintillator) in compared to the 200 µm thickness of a-Se required for direct conversion detectors to absorb X-rays used for mammographic applications (20 keV). However, the threshold voltage for initiation of impact ionization increases with decreasing a-Se thickness.

In this research, several vertical structure devices with different thicknesses of a-Se (5, 16.5, 56, 110 µm) were fabricated. The a-Se source boat currently used in the selenium evaporator could be filled with a maximum of 110 gr of selenium pellets, which leads to a maximum a-Se thickness of 50-60 µm. However, the capability of installing a boat that is four times bigger is available. In order to prevent readjusting the deposition parameters with the bigger boat for a potentially thicker layer of a-Se, the smaller boat was still used for thick depositions. To do so, the vacuum was broken and the

boat was reloaded. For characterization and comparison purposes, devices with 16 μm of a-Se (S6 from Chapter 4) were chosen since this thickness is close to that of the a-Se layer in the HARP structure.

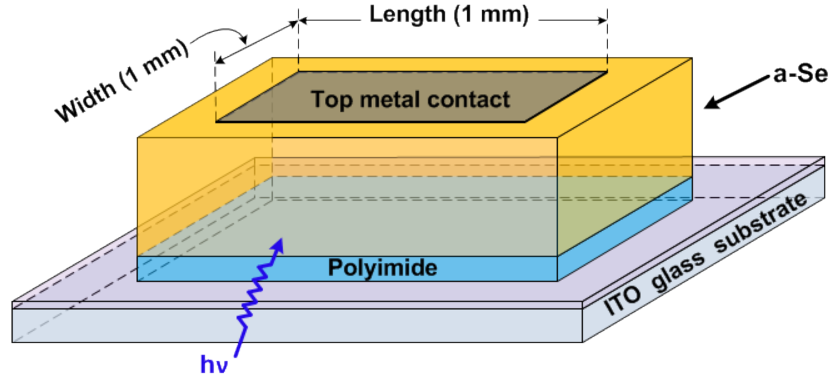

Figure 24: Vertical device structure (illustration not to scale).

5.2 Experimental details

For an indirect conversion detector, the X-ray to charge conversion gain is given by [87]:

$$g_{conv} = \eta_{X-ray} g_{scint} \delta \eta_{eff} \tag{7}$$

where η_{X-ray} is the X-ray quantum efficiency (i.e., the fraction of X-rays that interact with the scintillator), g_{scint} is the X-ray to photon conversion gain of the scintillator, δ is the optical coupling efficiency between the scintillator and the photodetector, and η_{eff} is the effective quantum efficiency of the photodetector. The first two terms of (7) depend on the scintillator performance while the last term depends on the photodetector performance. The conversion gain of the X-ray detector can be increased by increasing the effective quantum efficiency of the photodetector. The effective quantum efficiency of the fabricated devices was determined using:

$$\eta_{eff} = \left({}^{I_{ph}}/_{e} \right) \left({}^{h\nu}/_{P_{in} AT} \right) = \eta_{in} \left(1 - e^{-\alpha d} \right) G \tag{8}$$

where I_{ph} is the current of the device after shining light minus the device dark current, *e* is the electron charge, P_{in} is the incident light power, *A* is the area of the device, *T* is the light transmission through any light absorbing layers before the a-Se, hυ is the incident photon energy, η_{int} is the internal

quantum efficiency or photogeneration efficiency, α is the wavelength dependent absorption coefficient of a-Se, d is the a-Se thickness (16 μm), and G encompasses the transport efficiency, collection efficiency and any gain in the system. As can be understood from (8), the effective quantum efficiency can be increased by increasing η_{int} or G.

The photogeneration efficiency, which is electric field and wavelength dependent, is less than unity and has been modeled using the Onsager theory [34]. Previous work has shown that the Onsager theory fits the photogeneration data in a-Se very well. The theoretical photogeneration efficiency based on the Onsager dissociation efficiency was calculated in Chapter 2 (Figure 6).

The benefit of using (8) is that it allows us to yield a rudimentary estimation of the device gain. The left-hand side of (8) is obtained using experimental measurements while the right-hand side is used to evaluate the gain assuming transport efficiency and collection efficiency in the device are one hundred percent. Under these assumptions, the acquired estimate of the gain is necessarily conservative. Light transmission, T, through ITO glass, CeO_2, TiO_2, and PI on ITO glass was characterized using a UV-VIS spectrophotometer with the results shown in Figure 25.

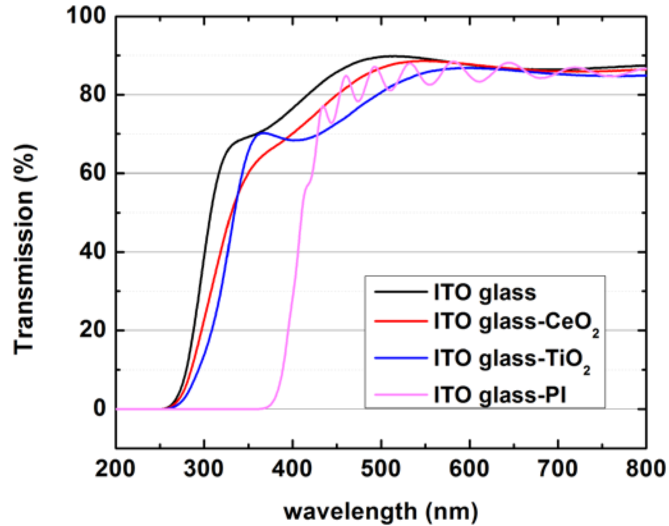

Figure 25: Transmission of light trough different layers (indicated in the legend) as a function of wavelength.

An Agilent semiconductor parameter analyzer (4156C) and a low-noise microprobe station were used to measure the device current and a Stanford Research Systems PS350 high-voltage power supply was used to bias the device. Amorphous selenium is more sensitive to light at blue wavelengths, which matches well with the emission characteristics of a cesium iodide scintillator

doped with sodium (CsI:Na). As a consequence, a blue LED is usually used as light source for investigating the photoresponse behaviour of a-Se devices.

5.3 Photoresponse

In order to study the photo response of the device, a 468 nm wavelength light source at an intensity of 170 μW/cm^2 was used. The photoresponse of the device at increasing electric fields is shown in Figure 26 where it can be seen that an electric field of 92 V/μm was achievable while maintaining a dark current below 1 nA/mm^2. As mentioned in Section 5.2, a conservative estimate of the gain of the device, G, can be determined using (8). The gain of the device, which is plotted in Figure 27, was calculated at different applied electric fields using (8) and the measured results in Figure 26. The measurements were carried out on multiple in-house fabricated device samples and found to be repeatable. The results from one such additional sample are also shown in Figure 27 (red triangles).

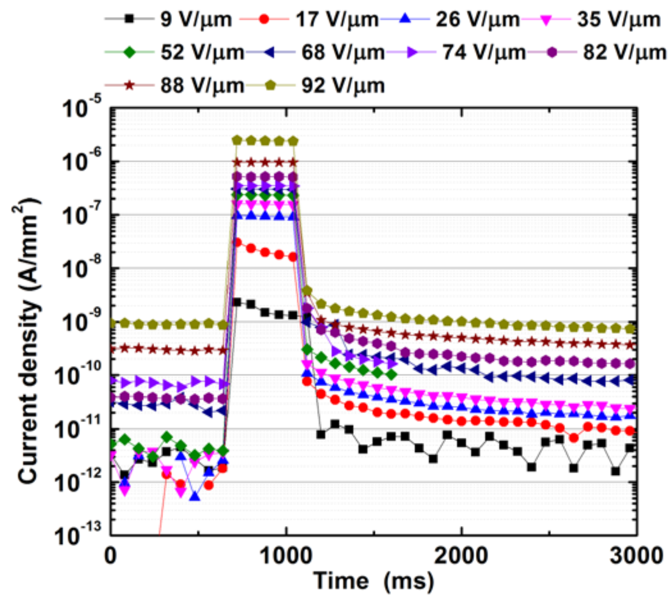

Figure 26: Measured photocurrent of S6 biased at different electric fields.

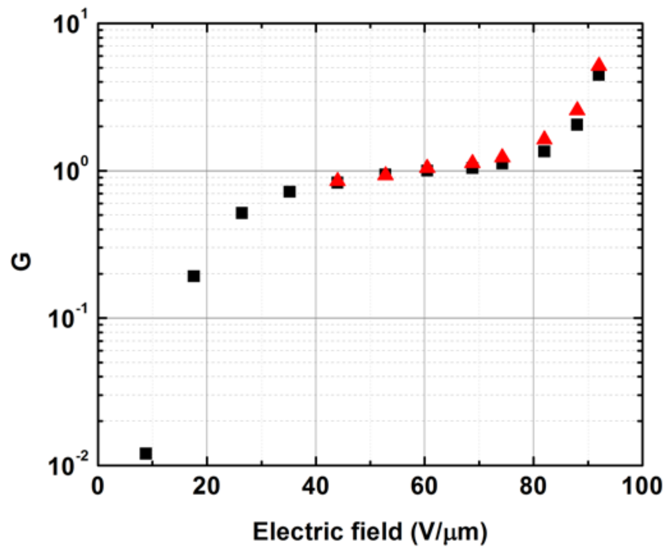

Figure 27: Gain of S6 (black square) and additional verification sample (red triangle) for different applied electric fields.

At low electric fields, the gain is much less than unity. Comparing Figure 6 in Chapter 2 (Onsager theory) and Figure 27 (experimental results), there is a large deviation for the gain value below 30 V/μm. The large deviation may be due to the carrier transport properties of the PI layer at low electric fields. Regardless of this deviation at low fields, it is noted that it is beneficial to operate the device at high electric fields due to higher conversion gain. The gain then tends to saturate near unity from approximately 50 V/μm to 75 V/μm. At high fields the gain starts to increase reaching 4.46 at 92 V/μm. Although we believe the gain above unity is due to an impact ionization mechanism such as avalanche multiplication, additional verification is necessary to determine the exact cause of this gain. Interestingly, the shape of the gain plot in Figure 27 agrees well with the shape of the gain plots reported for the HARP selenium samples [56, 59] where an avalanche multiplication mechanism is also claimed.

Since PI is typically used as an insulator and there is a conduction band offset at the PI/a-Se interface (see Figure 16), it was initially suspected that charge (specifically electron) accumulation would occur at the a-Se/PI interface and would degrade the device performance over time by reducing the internal electric field of the device. In order to determine whether there was significant charge accumulation at the a-Se/PI interface due to incident light, the light source was periodically pulsed (for 7 s the LED was on and for 15 s the LED was off) and the resulting response was examined for indications of field degradation. The response is shown in Figure 28 for different applied electric fields. As can be seen, the photocurrent is quite stable over time, suggesting that charge accumulation

does not significantly impact the internal field within the a-Se layer.

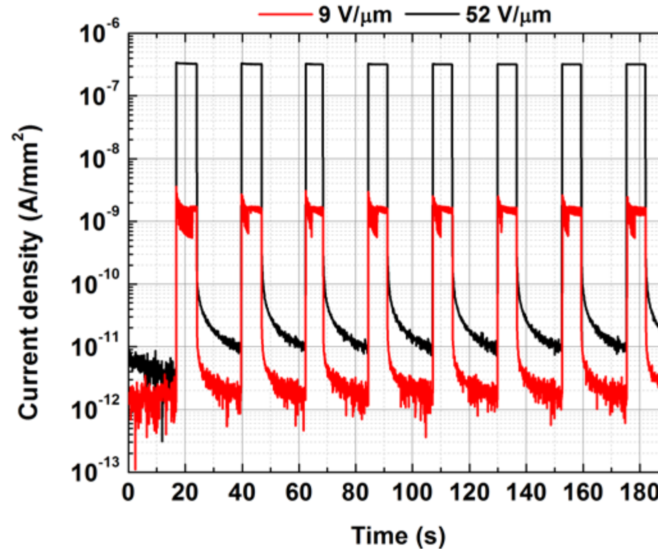

Figure 28: Photoresponse of S6 exposed to consecutive light pulses for different applied electric fields.

The dielectric constant of PI is 2.9, while its resistivity is 10^{16} Ωcm, which implies a long dielectric relaxation time (on the order of 100 minutes). The device was left under illumination for more than 10 hours (600 minutes) to further verify whether charge accumulation is significant on the long time scale. The light intensity applied, along with the time it was applied for, yielded an estimate of accumulated charge much greater than the total charge that would be required to fully deplete the device (i.e., the device is no longer operating in the small signal regime). The results are shown in Figure 29 where again the degradation in the photoresponse is minimal and is equivalent to that seen in a typical a-Se device without any blocking layer present. The results in Figure 29 also suggest that charge accumulation at the a-Se/PI interface is negligible. In Appendix B, we show that in the case of charge accumulation at the interface of PI/a-Se, the electric field within a-Se layer will drop to zero less soon after light illumination. The behavior of the PI blocking layer observed in the experiment at 35 V/μm is in contrast with the parylene blocking layer used in [73] where the parylene acts as an insulator and charge accumulation is reportedly present reducing the field in the thick a-Se layer. Thus, it is concluded that the PI layer is not perfectly insulating.

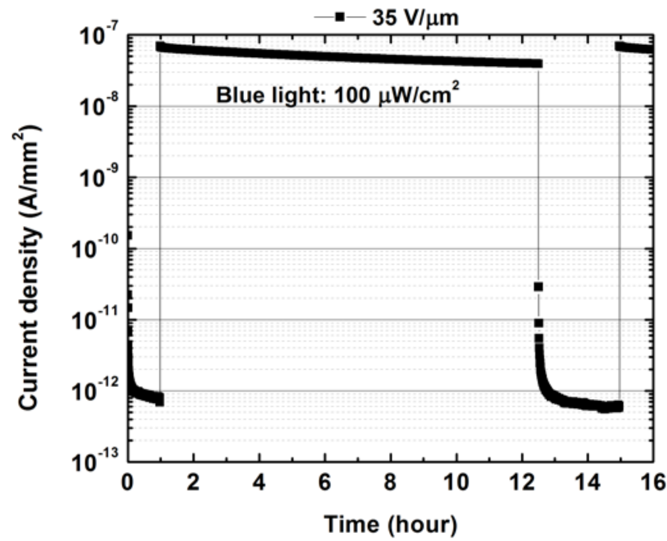

Figure 29: Photoresponse of S6 exposed to a light pulse lasting more than 10 hours.

5.4 Transient response

In this experiment, in addition to S6 (ITO-PI-16 a-Se-Au) another device with the same vertical structure and with 5 µm a-Se thickness was fabricated. In this experiment, an oscilloscope was used for signal acquisition while an Ametek 5182 low-noise current amplifier was used to amplify the signal (since the Agilent semiconductor parameter analyzer (4156C) sampling time is not fast enough). The measurement setup is shown in Figure 30.

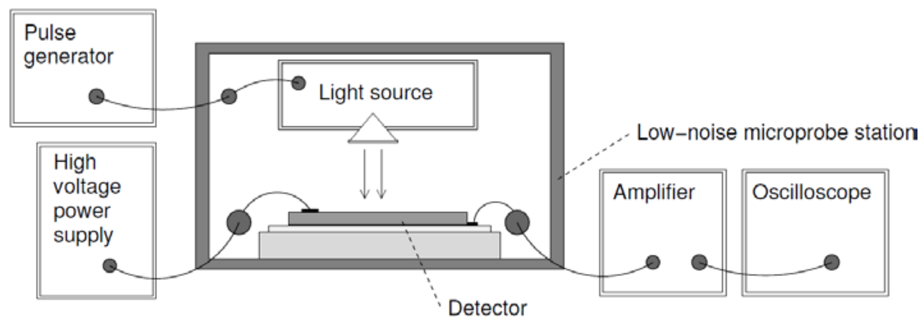

Figure 30: Transient response experimental setup.

A 468 nm wavelength (blue) light source (660 µW/cm^2 light intensity) was used for the experiments. The devices and light source were placed in a low-noise microprobe station. The gain-bandwidth product of the amplifier limited the maximum pulsing frequency. Thus the experiments

were limited to 100 kHz. The photoresponse of the fabricated vertical devices are shown in Figure 31 and Figure 32 for 100 μs and 10 μs pulse widths, respectively. Both vertical devices are shown to have the capability to operate at high speed.

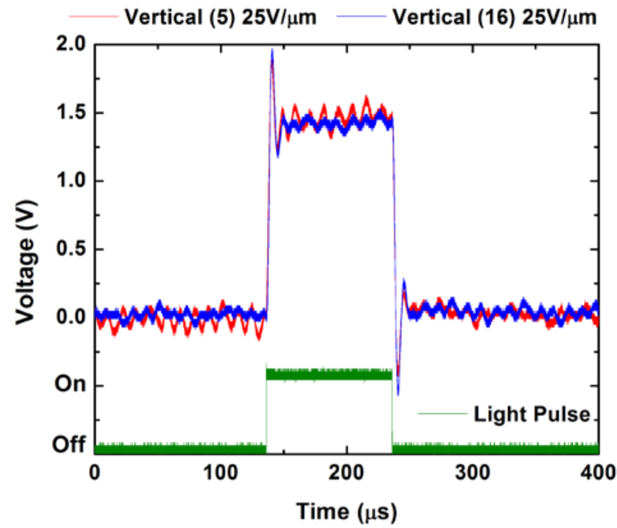

Figure 31: Transient response of vertical devices to 100 μs pulse of light. The light response is the same for both thicknesses.

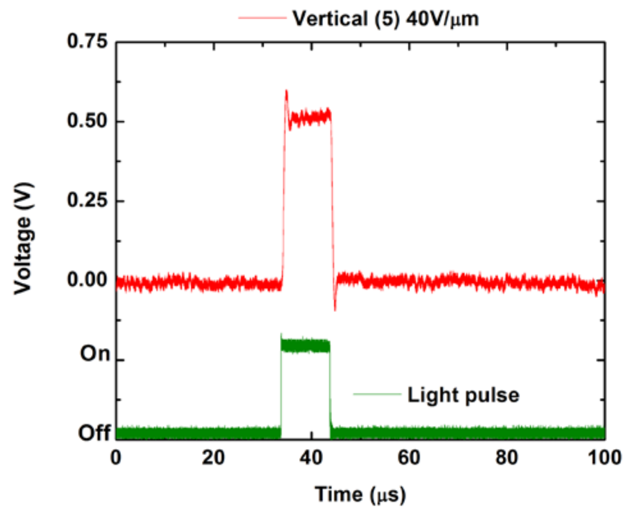

Figure 32: Transient response of the 5 μm thick a-Se vertical device to a 10 μs pulse of light. Note that the gain of the amplifier was one order of magnitude smaller than the gain used to acquire Figure 31.

5.5 Linearity

The photoresponse linearity of the 16 µm device was then tested over a wide range of light intensities (0.33 nW/cm^2 to 290 µW/cm^2). The results are shown in Figure 33 for two different electric fields (35 V/µm and 82 V/µm). The data was fit using a linear fit and reasonable linearity was observed over the studied light intensity range.

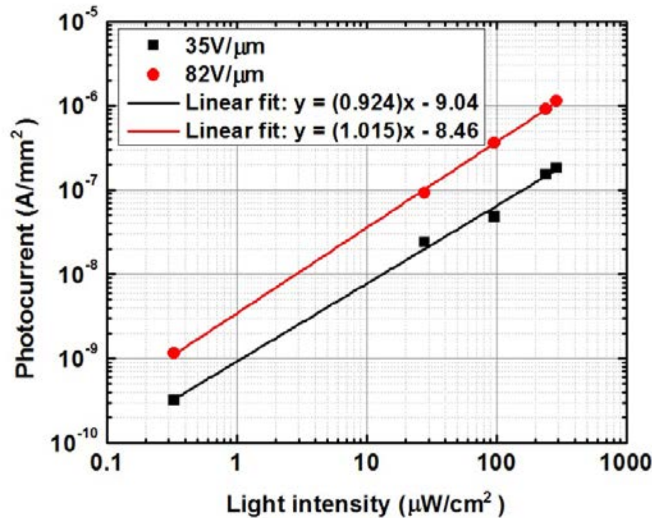

Figure 33: Photoresponse of S6 for two different applied electric fields over a wide range of light intensities. The data was fit to a linear fit and slopes near unity were observed, indicating good linearity of the device.

5.6 TOF measurement

The time-of-flight (TOF) technique was used to investigate transport and charge collection properties in the device with the PI blocking contact. The analysis of transport properties of this device is important to determine the effect of the PI layer on transient response. For comparison purposes, a device without the PI layer is needed. However, without the PI layer, TOF measurements at high fields (≥ 10 V/µm) are not practical due to very high dark current and breakdown of the device at electric fields higher than 30 V/µm. Therefore, a modified pixelated HARP sample was used that is the only current a-Se device capable of working at high electric fields up to 110 V/µm. The pixelated HARP sample is the exact same structure as discussed in Section 2.6 that was shipped from NHK to Thunder Bay Regional Research Institute. The samples were pixelated by spin-coating a Resistive Interface Layer (RIL) made of a semi-insulating polymer, namely cellulose acetate (CA) before deposition of a Au top contact. It was shown previously that adding a thin (approximately

1 µm) RIL does not degrade transport properties of the device but prevents breakdown of the device due to increased electric field at the edges of metal electrodes [88].

For TOF measurements, short laser pulses of approximately 35 ps with a wavelength of 420 nm were used. Both devices were exposed from the ITO side and the photocurrent transients were monitored at different electric fields by an oscilloscope (Figure 34). The electric field across the a-Se layer was created by positively biasing the ITO layer. The absorption depth of a 420 nm wavelength photon within a-Se is very short and almost all electron-hole pairs are generated close to the PI/a-Se interface. Electrons are collected by the ITO contact and holes traverse the thickness of a-Se to get collected by the Au contact. Figure 35 and Figure 36 show TOF measurement results at electric fields below and above avalanche multiplication.

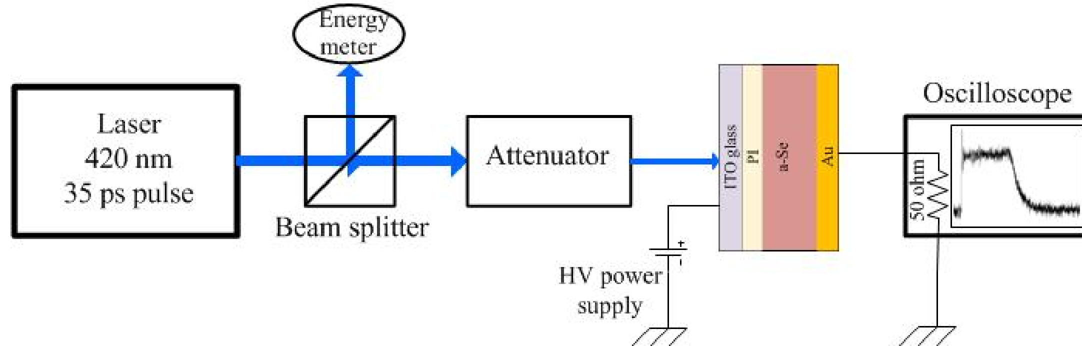

Figure 34: Schematic of TOF experimental setup used in Thunder Bay Research Institute for measurement of transient behavior in a-Se device with PI blocking layer.

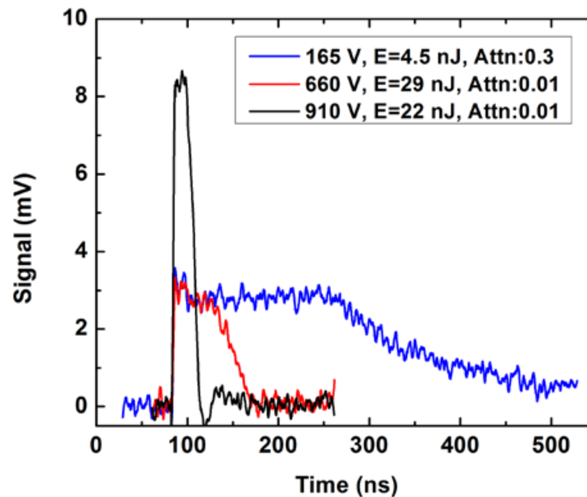

Figure 35: TOF signal from the 16.5 µm PI/a-Se detector biased at electric fields below avalanche regime. *E* refers to the energy of the laser pulse and *Attn.* refers to the transmission of the attenuator.

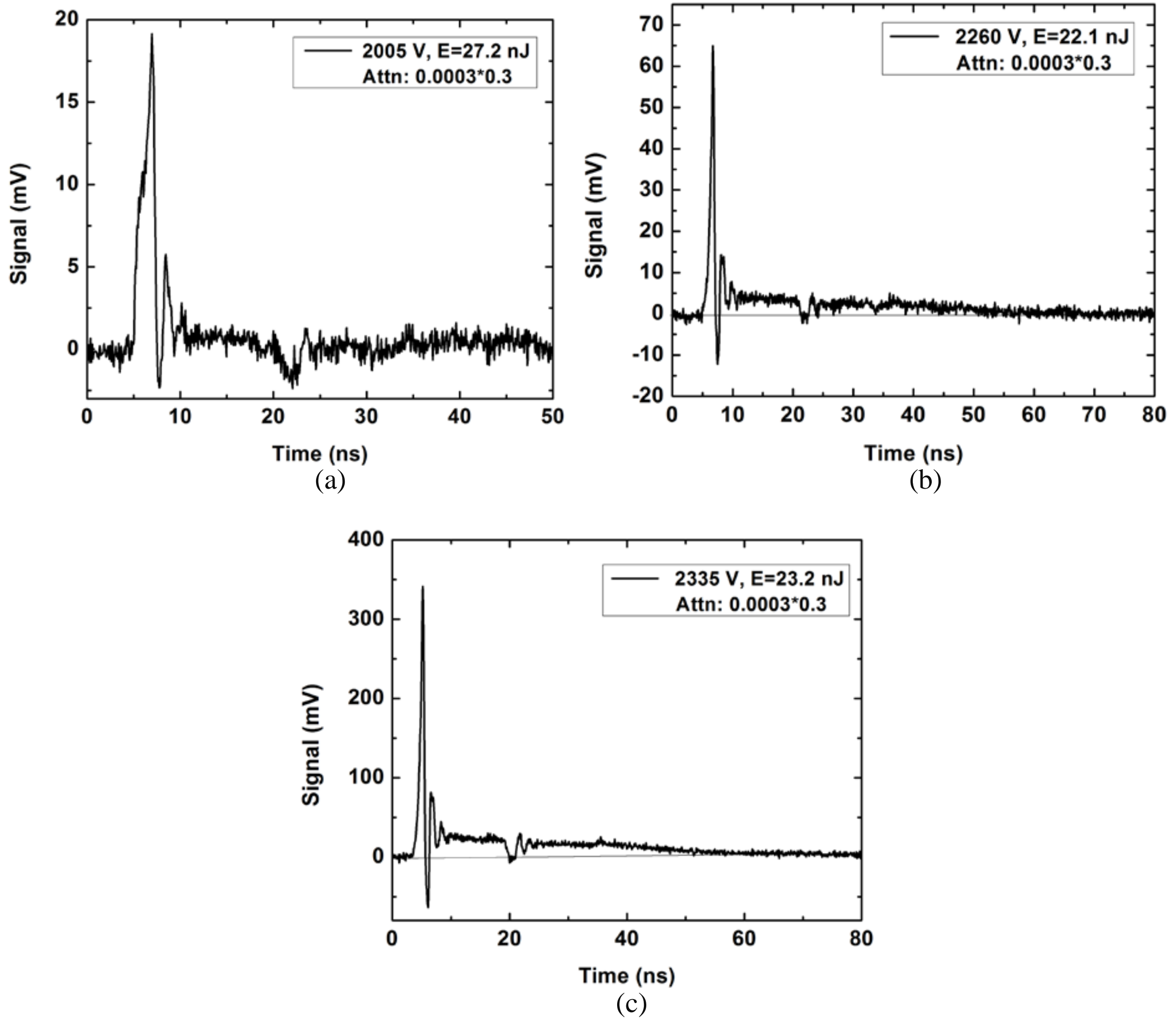

Figure 36: TOF signal from the 16.5 μm PI/a-Se detector biased at electric fields above avalanche regime. *E* refers to the energy of the laser pulse and *Attn.* refers to the transmission of the attenuator.

The current amplitude as a function of time in TOF measurements depends on the electric field as a function of depth in the device. As the electric field changes, the current amplitude as a function of time changes. As it is seen from Figure 35 hole transient response below the avalanche regime has a quasi-rectangular shape with well-defined knee that corresponds to the hole transit time t_h. The photogenerated electron's contribution to the photocurrent could be neglected due to the rapid collection of electrons by positively biased electrodes. These results are very promising that there is no significant charge trapping with in device.

The shape of the photocurrent at electric fields higher than 75-80 V/μm (the threshold for avalanche multiplication for devices with approximately 16.5 μm thick a-Se) contrasts those at fields

below avalanche. The transient response in the avalanche regime in Figure 36 increases rapidly due to impact ionization of holes and is followed by a long tail due to secondary non-avalanching electrons, which are much slower. Field dependence of hole drift mobility is shown Figure 37. Hole drift mobility μ_h is calculated using the hole transit time t_h derived from TOF measurement results which is then substituted into (5). Mobility increases by increasing the electric field in a-Se and reaches a value of 0.7 cm^2/Vs above 70 V/µm (in agreement with previously reported devices [88]).

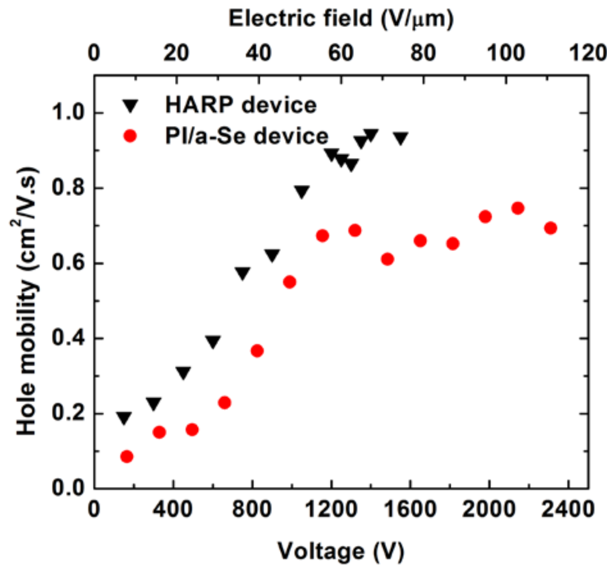

Figure 37: Extracted hole mobility over a range of electric fields applied to the 16.5 µm PI/a-Se detector (red circle) and 15 µm modified HARP structure. The difference in maximum value of the mobility in HARP and our device could be due to different quality of a-Se. The electric field values quoted were simulated based on partial capacitances of the PI/a-Se structure (Appendix C).

5.7 Vertical a-Se structure on CMOS substrates

Although TFT substrates are typically used for large area flat panel detectors, higher resolution panels can be achieved using CMOS substrates. Large areas are achieved by tiling several CMOS substrates together. To investigate the integration of the developed vertical detector with CMOS substrates, several CMOS dies were coated with the vertical detector. The integration of the detectors was verified by device dark current measurements.

The CMOS substrates, supplied by Teledyne DALSA, were approximately 2 cm x 2 cm with an active area of 2.56 cm^2 (Figure 38). The pixel pitch was 25 um. To be able to take advantage of the higher mobility of holes compared to electrons in a-Se the detector should be hole collecting. This means that the top electrode should be positively biased. For PI to be used as a hole blocking layer

would require the PI to be spin coated directly on top of a-Se. This is not practical because PI layer requires high curing temperature (350C) and would lead to crystallization of the underlying a-Se. Instead of PI we use PTCBI as the hole blocking layer.

Challenges related to the integration of CMOS with a-Se include strain at the a-Se/CMOS interface. As will be discussed in Chapter 7, a soft PI layer relieves the a-Se/substrate interface strain and prevents crystallization of a-Se. Therefore, we used a PI layer as a planarization layer on top of the CMOS substrate. Prior to PI coating the CMOS dies were cleaned with acetone and isopropyl alcohol in an ultrasonic bath. Reactive ion etching using oxygen gas was used to remove cured PI from the bond pads. After the PI was etched, a 50um thick a-Se layer was deposited. Next a 100 nm thick PTCBI layer was evaporated on the a-Se, followed by the deposition of a 50 nm gold contact (Figure 38). Shadow masks were used to cover the bond pads and prevent overlap at the edges. The fabricated devices were subsequently delivered to Teledyne DALSA for array level characterization using a specialized readout electronic board.

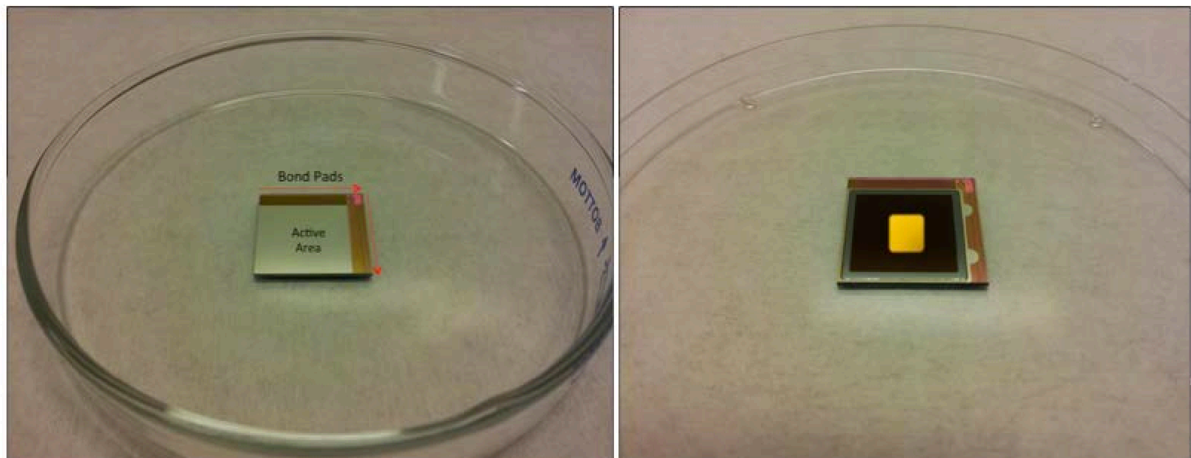

Figure 38: CMOS backplane prototype before (left) and after (right) detector layer coating.

The device dark current was measured using the University of Waterloo facilities for preliminary verification of the integration of a-Se on CMOS. To do so, a large aluminum electrode was deposited on the CMOS substrate prior to the spin coating of the PI layer. The result was a single pixel device on a CMOS substrate. Figure 39 shows the dark current for several bias conditions where the magnitude of the dark current is similar to that expected based on previous experiments on ITO glass in Chapter 4.

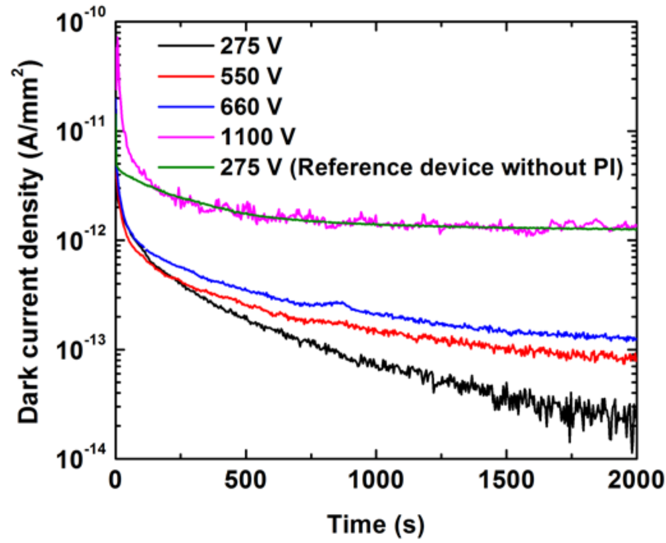

Figure 39: Dark current I-t curve for a vertical structure on CMOS substrate for different applied biases. The vertical structure consists of a 2 µm PI layer for planarization, 55 µm thick a-Se, 100 nm of PTCBI as a hole blocking layer and 50 nm thick Au as a top contact. The reference device is also a vertical structure on CMOS without any PTCBI as a hole blocking layer. All the measurements were done while Au contact was positively biased.

5.8 Conclusion

In summary, a wafer scale solid-state avalanche a-Se detector fabricated in-house at the University of Waterloo using a fully CMOS/TFT-compatible back-end fabrication process was demonstrated. The PI blocking layer suppresses dark current to below 200 pA/mm^2 at high electric fields greater than 80 V/µm without charge accumulation at the PI/a-Se interface, both essential conditions for safe and reliable operation of CMOS/TFT pixel level circuitry. Operating at electric fields above 70 V/µm enabled up to a factor of five increase in hole mobility that explains a significant improvement in detector speed (ns vs. µs) as evidenced by TOF experiments. The properties of the proposed detector make it a suitable candidate to replace a-Si:H p-i-n photodetectors in current flat panel CT technology. The main advantages of the detector are its capability of achieving gain above unity to approach a quantum noise limited system and its simple fabrication process compared with the fabrication of p-layer in p-i-n detectors. This research also extends avalanche a-Se detector technology to photon starved imaging applications and has the potential to usher in a new era of high speed, low light level, solid-state CMOS cameras.

Chapter 6

Development of high conversion gain a-Se photodetectors: Lateral structure

6.1 Introduction

Recently, lateral a-Se devices were reported [89] and integrated with a thin-film transistor (TFT) imaging array [90, 91] for indirect conversion X-ray imaging. These devices have the benefits of simple device structure, large area fabrication, and simple integration with TFT or CMOS processes, low cost, and high speed. Besides these benefits, there is no top contact in the lateral photodetector architecture that can undesirably absorb light before it reaches the photodector. One of the drawbacks of the reported lateral detectors is the significant increase in dark current with increasing applied bias [92]. As it was discussed before, high biases are desirable given the higher photogeneration efficiency [34] and carrier mobility [93] that result from increasing the electric field within the a-Se layer. In Chapter 4 and Chapter 5, a PI layer was shown to significantly reduce the dark current in the vertical structure. In this chapter, the results of using a PI layer for the lateral device are presented. Although the PI layer was investigated as a hole blocking layer, for simplicity, the same blocking layer (PI) is applied to both device contacts (i.e., it is used as a hole and electron blocking contacts). Figure 40 shows the lateral device structure with the PI blocking layer. Spin coating the PI layer over the whole lateral comb structure results in tremendous ease of fabrication. In order to pattern PI, a layer of metal must be deposited as a sacrificial layer and patterned to act as a mask for the PI layer against a reactive ion etching (RIE) process.

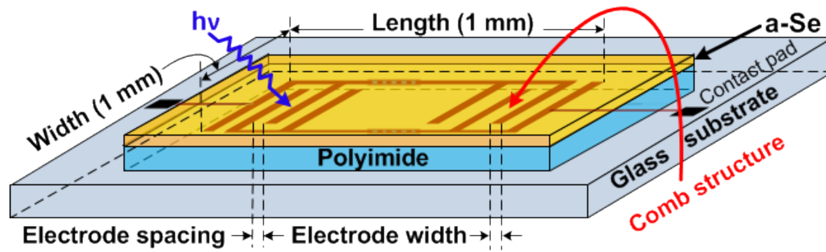

Figure 40: Lateral device structure (illustration not to scale).

6.2 Methods

The cross section of a lateral a-Se device structure is schematically shown in Figure 41 (a). It consists of metallic interdigitated comb electrodes (see Figure 41 (b)) patterned on a glass substrate that are subsequently covered by a thin layer of spin coated PI. A 2 μm thick layer of stabilized a-Se alloy (containing 0.2 % As and 5 ppm Cl) is then thermally evaporated on top of the PI layer. In this study, three different samples (S2-S4) were investigated with different electrode spacing (*d*) and electrode width (*w*) as indicated in Table 13.

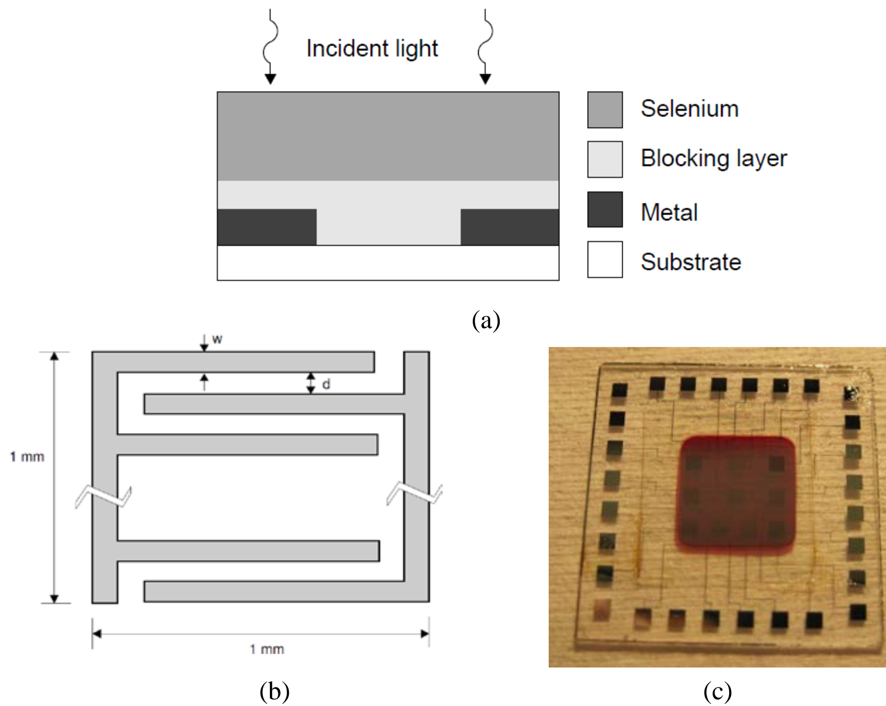

Figure 41: (a) Lateral a-Se device structure with blocking layer, (b) electrode schematic showing comb structure, and (c) photo of a total of 10 different device samples fabricated on the same substrate.

A reference sample (S1), containing no PI layer, was fabricated for comparison purposes and has the same electrode width and spacing as S2. As shown in Figure 41(b), the electrode lengths for all devices were 1 mm and the number of comb fingers varies between devices to keep the area consistent for all devices (1×1 mm^2). All devices were fabricated on the same substrate using identical layers, as shown in Figure 41(c), to allow for a meaningful comparison.

Table 13: Prepared lateral a-Se samples.

Sample #	**Electrode spacing (*d*) (μm)**	**Electrode width (*w*) (μm)**	**PI layer (nm)**	**a-Se layer (μm)**
S1	5	10	None	2
S2	5	10	800	2
S3	10	10	800	2
S4	5	5	800	2

The device structure was simulated to evaluate the expected field in the device, and the results are shown in Figure 42. The arrow length represents the field strength and it points in the direction of the electric field. The simulations indicate that, in spite of the blocking contact layer, there is still a significant field in the a-Se region of the device where the photogeneration of the carriers takes place. Figure 43 shows the electric field as a function of distance through a cross section of the lateral device at the top surface of the a-Se layer (red dashed line in Figure 42) where the non-uniformity of the electric field can be seen. The electric field within the 2 μm of a-Se does not decrease significantly towards the surface, varying approximately 7 % from the top of the PI layer to the top of the a-Se layer. The electric field is a very important parameter in defining the performance of a-Se based devices since the mobility and photogeneration efficiency of these devices depend strongly on the electric field within the device. In order to evaluate the device performance and specifically when we want to compare the lateral device with a vertical device, the average electric field is calculated and used for comparison of the different samples.

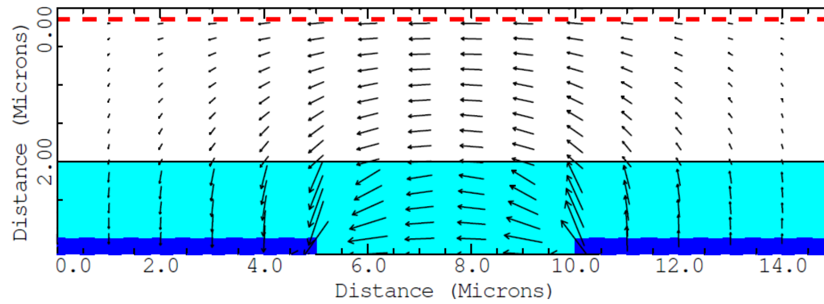

Figure 42: Simulated distribution of the electric field inside the detector using Medici, Synopsis Inc. The arrow length represents the field strength and it points in the direction of the field. The red dashed line represents the device region where the electric field in Figure 43 was calculated.

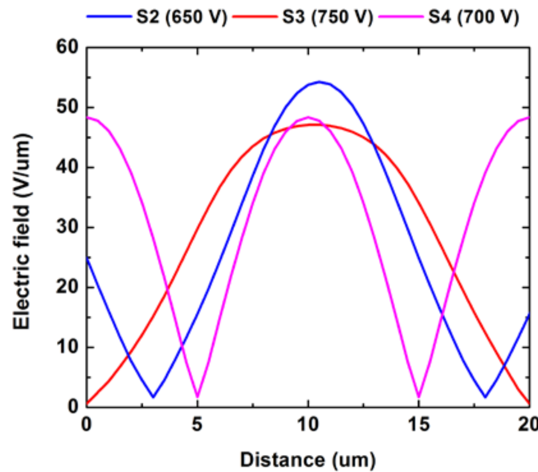

Figure 43: Simulated electric field across the surface of the detector for different samples (different electrode width and spacing). The troughs correspond to the area on top of the center of the electrodes.

The electric field inside the a-Se layer may be modified by charge trapping at the top surface of the a-Se layer or charge accumulation at the PI/a-Se interface. The penetration depth of the 468 nm wavelength photons is relatively small, leading to the generation of carriers at the surface. Since the field at the surface of the a-Se layer is parallel to the surface (see Figure 42), these generated carriers are not initially swept from the surface and may get trapped, leading to field modification near the surface and ultimately reduce the photo current for future exposures. The photogenerated carriers that reach the PI/a-Se interface can also accumulate at the interface. The field may then be reduced near the electrodes, leading to lower photocurrent for subsequent exposures. In order to verify whether the field is modified due to either of the aforementioned scenarios, consecutive pulse light experiments

were performed. The pulse duration was set to 20 s while the pulse period was 70 s. Reduction in the photo current for consecutive pulses would indicate that the field has been modified in the a-Se layer.

An Agilent semiconductor parameter analyzer (4156C) and a low-noise microprobe station were used to measure the device current and a Stanford Research Systems PS350 high-voltage power supply was used to bias the device. A blue LED (468 nm wavelength having an absorption depth in a-Se of 43 nm) with an intensity of 96 $\mu W/cm^2$ was used to study the photoresponse behaviour of the devices. The photocurrent of the device was simulated to estimate the effect of the photogeneration efficiency, recombination (e.g., near the surface), and trapping in the a-Se layer. The PI layer was not included in the simulations due to the uncertainties in modeling of the a-Se/PI interface and the carrier transport properties in PI used as a blocking contact. Instead the device was modeled in Medici similar to the device shown in Figure 42 without the PI layer and biased to reach the same average field as the device with the PI layer. The photogeneration efficiency was modeled using Onsager theory for blue (468 nm wavelength) light and was fit within the electric field range of interest using an exponential fit (see Figure 44):

$$f(x) = A - B\exp(-xC) \tag{9}$$

where A = 0.899, B = 0.803, C = 0.0295. Since the electric field in the a-Se layer does not change significantly with depth and the absorption depth of blue photons is relatively small (43 nm), the photogeneration efficiency was assumed to be constant as a function of depth. However the variation of the photogeneration efficiency parallel to the surface due to the non-uniform electric field was taken into account. Other relevant parameters for the a-Se model are summarized in Table 14 where bimolecular recombination was considered using the Langevin recombination coefficient [94].

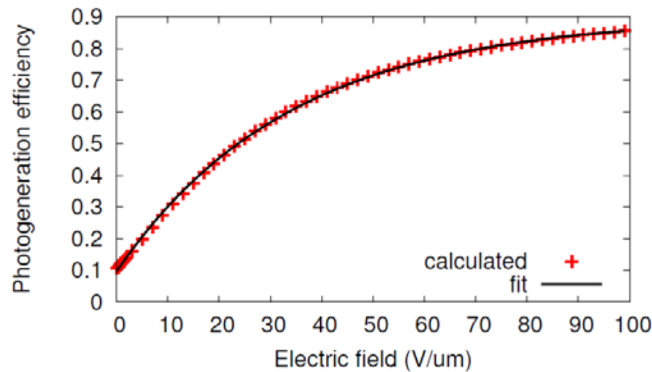

Figure 44: Photogeneration efficiency of a-Se at 468 nm wavelength using Onsager theory [9] and exponential fit.

Table 14: Medici a-Se model parameters.

Parameter	Value
Hole mobility (cm^2/V.s), μ_h	0.12
Electron mobility (cm^2/V.s), μ_e	0.003
Hole lifetime (s), τ_h	10
Electron lifetime (s), τ_e	100
Relative permittivity, ε_R	6.7
Recombination coefficient (cm^3/s), C	$e(\mu_h + \mu_e)/(\varepsilon_0\varepsilon_R)$

6.3 Dark current

To be consistent, the value of dark current versus time is recorded starting after 100 s for a total duration of 80 s. Note that the current density quoted for lateral devices is given by dividing the acquired current by the total device area (1 mm x 1 mm). The dark current results of a device without (S1) and with (S2) a blocking layer (PI) but having the same electrode spacing (5 μm) and width (10 μm) are shown in Figure 45 for different electric fields. It is evident that the dark current is significantly reduced when using the blocking layer. Since the photogeneration efficiency inside a-Se is field dependent (it increases with increasing field), higher fields within the a-Se layer are desirable.

In medical imaging applications it is also important for the dark current to be negligible, to maintain a quantum noise limited system (i.e., not limited by shot noise or electronic noise). Here an upper limit for the dark current to be on the order of 10 pA/mm^2 is used [95]. That is, the bias voltage is not increased further after such magnitudes of dark current are observed since they render the photodetector device performance impractical for medical imaging applications. Based on this restriction and looking at Figure 45, it is clear that operating a lateral a-Se MSM detector without a blocking layer at high electric fields leads to high dark currents which are not suitable for medical imaging.

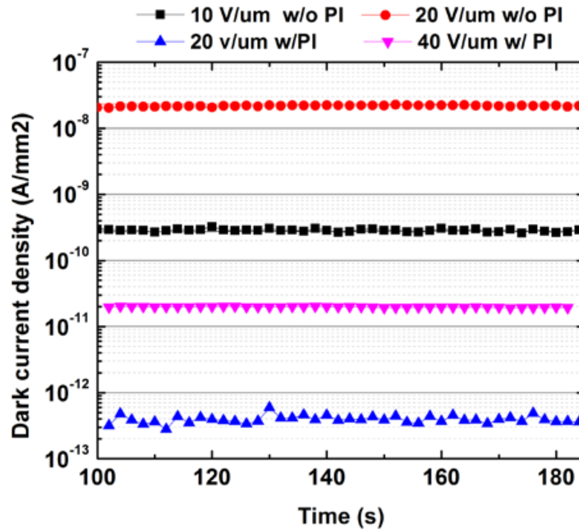

Figure 45: Dark current for devices (S1 and S2) with and without a blocking layer (PI).

6.4 Photoresponse

First the light source was periodically pulsed and the resulting response from S2 was examined for indications of field degradation. The response is shown in Figure 46 for two different applied electric fields (22 and 35 V/µm). As can be seen, the photocurrent is quite stable over time, suggesting that charge accumulation and surface trapping do not significantly impact the electric field within the a-Se layer.

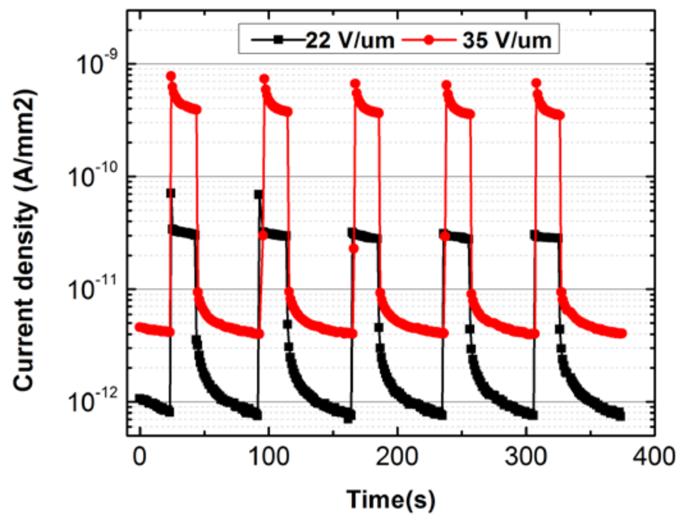

Figure 46: Response of S2 from periodically pulsed light at two different electric fields

The photoresponse of the devices without (S1) and with (S2) PI for a light intensity of 96 μW/cm^2 is shown in Figure 47(a) and (b), respectively. The photo-to-dark-current ratio of the device without PI layer can be seen to be much smaller than that of the device with a PI layer. The use of a PI layer in the device, as expected, also allows lower light intensities to be detected. For example, there was no distinguishable signal for the device without a PI layer (biased at ~10 V/μm) for a light intensity of 1.7 μW/cm^2 [96]. However this signal was clearly visible in a device with a PI layer. Comparing the results for S1 and S2, although the device with PI layer has a lower photo current, the lower photocurrent can be compensated for by increasing the electric field while maintaining a low dark current and thus a high photo-to-dark current ratio. Figure 47 (b) and Figure 48 (a) show the photoresponse of devices having the same electrode width (10 μm) but different electrode spacing (5 μm (S2) and 10 μm (S3) respectively) where the dark current is observed to be the lowest for S3.

Although all devices have identical exposure areas (1×1 mm^2), one difference occurs in that S2 has a larger number of fingers pairs (66) compared to S3 (50). This observation could help explain the observed dark current trend. However, we do not believe that this factor alone is sufficient to explain the observed trend for the photo current. Other factors can play a role, such as (a) the fraction of the device area occupied by electrodes, (b) fraction of photogenerated carriers that escape recombination, and (c) the magnitude of the electric field at each point within the cross section of the device as shown in Figure 43.

For the photocurrent, since the charge carriers are being swept away from the surface, the magnitude of the field at the surface greatly depends on the electrode spacing and width (factors (a) and (c)). On the other hand, carrier recombination is mainly affected by the electrode spacing since as the electrode spacing increases, the path that the carriers travel along the surface also increases, increasing the likelihood of recombination (factor (b)). Lastly, the contact electrodes occupy a fractional area of 0.67 and 0.5 for S2 and S3 respectively. Experimentally it was observed that S3 had the greatest photocurrent. The lower photocurrent of S2 (compared to S3) suggests that the total number of finger pairs is not the dominant effect for photocurrent.

Figure 48 (b) shows the results of S4 having an electrode width of 5 μm and spacing of 5 μm. The number of devices in S4 is 100 (which is greater than S2 and S3), while the fractional area occupied by electrodes is the same as S3 and the electrode spacing is the same as S2 but smaller than S3. The high dark current in S4 tends to agree with the previous conclusion that a higher number of finger pairs correspond to a higher dark current while the photocurrent of S4 is larger than all other samples.

For comparison, the photoresponse of S2, S3, and S4 are shown in Figure 49 for approximately the same electric field (~30 V/μm).

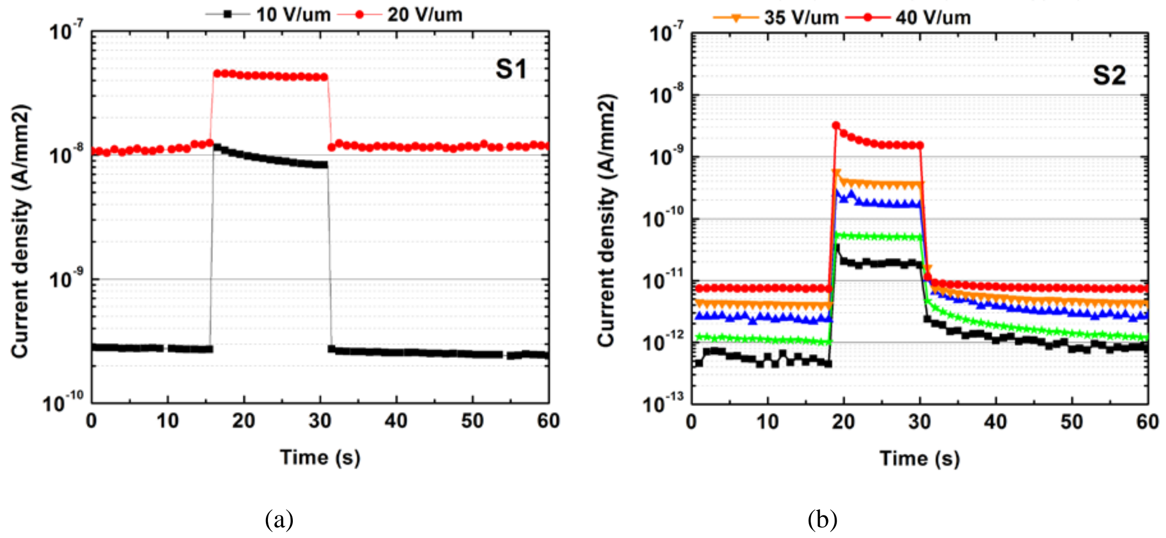

(a) (b)

Figure 47: Photoresponse of (a) S1 and (b) S2 for different electric fields.

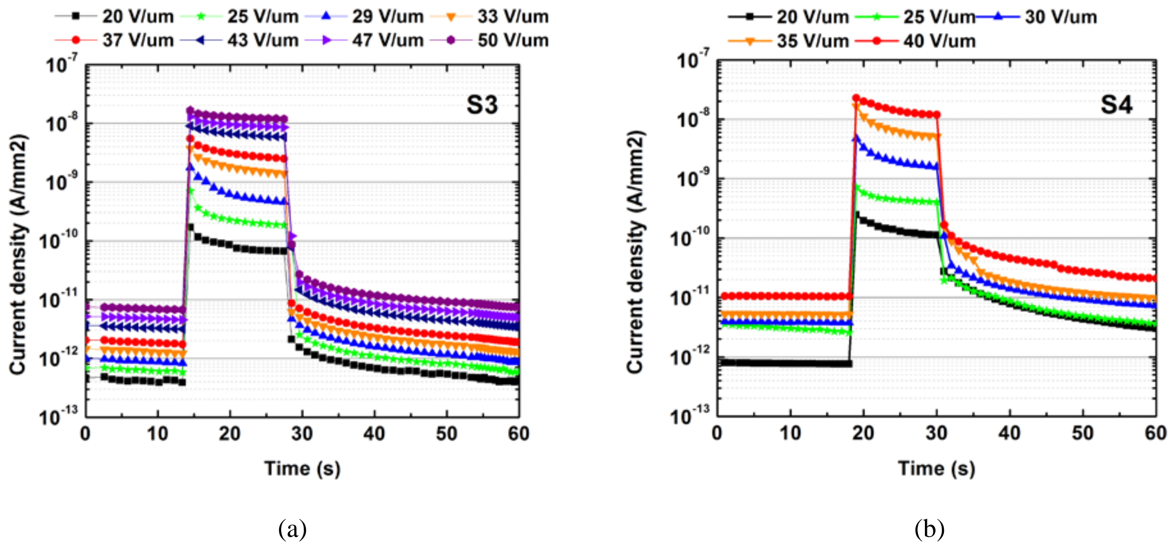

(a) (b)

Figure 48: Photoresponse of (a) S3 and (b) S4 for different electric fields.

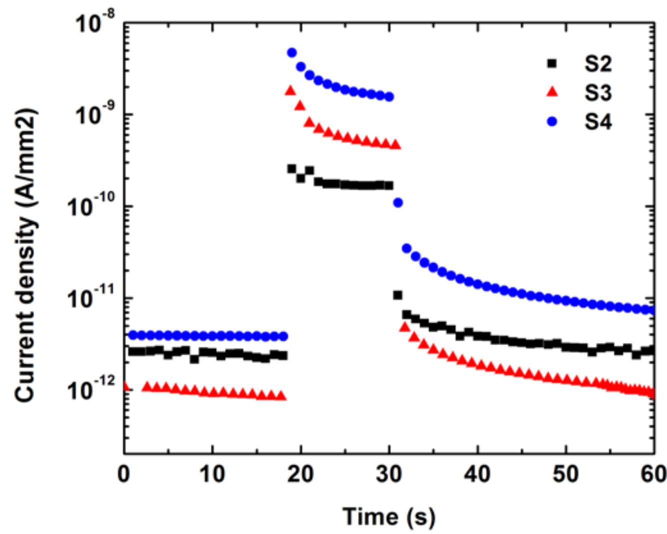

Figure 49: Photoresponse of S2, S3, and S4 at 30, 29, and 30 V/µm, respectively.

The photocurrent (sampled at the end of the light pulse) of samples S2-S4 is shown in Figure 50. The photocurrent was simulated for samples S2-S4 in Medici as a function of electric field to compare with the trends seen in the experimental results and to estimate the effect of photogeneration efficiency, recombination, and trapping. The device structure simulated differs from that of the fabricated devices and thus the exact magnitude of the current is not of particular interest. Rather, it is desired to gain insight from the observed trend with increasing electric field and field across the different device structures.

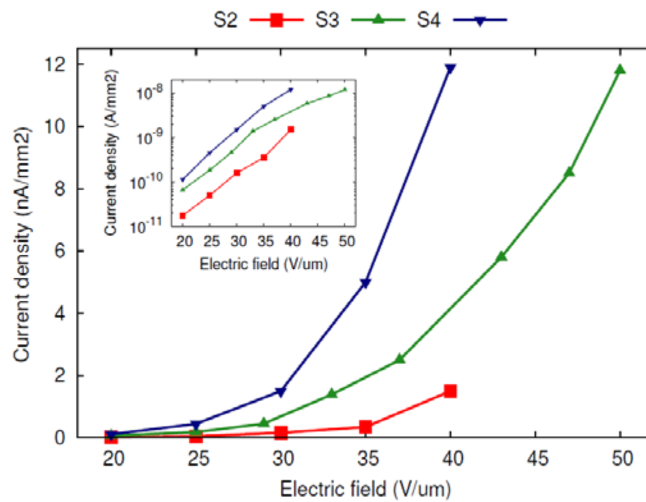

Figure 50: Photocurrent for different samples as a function of electric field in linear and logscale (inset).

The simulated results are shown in Figure 51. Comparing Figure 50 and Figure 51, the order of the samples with highest to lowest photocurrent is the same (S4 highest, S2 lowest). However the change in photocurrent as a function of electric field is noticeably different between the simulated and experimental results. The increase in photocurrent that accompanies an increase in field for the simulated results is most likely due to an increase in photogeneration efficiency and although recombination and trapping affect the results, especially in the low field region of the device, their contribution is not expected to be as significant as the photogeneration efficiency.

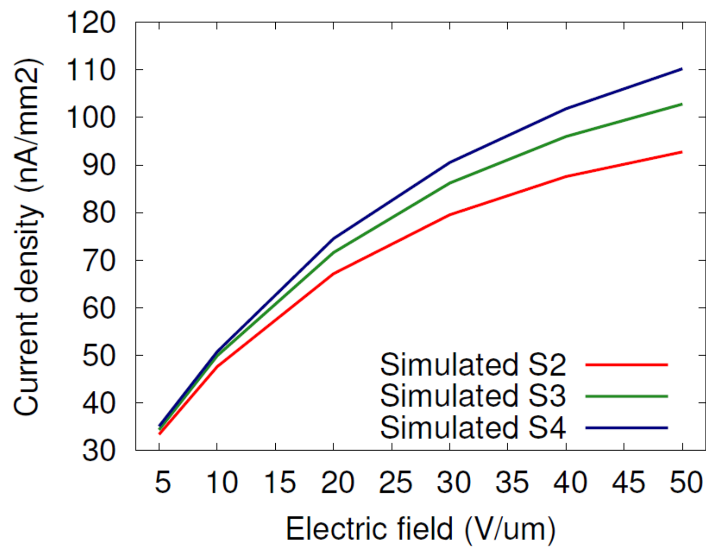

Figure 51: Simulated photocurrent for different samples as a function of electric field.

It should be mentioned however that there are discrepancies between the Onsager theory photogeneration efficiency and previous experimental results [34], especially at lower fields. The experimental photogeneration efficiency tends to be lower than the Onsager theory predicts. This may be one of the reasons for differences in the predicted and observed photocurrent. The differences may also be compounded by the use of the PI blocking layer in the experimental device. Interestingly a significant change in photocurrent at low fields was observed when using a PI blocking layer in a vertical a-Se device structure (see Figure 52). It is believed that the cause of the significant change (orders of magnitude) of photocurrent when increasing electric field over a small range (e.g., from 20

to 40 V/µm in the lateral device and from 10 to 30 V/µm in the vertical device) in the lateral and vertical devices are linked, however the reason for the significant change is currently unknown.

From the experimental results, S3 (10 µm width and 10 µm spacing) was found to have the most favorable properties when compared to the other samples: high photocurrent and low dark current. Although high photocurrent was observed for S4 (5 µm width and 5 µm spacing), the dark current began increasing to unacceptable levels at higher electric fields. For S2 (10 µm width and 5 µm spacing), a relatively low photocurrent was found while the dark current was high.

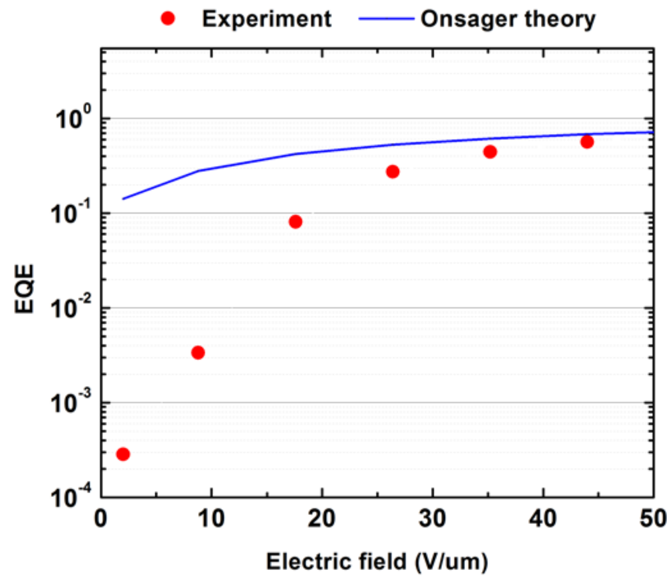

Figure 52: External quantum efficiency (EQE) for a vertical a-Se detector with a PI blocking contact exposed by a 468 nm wavelength source and Onsager theory photogeneration efficiency as a function of electric field. The EQE is given by dividing the photocurrent by the incident photon rate.

6.5 Comparison of lateral and vertical structures

Advantages attributed to lateral a-Se photodetectors, assuming the same exposure area as vertical based detectors, were discussed in Section 6.1. These advantages include its low capacitance and high speed. Besides these benefits, there is no top contact in the lateral photodetector architecture that can undesirably absorb light before it reaches the photoconductor. Aside from the benefits of the lateral device, there are also potential limitations such as an electric field parallel to the surface that may lead to increased trapping, and a limited fill factor due the finite width of the electrodes. In this section the performance of the lateral a-Se photodetector is compared with the vertical counterpart. In Section

6.4, the dark current and photoresponse of lateral devices with different electrode spacing and electrode width were shown. Considering S2 (d = 5 µm and w = 10 µm) and S4 (d = 5 µm and w = 5 µm), a vertical device with 5 µm thick a-Se and 1 µm thick PI as a hole blocking layer was sandwiched between ITO coated glass and an Au top electrode. It should be noted that since the electric field in the lateral device is not uniform, there is no direct comparison of the vertical and lateral devices. The goal is to compare the performance of a 5 µm thick a-Se layer in vertical devices with lateral devices with 5 µm electrode spacing (S2 and S4).

Figure 53 shows the photoresponse of the 5 µm thick a-Se vertical device for different electric fields using a blue light intensity of 96 µW/cm^2. Comparing the results presented in Figure 47 (b) and Figure 53 at the same electric field, the vertical device has a greater photocurrent while the dark current level stays approximately the same for both devices. At low electric fields (20 V/µm), the ratio of the vertical device photocurrent to the lateral device photocurrent is approximately 40. As the field is increased, this ratio decreases, reaching 10 at 40 V/µm. This shows the photoresponse of the lateral device can be made to approach that of the vertical device, as long as the dark current can be kept low.

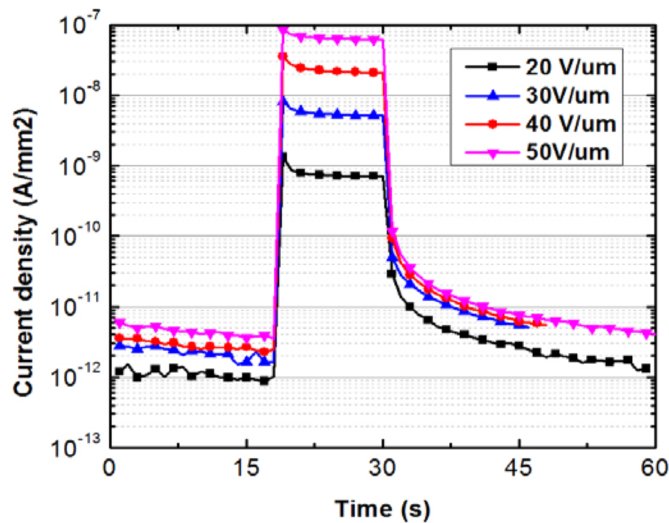

Figure 53: Photoresponse of the 5 µm thick a-Se vertical device for different electric fields. The light intensity was 96 µW/cm^2.

Comparing the results presented in Figure 48 (b) and Figure 53, the ratio of the vertical device photocurrent to the lateral device photocurrent reaches 2 at 40 V/μm. The dark current of vertical device is 4 pA/mm^2 and dark current of lateral device is 20 pA/mm^2. The reason for higher dark current in lateral device is that in order to increase the voltage within the a-Se layer we have to drastically increase the voltage across the device and the electric field at the sharp edge of the electrodes is much higher than the average fields that could lead to an increase in dark current. Since it is known that the dominant part of dark current is due to injection of holes from the positively biased electrodes, pattering the PI layer on one of the electrodes could be a possible solution for improving the performance of lateral device.

In order to study the effect of surface trapping, the lateral device (S2 with 10 μm electrode width and 5 μm electrode spacing) was exposed to light of different wavelengths. The rational behind this was that light that penetrates deeper in the device should lead to less trapping at the surface. To aid the analysis further, a vertical device (5 μm thick a-Se) was also exposed to the light of different wavelengths. Blue light (96 μW/cm^2) with an absorption depth of 43 nm and green light (91 μW/cm^2) with an absorption depth of 91 nm in a-Se were used. Trapping in the vertical device is expected to be negligible. The results are shown in Figure 54.

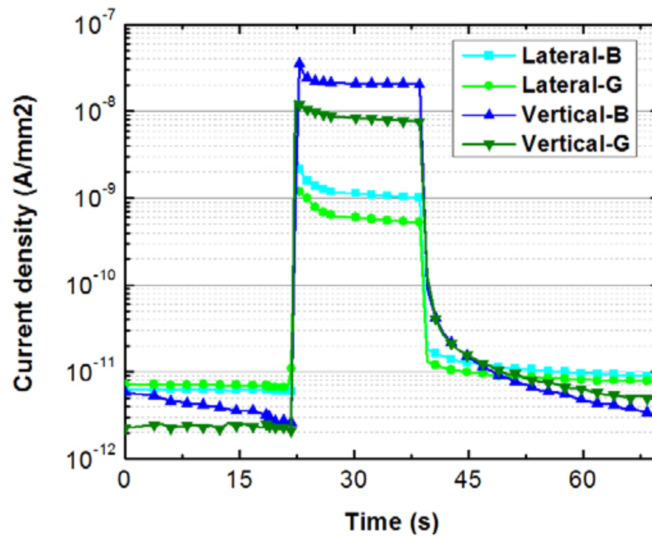

Figure 54: Photoresponse of the lateral and vertical devices, biased at 40 V/μm, exposed to green (G, 91 μW/cm^2) and blue (B, 96 μW/cm^2) light.

Using the Onsager theory, it was found that the photogeneration efficiency at 40 V/μm for blue light was approximately 0.66 while for green light it was approximately 0.32, giving a blue-to-green ratio of 2.06. This ratio is used as a guideline only, as the values were obtained from data fit from [34]. The blue-to-green photocurrent ratio for the vertical device was found to be 2.70. For the lateral device, this ratio was found to be 1.91. Although the reason for the decrease in this ratio may be due to several factors, one of those factors is surface trapping. Since blue light will tend to get absorbed closer to the surface, a decrease of the blue-to-green photocurrent suggests that trapping at the surface may occur.

6.6 Lateral a-Se structure on flexible substrates

With the advent of flexible TFTs, flexible electronics have become a viable technology. This technology may be leveraged for flexible imaging, however the detection and conversion materials that serve to convert the incident X-rays to collectable charge will also need to be flexible. In this section, the use of a-Se photodetectors on flexible substrates is investigated and the performance is compared with that of a-Se photodetectors deposited on glass. Figure 55 shows a-Se deposited on the flexible Kapton substrate. Devices were fabricated without a PI layer for simplicity. After deposition of a-Se on the flexible substrates, the devices were visually examined under the microscope. The quality of a-Se appeared to be similar to that deposited on glass substrates. Small bending angles were introduced and no peeling or flaking of the a-Se was observed.

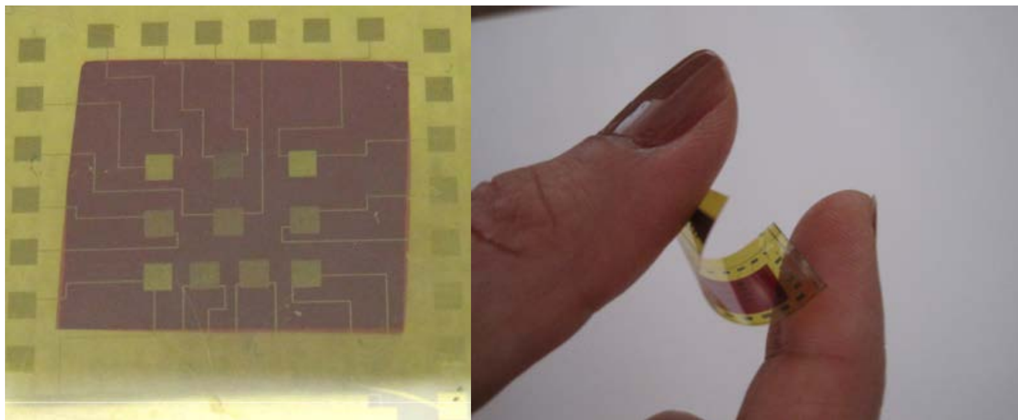

Figure 55: Lateral a-Se devices on a Kapton substrate.

To determine whether any major differences exist for the dark current and photo current, devices deposited on glass and flexible substrates (the lateral devices with 10 µm electrode spacing and 10 µm electrode width were used) were tested and compared. The results are shown in Figure 56 for the glass and Kapton substrates at different applied voltages.

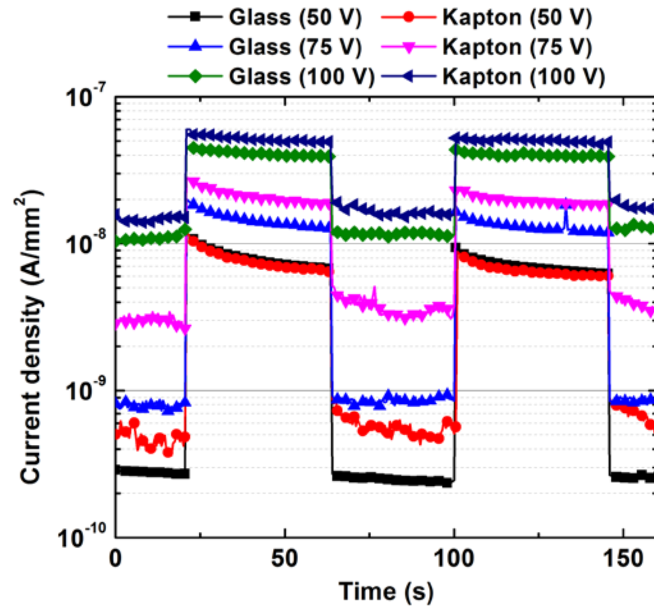

Figure 56: Photoresponse of the lateral device on glass and Kapton for different bias voltages, 50, 75, and 100 V. The blue light intensity was 96 µW/cm^2

For bias voltages of 50, 75, and 100 V, the peak electric field (occurring exactly between two electrodes) was 4.3, 6.5, 8.7 V/µm, respectively, and the average electric field was 2.4, 3.6, and 4.8 V/µm, respectively. The devices on the glass and flexible substrates show similar trends of increasing photo current and dark current with increasing bias voltage. At a bias of 50 V, both devices show comparable photo current, while the dark current of the flexible substrate device is slightly higher than that of the glass substrate device. At higher bias voltages (75 V and 100 V), the photo current and dark current of the flexible substrate device are higher than that of the glass substrate device. The slightly higher photo current in the flexible substrate device may be related to the higher dark current in the device since the photo to dark current ratio is small.

Next the devices were exposed to a different light intensity to see how the device response changed. The results are shown in Figure 57. The light intensity was increased by a factor of 2.5 while

the photo current increased in both devices by the same factor, 1.6. This demonstrates that the device behavior, as far as dark current and photo current are concerned, for devices on flexible substrates is quite similar to that of devices on glass substrates.

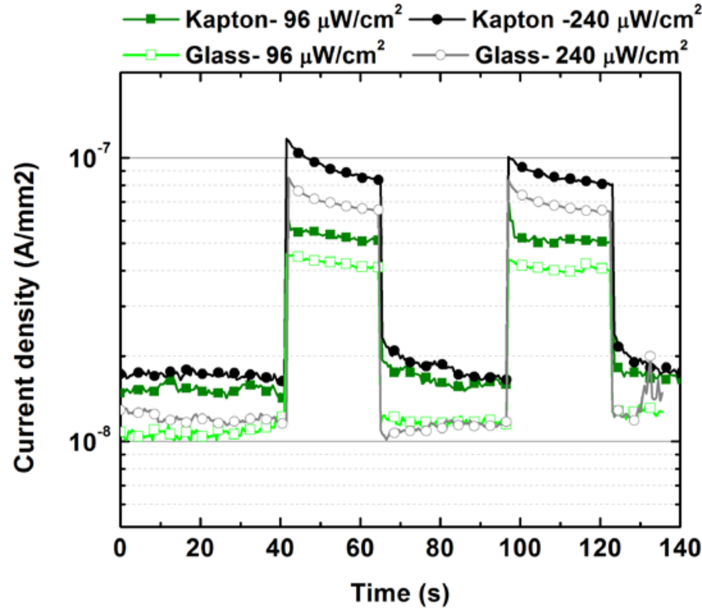

Figure 57: Photoresponse of the lateral devices on Kapton and glass substrates for different blue light intensities at a bias voltage of 100 V.

6.7 Conclusion

An a-Se-based lateral photodetector is reported that uses a PI blocking layer to lower the dark current at high electric fields. The PI layer prevents the injection of carriers from the device electrodes into the a-Se layer. Of the samples fabricated, the device with an electrode spacing of 10 μm and an electrode width of 10 μm showed the best performance with respect to both dark and photocurrent. The lateral device structure reported in this research can be implemented using simple post-processing steps to evaporate the a-Se layer following a standard a-Si TFT fabrication process, and allows for easy integration into current manufacturing facilities. Although a gain above unity was not observed for the lateral configuration, the photodetector performance improvements reported in this research provide the impetus to integrate lateral a-Se devices into large area active matrix imaging arrays for low cost flat-panel volume CT. If a gain above unity is required, a vertical configuration is preferred, at the cost of additional fabrication complexity.

Chapter 7

Development of high conversion gain a-Se photodetectors: Stability

7.1 Introduction

One of the initial steps in interaction of radiation (UV, VIS, NIR light, neutrons, γ-or X-ray) with matter is energy absorption and excitation of electrons and holes. This process induces changes of electrical conductivity in photoconductive material, it could even lead to chemical bond redistribution or reorientation, changes in chemical reactivity, reflectivity, index of refraction, to photo-darkening, photo-induced crystallization, and even melting or evaporation of the material. These effects are called photo-induced effects (PE) and can be reversible or irreversible. When high-intensity sources of radiation are used for excitation, the PE efficiency increases. After exposure, the excited states relax back to the original state or to a new state. These transitions happen after a time, either directly or by intermediate steps; it can involve changes in position of atoms individually or in groups. The relaxation time varies from picoseconds to years, depending on the structures, temperature, and wavelength of the excitation source [97].

In a crystalline structure, the PE changes of atomic structure are very confined due to dense packing of atoms and PE changes are small and they relax back after the exposure is finished. However, the situation in amorphous and glassy chalcogenides (AGC) is different. The disorder of these materials is high and their density is generally lower and a large free volume is available which is favorable for the formation of coordination defects. Amorphous selenium as many other chalcogenide glasses can undergo photo-induced structural transformation resulting in the red shift in the absorption called photo-induced darkening (PiD) or starts nucleation and crystal growth called photo-induced crystallization (PiC). Figure 58 shows permanent defects (white blemishes on dark

background) that appeared on a 25 μm HARP target after many hours of camera operation. In [98] it was concluded that these defects are associated with irreversible component of PiD.

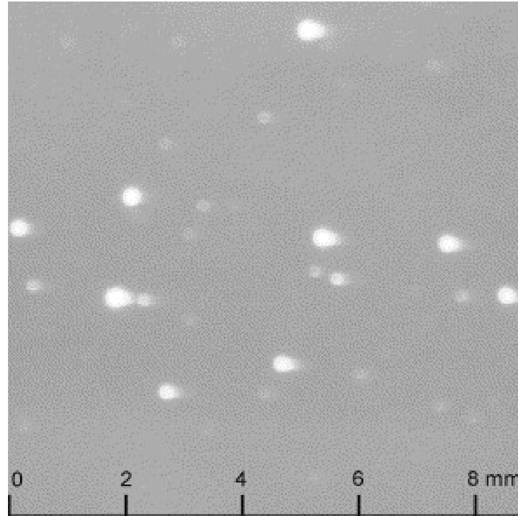

Figure 58: An image of permanent defects (white spots) region on a 25 μm HARP target[98].

The phenomenological model previously developed by Tanaka and Shimakawa suggests that PiD is caused by photo-induced conversion of some structural units from their ground state configurations into some metastable states that increase the level of disorder, broaden the band tails and hence, increase the absorption [99]. Using a double-well energy configuration, it was shown that the energy barrier between the ground state and a metastable state in pure a-Se was 0.8 eV [100]. A similar activation behavior was observed in PiC of a-Se studied by Raman spectroscopy [69]. This similarity suggests that the formation kinetics of PiD and PiC are controlled by the same configurational changes occurring via photo-induced metastable defects. Recently, the photocrystallization studies revealed that the interface between a-Se layer and the substrate significantly influenced the structural stability of a-Se: the onset time of the PiC was found to vary for different substrates (glass, polymer encapsulation, and thin blocking/buffer/ITO layers) [101].

In this chapter, the results are shown of investigating the stability of our evaporated a-Se films with 0.2 wt.% of arsenic deposited on different substrate against PiD and PiC. An understanding of the effect of a substrate on photo-induced structural transformation in a-Se is of great practical importance due to the application of a-Se photosensors in optical and radiation medical imaging. Indeed, structural changes can result in the permanent degradation of a-Se photoconductive

properties, which has to be prevented. The PiD experiment was done partially in collaboration with Dr. Rowlands' group at the Thunder Bay Regional Research Institute and the PiC experiment was done partially in collaboration with Dr. Weinstein in SUNY at Buffalo.

7.2 Experimental details

A 16.5 µm thick a-Se stabilized with 0.2% of As was deposited using vacuum evaporation technique in the same run on all three different substrates: glass, ITO-coated glass and PI-coated ITO glass. ITO glass was chosen as a substrate due to its potential applications in optical imaging. For instance, when a-Se must be biased, an ITO layer coated on a glass plate is typically used as the transparent electrode. Similarly, PI-coated ITO glass has its advantages as well to provide excellent blocking properties in the case of significant dark current at high fields. Figure 59 shows the structure of three samples studied in this work.

To study the PiD of the samples, we used the standard method of observing the changes in transmission as a function of exposure to light. Figure 60 shows the experimental apparatus that was used to carry out the PiD experiment. In this study, two laser beams with wavelengths of 633 nm were used to illuminate the same area of the sample. The less powerful probing beam was used to monitor changes in transmission of light, T. It is crucial that the intensity of the probing beam is low enough that it does not contribute to the PiD. The more powerful pumping beam, on the contrary, was used to produce PiD.

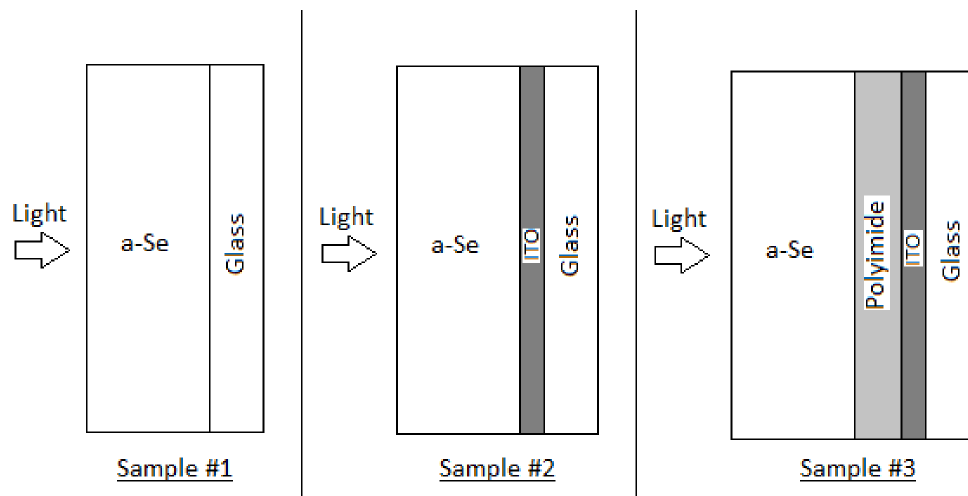

Figure 59: Structures of the different samples tested. Amorphous selenium was deposited on glass, ITO glass, and a PI-coated ITO glass.

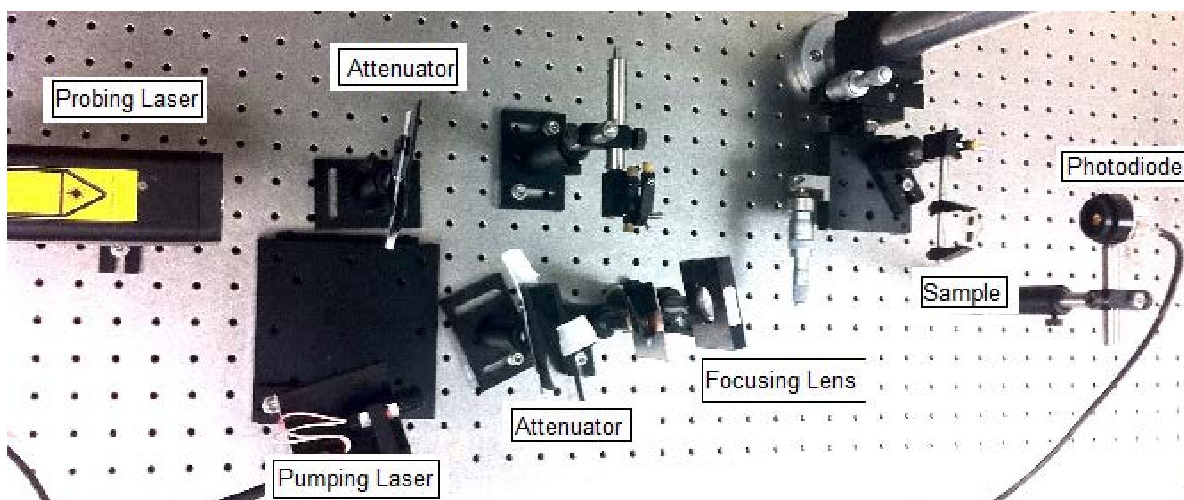

(a)

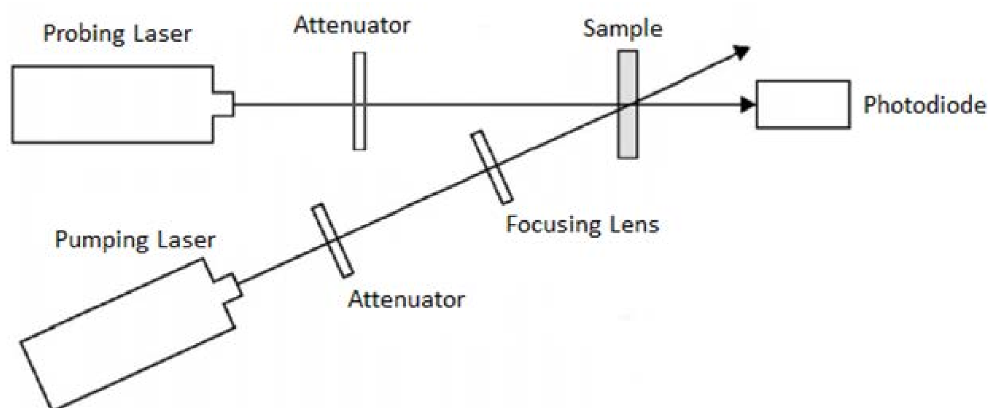

(b)

Figure 60: Experimental apparatus used to carry out the PD experiment.

The kinetics of the PiD were studied by periodically exposing the a-Se to the pumping beam for cycles of 200 s separated by 200 s of rest. During those cycles, the probing beam transmission, *T*, is continuously monitored and the relative changes compared to the original transmission of light, *T/T0*, were then calculated. The alternating cycles of pumping and resting were produced using a function generator. Measurements were taken at room temperature and repeated at 35 °C.

To study the PiC of the samples, Raman spectroscopy was used for temperatures below and above the glass transition of a-Se (T_g~313 K). The samples were illuminated through the glass substrate with a 647 nm laser at a flux of ~50 W/cm^2. The illuminated laser spot size was about 100 micrometers. A closed cycle helium cryostat and a heater were used to control the temperature.

7.3 Results

7.3.1 Photo-induced darkening

The results of the PiD measurements for the three different substrates at room temperature are shown in Figure 61 as a function of *T/T0* versus time for four pumping/resting cycles. All samples exhibit only partial recovery during resting cycles, leading to an overall decrease in transmission in subsequent cycles. Therefore, both reversible and irreversible components of PiD are present for all substrates. Figure 62 (upper) shows the relaxation of the PiD with time during a selected resting cycle (when pumping is switched off) for a-Se deposited on ITO glass. Although all samples exhibited partial recovery (see Figure 61), the experiment showed, however, that the transmission through the PI sample decreased the least, followed by the ITO sample and finally the glass sample. Since the magnitude of the irreversible PiD effect is proportional to the number of structural units which can be converted into a metastable state and provide the irreversible PiD, it is concluded that this number is the smallest for a-Se interfacing semi-soft material (i.e., PI) and the largest for a-Se interfacing rigid substrate (glass) where the strain at the interface is larger.

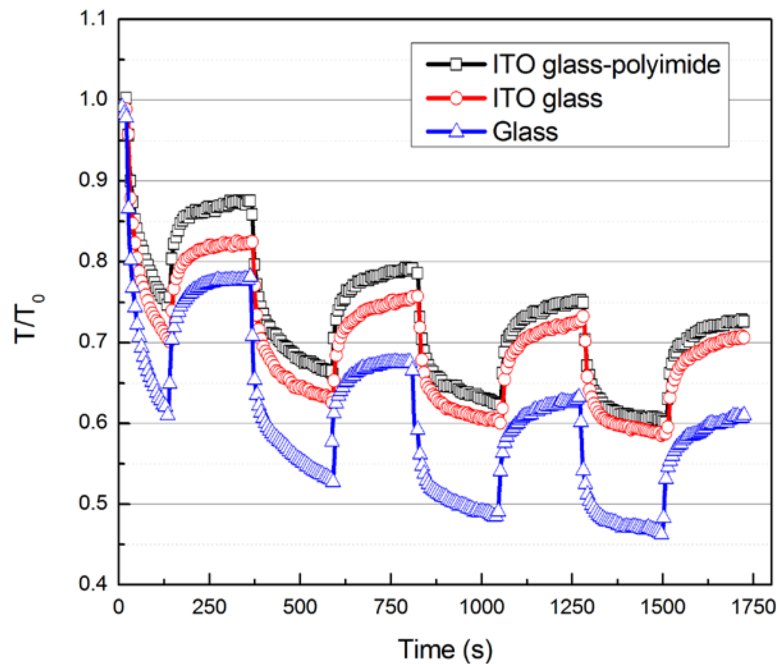

Figure 61: Normalized transmission as a function of time for the three samples at room temperature.

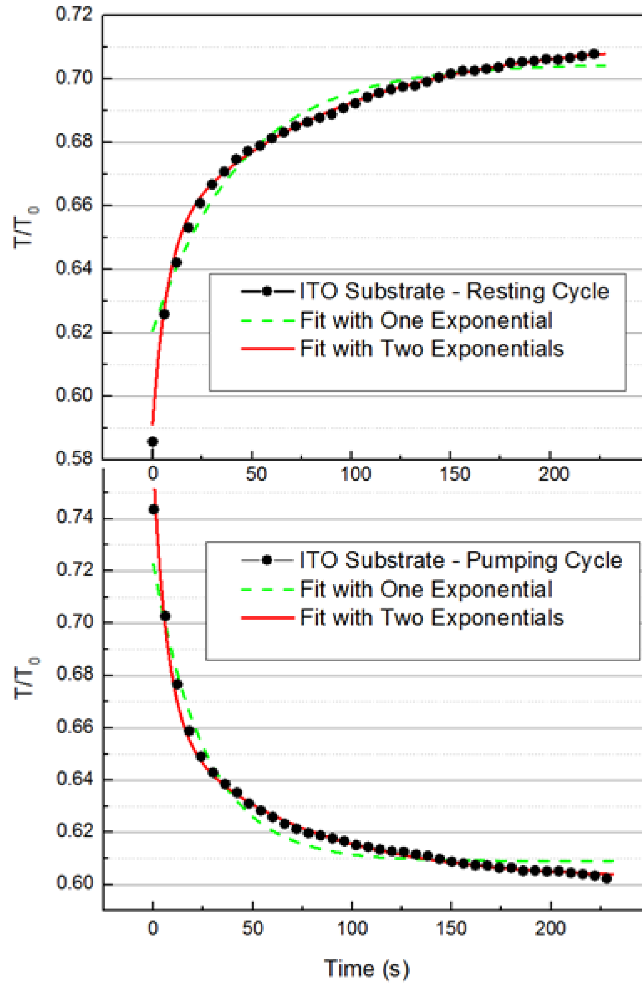

Figure 62: The recovery (upper part) and the decay (lower part) of the optical transparency for a resting/pumping cycles at room temperature.

In order to interpret the relaxation kinetics, the single state model [98] is first used, which was previously used to describe PiD in pure a-Se. In this model, during relaxation, transitions from metastable configuration back to initial ground state configuration occur through thermal activation over an energy barrier, E_B~0.8 eV (see Figure 63). As a result, the relaxation of the photodarkening can be fitted by single exponential decay with characteristic time constant τ that relates to the height of the activation energy as:

$$\tau = \nu_0^{-1} \exp(\frac{E_B}{k_B\theta}) \tag{10}$$

where k_B is the Boltzmann constant, θ is the temperature and ν_0 is the attempt-to-escape frequency of the order ~10^{12} s^{-1}. However, the single exponential decay fails to fit the experimental results. In contrast, double-exponential decay works much better as it is seen in Figure 62. The characteristic relaxation times τ_1 and τ_2 derived from fitting resting cycles are 8 s and 85 s, respectively, after averaging over several cycles.

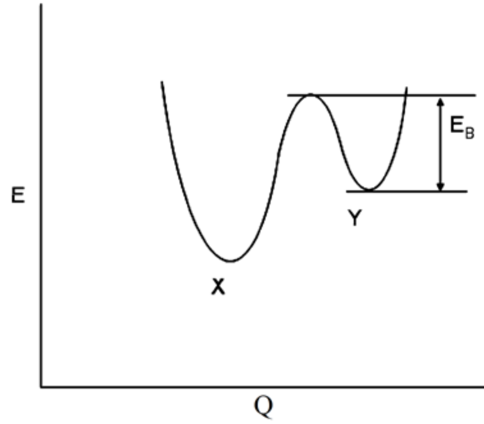

Figure 63: Energy-configuration diagram illustrating the energy barrier of transitions from metastable configuration back to initial ground state configuration.

The use of two exponentials to fit the data suggests that there may be two metastable states instead of a single in pure a-Se due to the presence of As in studied layers. For all of the substrates, the relaxation time of one of the exponentials, τ_1, is in the same range as the relaxation time previously found for the single state model (~10 s) [98]. This relaxation time is also similar between the different substrates tested. Conversely, the second relaxation time, however, is significantly longer meaning that the corresponding metastable state relaxes back through larger barrier.

It has to be mentioned that the kinetics of the PiD during pumping cycles can be modeled by double-exponential decay yielding the same τ_1 and τ_2 (Figure 62: lower part). Since a stretched exponential model was used by Shimakawa et al. [102] to model amorphous chalcogenides, a stretched exponential model was also investigated in this work. The stretched exponential model has the following form:

$$y(t) = y_0 + y_1 \exp(-\left(\frac{t}{\tau}\right)^{\beta}) \tag{11}$$

where y_0, y_1, τ, and β are fitting parameters and β<1. The stretched exponential results matched well with the double-exponential model and the results are summarized in Table 15. For further

comparison, the adjusted coefficient of determination (R^2) is included [103], which indicates the goodness of the fit (where a value closer to unity indicates a better fit).

Table 15: Relaxation parameters for different substrates using different models: single state model (single exponential and stretched exponential) and two state model (double exponential). The goodness of fit is included using R^2, where a value closer to unity indicates a better fit.

		Single exponetial		Double exponential			Stretched exponential		
		τ_1(s)	R^2	τ_1(s)	τ_2(s)	R^2	β	τ(s)	R^2
Glass	Resting	34.0	0.849	5.95	60.7	0.882	0.500	19.8	0.880
	Pumping	32.2	0.889	5.67	76.1	0.938	0.387	24.3	0.936
ITO	Resting	34.9	0.809	8.48	85.1	0.834	0.452	20.4	0.835
	Pumping	27.2	0.886	7.15	63.2	0.920	0.463	16.5	0.918
Polyimide	Resting	33.5	0.794	6.80	75.4	0.827	0.401	16.2	0.828
	Pumping	31.4	0.873	7.00	84.1	0.915	0.411	16.0	0.913

Figure 64 shows the PiD results at 35 °C for the glass substrate and the PI-coated substrate, as examples, where full recovery is observed. This agrees with previously reported results, where the irreversible component of the PD disappeared near the glass transition temperature [98].

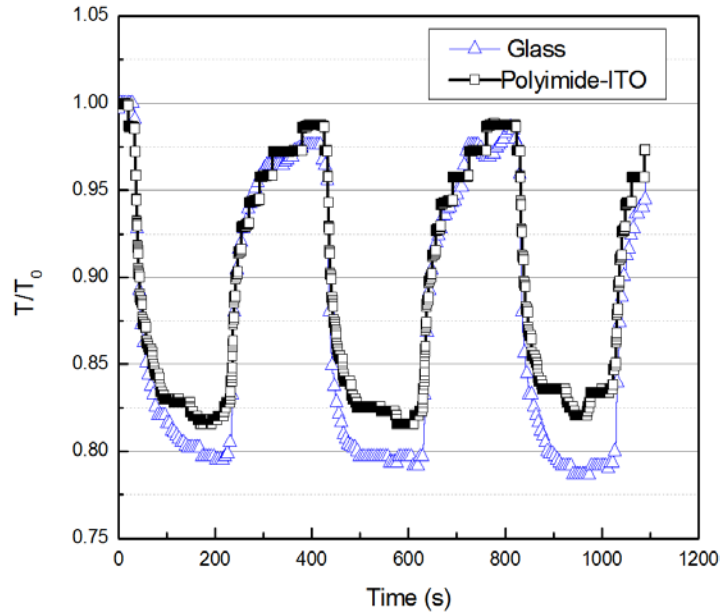

Figure 64: Normalized transmission as a function of time for two samples at 35 °C.

7.3.2 Photo-induced crystallization

Figure 65 and Figure 66 outline the Raman PiC results for a 16.5 μm thick stabilized a-Se film grown on glass, and on Polyimide coated glass. The Raman measurements were carried out at temperatures between 280 K and 343 K. The figures show the PiC onset time of crystallization for the a-Se film versus temperature. It is found that the onset time follows qualitatively the same trend as for the HARP sample in [101]. However, the PI coated sample showed the most striking difference. No PiC could be induced at any temperature studied in the experiment, as is evident in Figure 66(b).

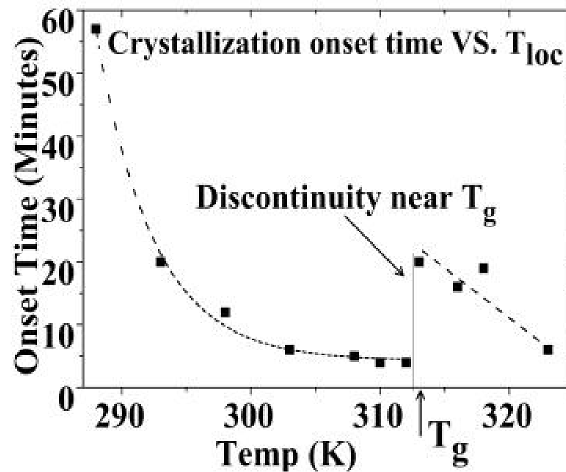

Figure 65: Onset time plots for PiC from 285 K to 343 K for a ~16.5 μm thick a-Se film grown directly on glass.

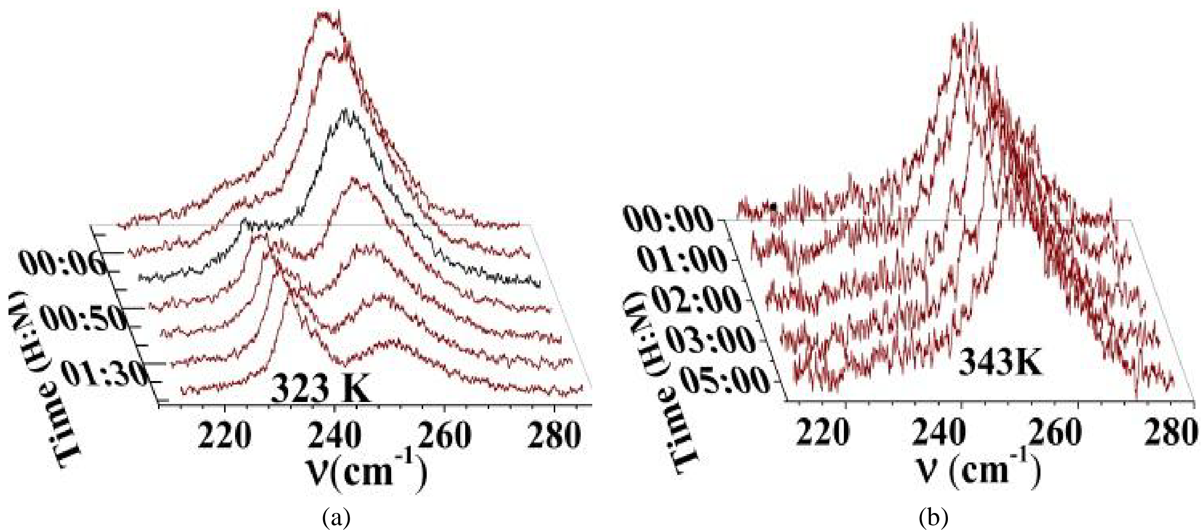

(a) (b)

Figure 66: Sample spectra for the PiC results at the most active temperature. (a) Shows growth of PiC in the a-Se sample on glass for 2 hours. (b) Spectra of an a-Se/polyimide/glass sample for 5 hours. No PiC occurs.

The model proposed by Stephens, 1980 [104], is used to explain the above results. In this model, shear strain at the a-Se substrate interface induces nucleation of the crystalline selenium (c-Se). The 12% volume difference between the a-Se and c-Se then sets up a strain field that continues to drive the growth below *Tg*. Near *Tg* the strain field anneals, slowing or halting c-Se growth, until at higher temperatures the PiC is promoted by thermal processes. The addition of the soft PI buffer layer relieves the a-Se–substrate interface strain and prevents the initial nucleation of the trigonal selenium, thus inhibiting the PiC in those samples. A similar mechanism can account for the positive effects of a soft buffer layer in reducing the PiD in a-Se films.

7.4 Conclusion

It was found that the substrate affects the magnitude of PiD significantly in stabilized a-Se: the more rigid the substrate, the stronger is the PiD. It is concluded that when a-Se is deposited on a rigid substrate, the number of structural units which are photo-induced to transform from their ground states (which are optically transparent) into metastable states (which cause PiD) is larger than in the case of a more flexible substrate. The model involving two different kinds of metastable states is used to explain the observed relaxation kinetics of PiD. At 35 °C, PiD in stabilized a-Se exhibits full recovery, as it was previously found in pure (non-stabilized) a-Se. It was found that a 1 μm layer of PI stabilized the a-Se film against PiC for T = 280-345 K. Technologically, this is very important because one challenge with currently sold a-Se detectors is that they suffer from long term reliability issues. Amorphous selenium layer tends to crystallize in random places leading to an increase in dark current making the detector ineffective to detect low levels of signal. By using PI as a base layer on the bottom of the a-Se layer, we can improve reliability and immunity to crystallization. These last two points will relax the temperature control requirements of the a-Se detector, which will be of benefit when considering a-Se detectors for flat panel CT.

Chapter 8

UV detection of microplasma emission by a lateral a-Se based detector

8.1 Introduction

As a practical demonstration of an indirect detection selenium device, the lateral detector was used in an example application, spectrochemistry. Since the implementation of the a-Se detector in a CT system has many hurdles, the spectrochemistry application was chosen as it was considerably simpler to demonstrate. Complications arise in the need for a pixelated readout circuit, synchronized x-ray tube, coupled scintillator, and image processing including reconstruction. The demonstration of a pixellated detector for flat panel CT is left for future work.

Optical detectors based on crystalline Si (c-Si), such as photodiode arrays (PDAs) and charge coupled devices (CCDs) have found considerable applicability in the field of plasma spectrochemistry [105]. But the indirect bandgap of 1.2 eV for c-Si causes considerable dark current at room temperature and reduces responsivity in the UV. For plasma spectrochemistry, most analytically-useful spectral lines lie in the UV region [105-109]. To increase responsivity in the UV, Si-based detectors are coated with fluorescent dyes (e.g., Lumogen, Metachrom). This increases quantum efficiency and cost. To reduce dark current (and thus improve SNR), cooling is required (e.g., -10 to -60ºC ± 0.1°C). But cooling hinders portability of miniaturized, plasma-based analytical instruments [109]. Materials with wider direct bandgaps, such as titanium dioxide, zinc oxide, or a-Se are attractive for detecting UV un-coated. An added advantage of a-Se is that due to its low dark current at room temperature, it does not require cooling. This enables portability for use on-site (i.e., in the field).

A low-cost in-house fabricated a-Se detector, described in Chapter 6, is demonstrated for detection

of photons in the UV region of the spectrum (e.g., from 200-400 nm). An advantage of the design is that the device structure allows photons to directly strike the light-sensitive a-Se layer rather than through electrodes or blocking layers. Another advantage is that despite operating at high electric fields (e.g., 30-40 V/µm) the dark current of the detector is less than 1 pA/mm^2. When combined, these two advantages provide a high light-to-dark current ratio. To determine the UV-response of the detector, emission spectra were scanned by attaching the detector to the exit slit of a scanning monochromator and a battery-operated, microplasma to its entrance slit. Spectral scans obtained using the monochromator were comparable with spectra measured using a fiber-optic spectrometer equipped with a linear CCD array-detector. To demonstrate detector sensitivity, emission signals with appreciable signal-to-noise ratios were obtained by introducing ng-amounts of diluted single element standards into the microplasma and by monitoring their spectral lines in the UV. For example, for Zn at 213.856 nm (10 ng), for Mg at 285.213 nm (5 ng), for Cu at 324.794 nm (10 ng), for Ag at 328.068 nm (10 ng), for Cd at 361.051 nm (5 ng) and for Mn at 403.307 nm (90 ng).

The objectives of this part of the project are two-fold: One is to document the UV spectral response of a lateral, a-Se detector in conjunction with a microplasma operated as a spectral lamp. And two, to demonstrate potential analytical applicability by obtaining signals with an appreciable SNR from ng-amounts of sample introduced into a portable, battery-operated microplasma for possible future analytical determinations on-site.

8.2 Experimental

The lateral a-Se detector used in this study is similar to S3 (operated at average field of 29 V/µm) in Chapter 6. The electrodes were 1 mm long and 10 µm wide and had an electrode spacing of 10 µm. Due to top illumination, there is no absorption of photons by electrodes or by blocking layers. The Cr electrodes were patterned on a glass substrate and were subsequently covered by a thin layer of spin-coated PI. A PI blocking layer was used to minimize dark current. A 2 µm thick layer of stabilized a-Se was thermally evaporated on top of the PI layer.

Conceptually, the experimental set up shown in Figure 67 consists of five parts: a scanning monochromator; an a-Se detector; a portable, fiber-optic CCD-spectrometer; a micro-plasma device (MPD); and a micro-sample introduction system. The monochromator was a 0.35 m focal length (Heath, Benton Harbor, MI) equipped with a scanning mechanism. The portable, fiber-optic spectrometer (StellarNet Inc., FL) had a focal length of 15 cm and it was equipped with a 2048-pixel

charge-couple device (CCD) linear detector and a 600 μm-diameter fiber optic cable. The entrance slit of the monochromator was adjusted so that both monochromator and portable spectrometer will have the same spectral bandpass. One side of the microplasma device (MPD) was affixed to the entrance slit of the scanning monchromator and the other side was viewed by the fiber-optic cable (Figure 67). Thus, microplasma emission could be monitored simultaneously.

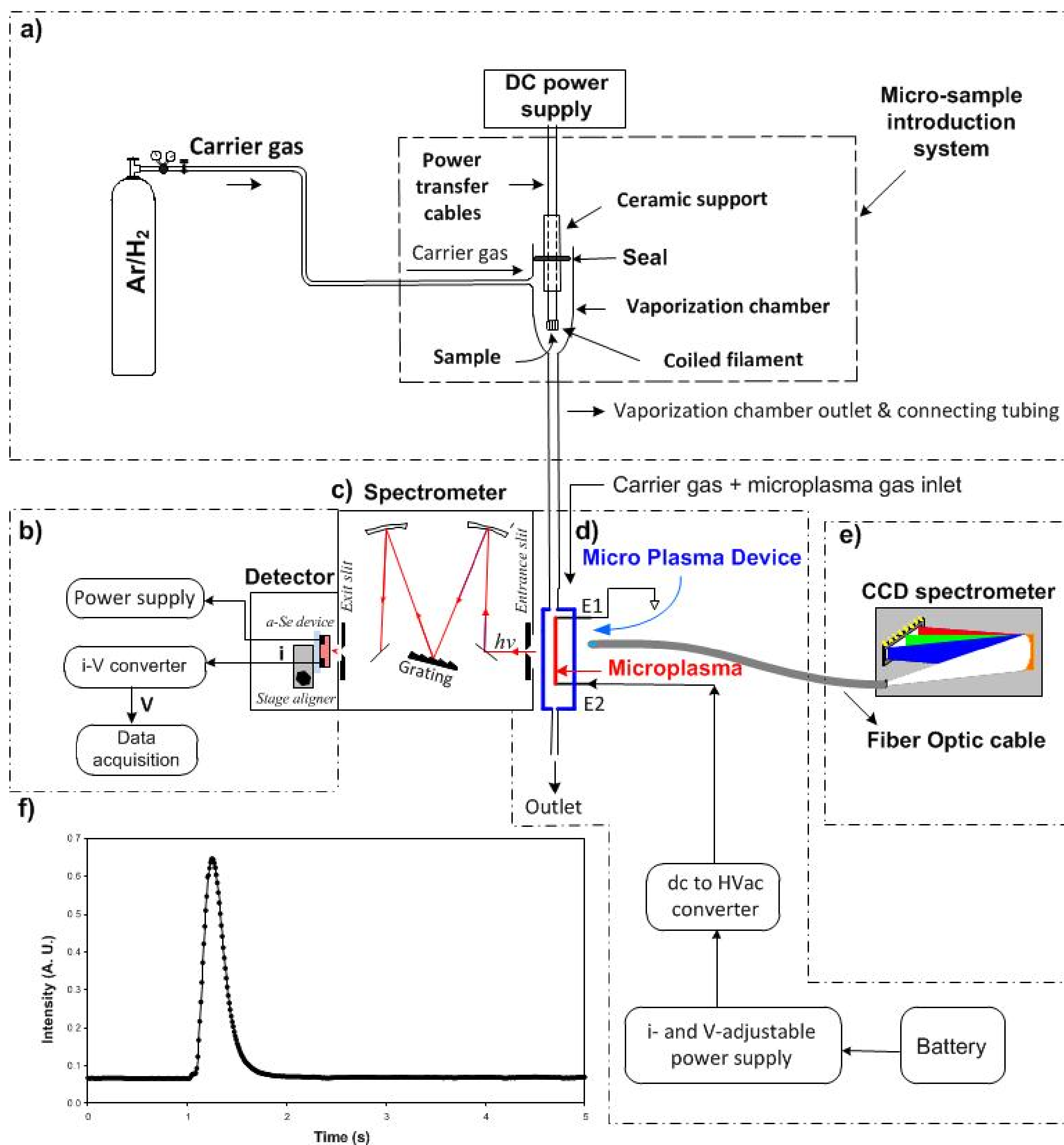

Figure 67: Experimental set-up of the UV experiment. (a) Micro-sample introduction system, (b) detector system, (c) spectrometer, (d) micro plasma device, (e) CCD spectrometer, (f) typical transient emission signal from data acquisition.

Initially, the ~800 μm diameter microplasma was used as a light-source that provided both broad background and spectral line emission. The rapidly prototyped MPD [106] was a hybrid plastic-quartz structure that had two stainless steel needle electrodes, a gas (and sample) inlet, and an outlet. The microplasma was formed between the needle electrodes and it was powered by a high voltage ac generated from a power supply driven by a rechargeable battery [107].

Typically, 10 μL of sample containing ng-amounts of diluted single element standard were first dried and subsequently vaporized into the microplasma using an electrothermal vaporization microsample introduction system. When introducing samples, a 3% Ar-H_2 mixture was used as the carrier- and the microplasma support-gas, and this was dictated by the micro sample introduction system.

8.3 Results and discussion

8.3.1 Spectral response

The spectral response of the detector in the UV (and visible) spectral regions was determined by scanning the monochromator fitted with the a-se detector and by employing the MPD as a spectral lamp (Figure 67). Spectral scans were compared with spectra obtained at the same time using the portable, fiber-optic spectrometer (Figure 67). The results are shown in Figure 68 (a) for a microplasma operated using an Ar-H_2 mixture as the plasma-gas and in Figure 68 (b) when Ar only was used as the plasma-gas.

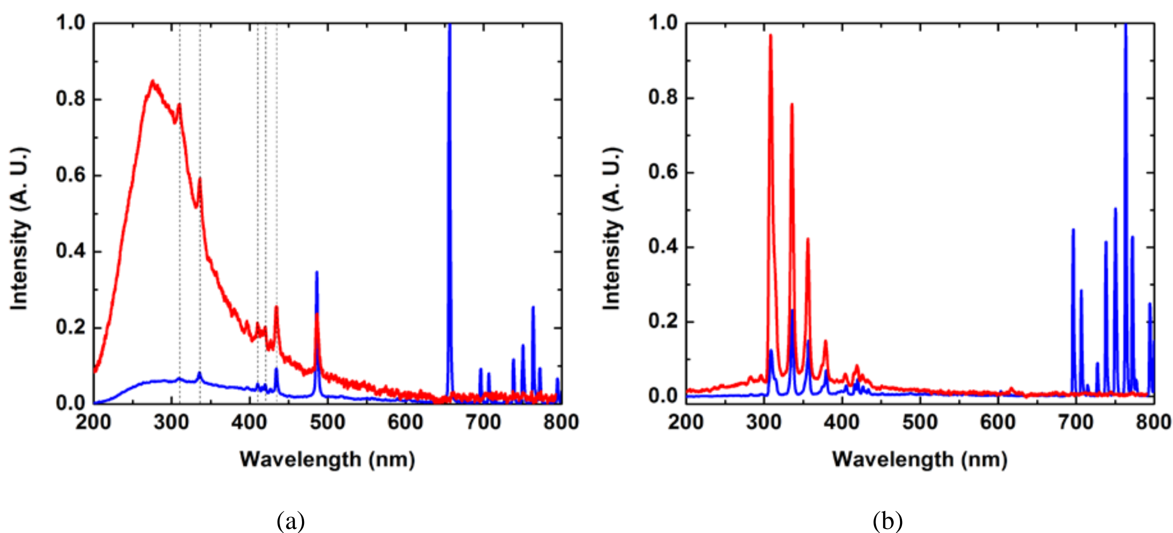

Figure 68: Microplasma background emission signals of (a) Ar-H_2 and (b) Ar only.

Although direct, quantitative comparisons are not possible due to use of different spectrometers and detectors, from the similarity of the spectral features it can be concluded that the a-Se detector has an appreciable UV response between 200 and 400 nm. The 200 nm cut-off was set due to atmospheric absorption (primarily from O_2). And although there is a report that a-Se responds to UV between 100 and 400 nm, spectra were not given [110]. The lack of response to wavelengths above about 650 nm can be explained by considering that 99.999%-pure a-Se powder has an optical bandgap of 1.99 eV [111]. Such a bandgap corresponds to 623 nm, thus pure a-Se powder is not capable of detecting any wavelength above about 623 nm. This is close to the 638 nm observed here, as shown in Figure 68.

8.3.2 Signal response

To demonstrate responsivity and to obtain a quantitative measure of detector response across the UV-range, the microplasma was used as an analytical source by introducing ng-amounts of sample into it and by measuring analyte emission temporal behavior. For instance, for Zn at 213.856 nm (10 ng), for Mg at 285.213 nm (5 ng), for Cu at 324.794 nm (10 ng), for Ag at 328.068 nm (10 ng), for Cd at 361.051 nm (5 ng) and for Mn at 403.307 nm (90 ng). 10 µL of sample containing ng-amounts of diluted single element standard were first dried and subsequently vaporized into the microplasma as it was explained in Section 8.2. Example signals are shown in Figure 69: Emission signals from Zn (10 ng), Mg (5 ng), Cu (10 ng), Ag (10 ng), Cd (5 ng), and Mn (90ng). From substantial SNR of these signals, it can be concluded that the lateral a-Se detector has good responsivity in the UV. These signals had SNR comparable with that obtained using the fiber-optic spectrometer [107]. Other comparisons are not possible due to differences in instrumentation. The precision (obtained using 10 ng Zn and the 213.856 Zn spectral line) was found to be 6.6 % relative standard deviation. Some examples are shown in Figure 70.

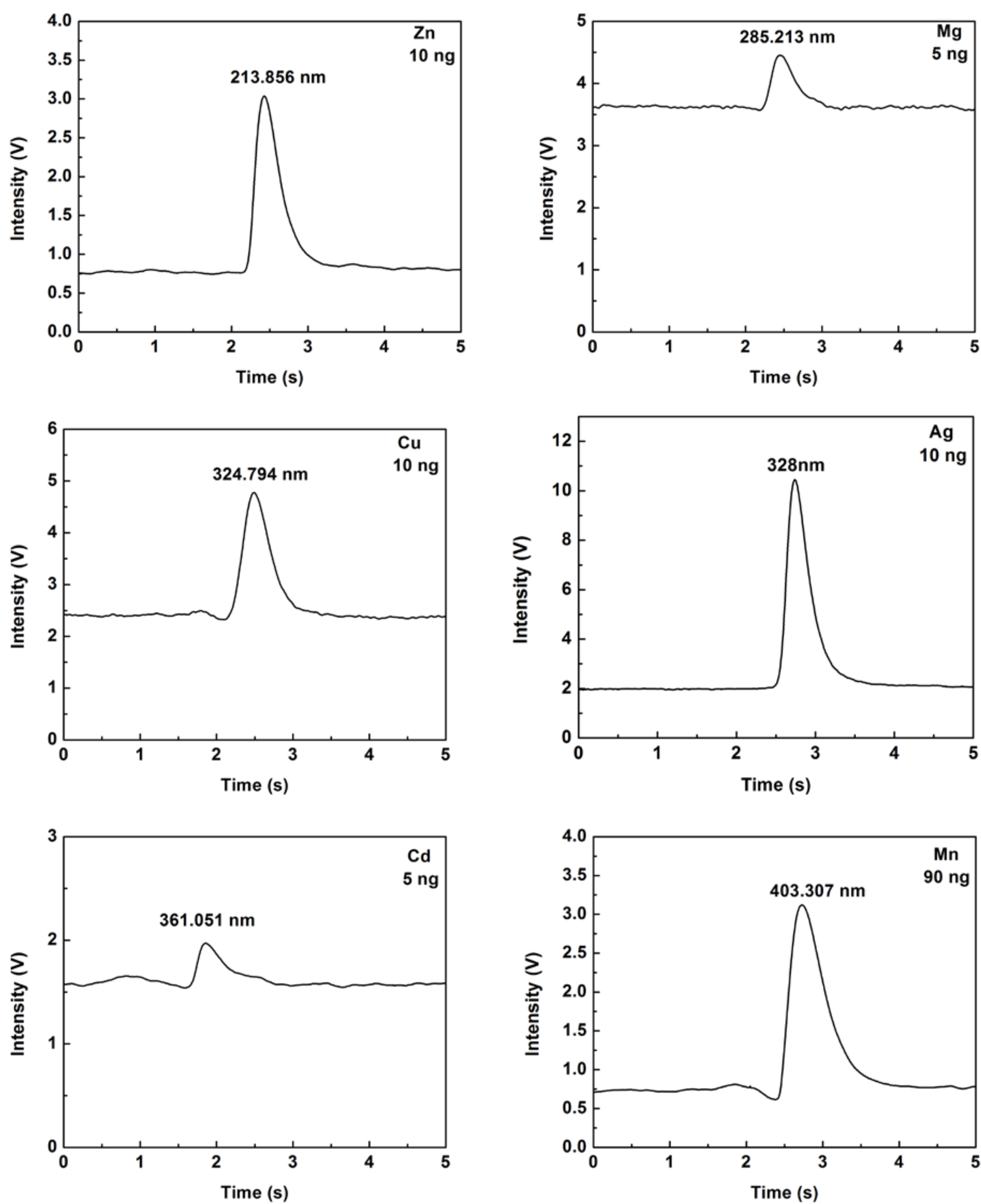

Figure 69: Emission signals from Zn (10 ng), Mg (5 ng), Cu (10 ng), Ag (10 ng), Cd (5 ng), and Mn (90ng).

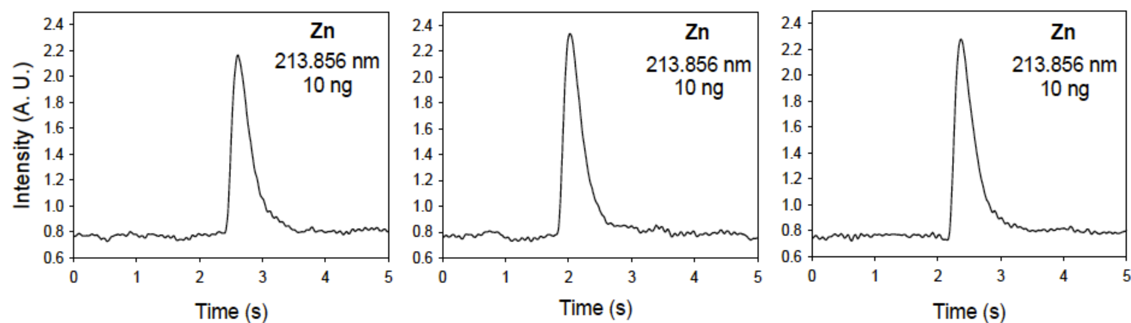

Figure 70: Precision (three consecutive analytical runs).

8.4 Conclusion

These proof-of-concept results demonstrate that the a-Se detector has the potential for use in spectrochemistry, especially for on-site measurements using portable microplasmas and spectrometers, thus warranting further investigation. The device structure can be easily fabricated using a single post processing step, specially, to evaporate the a-Se layer following a standard a-Si TFT or CMOS fabrication process.

Chapter 9

Summary, contribution, and future considerations

9.1 Summary

This work investigated the use of a-Se photodetectors for indirect conversion X-ray detectors for medical imaging applications. The properties of the ideal detector sought included: low dark current, high gain, high speed, compatibility with CMOS/TFT processes, and large area compatibility. Two detector structures were proposed and the results, summarized below, indicated that the vertical structure met the desired characteristics.

The project began with the deposition and characterization of a-Se films. The process parameters were varied to determine conditions that provided high quality a-Se films with decent electrical properties (carrier mobility and lifetime). To reduce the dark current to acceptable levels in an a-Se vertical structure several materials (CeO_2, TiO_2, PTCBI, and PI) with desirable properties for hole blocking layers were tested. PI, which uses a simple fabrication process, was determined to significantly reduce the dark current, even at high electric fields, and it was found to be the most appealing layer. Thus, PI was integrated in both the vertical and lateral structure designs.

Vertical structures using PI as a blocking layer were fabricated and tested. Specifically the photoresponse was measured for different electric fields. The absence of charge accumulation at the a-Se/PI interface was verified by consecutive pulse and long exposure time (> 10 hours) experiments. The transient response and linearity of the detector were also measured. A gain above unity was measured and TOF measurements were conducted to confirm that the gain was due to impact ionization. To verify the potential for integration with CMOS, the vertical structure was fabricated on CMOS substrates.

Lateral structures using PI as a blocking layer were fabricated and tested. Since the performance depends on the electrode spacing and width, several devices with varying electrode dimensions and spacing were fabricated. The measured dark current confirmed that PI is a good blocking layer for the lateral structure. The photoresponse was measured for the various fabricated detectors and it was determined that the device with 10 µm electrode spacing and 10 µm electrode width was the best. The performance of the vertical and lateral structures was compared where it was determined that the vertical structure performance was superior. The performance of the lateral structure suffers from the absence of a strong electric field covering the entire device area. Lateral devices were fabricated on flexible substrates and their performance was found to be comparable to those deposited on rigid substrates, indicating the possibility of these devices being used for applications flexible substrates, such as flexible and portable CT [112].

One appealing aspect of the lateral structure, namely the absence of a top contact, made it suitable for use as a UV detector. UV detection using the lateral a-Se detector was tested using microplasma emission. The a-Se detector showed high response in the UV-blue region of the electromagnetic spectrum. The detected emission peaks were confirmed by comparison with a CCD spectrometer. The a-Se detector was successful at detecting several to tens of ng of elemental samples. The results demonstrated that the detector has potential use in spectrochemistry.

Since a-Se is an amorphous material it is prone to stability issues such as photo-induced darkening and photo-induced crystallization. These two effects were studied for different substrates to determine the effect of the substrate on stability. It was determined that a PI layer on the substrate reduced the effect of photo-induced darkening. In addition, the use of a PI layer beneath a-Se prevented the a-Se in the device from crystallizing whereas the device without a PI layer beneath a-Se crystallized.

9.2 Contributions

This work has made numerous contributions to the imaging field. These contributions are summarized below:

- Developed two device structures (lateral and vertical) for detecting optical photons in indirect conversion X-ray imagers that can easily be integrated with CMOS or TFT processes
- Compared several organic and inorganic materials as hole blocking layers

- Investigated effect of substrate (and buffer layer) on a-Se stability (photo-induced darkening and photo-induced crystallization)

Vertical device structure contributions:

  - Developed avalanche capable a-Se detector (fabricated in-house at the University of Waterloo)
  - Verified avalanche gain in a-Se detector using TOF measurements
  - Fabricated and tested vertical device structure on a CMOS substrate

Lateral device structure contributions:

  - Investigated effect of electrode width and spacing on lateral device performance
  - Fabricated and tested lateral devices on rigid (glass) and flexible substrates
  - Demonstrated application of lateral structure as a UV detector (for spectrochemistry)

9.3 Future considerations

The detectors presented were primarily for indirect conversion X-ray detectors. However, the vertical device structure presented can easily be extended to direct conversion X-ray imagers. Work has already begun to realize such an imager in collaboration with Teledyne DALSA. The temporal performance of the detector structure has been investigated, however the modulation transfer function (MTF) and noise power spectrum (NPS) of the detector remain to be tested.

Higher carrier mobility than that of conventional a-Se direct conversion detectors (biased at 10 V/µm) can be achieved by applying a higher electric field (e.g., 40 V/µm). However, this comes at the cost of higher bias voltages, which can raise practical concerns since direct conversion a-Se detectors are much thicker (e.g., 200 µm) than the detectors investigated in this thesis. To prevent applying a large bias across the entire thickness of a-Se, which is more important if avalanche-enabling electric fields are desired, the detector may be split into two regions: (i) a conversion region, and (ii) an avalanche region [113-115]. The conversion region is a thick a-Se layer having typical electric field (10 V/µm) that serves to convert X-rays into detectable charge. The avalanche region is a thin a-Se layer having a sufficiently high electric field to achieve avalanche that increases the signal of the now-converted detectable charge. Since this layer is thin, the bias voltage requirements are relaxed.

Aside from the vertical structure, there is also potential future work for the lateral structure. Since holes are the dominant source of dark current for a-Se detectors, the blocking layer (PI) need not be deposited on both comb electrodes. In this work, for simplicity, the blocking layer was spin coated over both electrodes. Having the blocking layer only deposited on the positively biased electrode may allow for higher fields within the a-Se layer closer to the negatively biased electrode, while still maintaining low dark current. Such a modified structure would however require the addition of a patterning step to the fabrication process. Photoconductive materials other than a-Se can also be tested using this structure, such as a-Si:H [116, 117].

Another aspect of this work that could be extended is the integration of a scintillator with the a-Se detector. In this work LEDs were used to mimic the scintillators. Preliminary experiments were conducted with a scintillator (CsI:Na) [118], however the characterization of the scintillator crystal used proved difficult. Although it is suggested to use CsI:Na due to its spectral matching with a-Se, other materials are of course possible. Integration of a scintillator would allow for the device to be tested under the exposure of X-rays.

Appendix A

Onsager formulation

The Onsager theory characterizes geminate recombination. It considers Brownian motion (random motion), columbic attraction, and the external applied electric field on the dissociation of photogenerated electron and hole pairs in material. A brief explanation of theory is summarized below [34, 35].

First consider an electron-hole pair initially separated by distance r_0 due to thermalization and having an angle θ with respect to the electric field. To calculate the probability that carriers would escape recombination, Onsager solved the diffusion equation in the presence of an electric field (the Smoluchowski equation) at steady-state by using two extreme boundary conditions: one is the stationary flow with a source at the origin and a sink at $r = \infty$ and the other is a source at infinity and a sink at $r = 0$. The probability that carriers escape recombination, $f(r, \theta, E)$, is given by the ratio of the flow into the sink at $r = \infty$ to the flow into the source and is given by:

$$f(r, \theta, E) = \exp(-A)\exp(-B)\sum_{n=0}^{\infty}\sum_{m=o}^{\infty}\frac{A^m}{m!}\frac{B^{m+n}}{(m+n)!} \tag{12}$$

where

$$A = \frac{e^2}{4\pi\epsilon\epsilon_0 rKT} \tag{13}$$

and

$$B = \left(\frac{erE}{2KT}\right)(1 + \cos\theta) \tag{14}$$

Using the probability of dissociation and initial distribution of thermalized electron-hole pairs, g(r,θ), the overall photogeneration efficiency is defined as:

$$\Phi(E) = \Phi_0 \int f(r, \theta, E)\, g(r, \theta) d^3 \tag{15}$$

where Φ_0 is defined as the efficiency of production of thermalized electron-hole pairs per absorbed photon and is assumed that is not dependent on the electric field. The initial distribution of carriers may be approximated by a delta function isotropic in space which can be written as:

$$g(r, \theta) = \delta(r - r_0)/4\pi {r_0}^2 \tag{16}$$

Carrying out the integration in (4) leads to the following solution for escape efficiency or quantum efficiency:

$$\Phi(\mathrm{r_0, E}) = \Phi_0 \frac{\mathrm{kT}}{\mathrm{eEr_0}} \exp(-\mathrm{A}) \exp\left(-\frac{\mathrm{eEr_0}}{\mathrm{kT}}\right) \sum_{\mathrm{m=0}}^{\infty} \frac{\mathrm{A^m}}{\mathrm{m!}} \sum_{\mathrm{n=0}}^{\infty} \sum_{\mathrm{l=m+n+1}}^{\infty} \left(\frac{\mathrm{eEr_0}}{\mathrm{kT}}\right)^{\mathrm{l}} \frac{1}{\mathrm{l!}} \tag{17}$$

Where A is same as (2) for $= \mathrm{r_0}$.

A critical Onsager distance $\mathrm{r_c(T)}$ is defined as that distance at which the Coulomb energy is equal to kT:

$$\mathrm{r_c(T)} = \frac{\mathrm{e^2}}{4\pi\epsilon\epsilon_0 \mathrm{KT}} \tag{18}$$

Accordingly, the first few terms of (6) can be written as:

$$\Phi(\mathrm{r_0}, E, T) = \Phi_0 exp\left[-\frac{\mathrm{r_c}}{\mathrm{r_0}}\right] \left\{ \begin{array}{c} 1 + \left(\frac{e}{kT}\right) \frac{1}{2!} \mathrm{r_c E} + \left(\frac{\mathrm{e}}{\mathrm{kT}}\right)^2 \frac{1}{3!} \mathrm{r_c} \left(\frac{\mathrm{r_c}}{2} - \mathrm{r_0}\right) \mathrm{E^2} \\ + \left(\frac{e}{kT}\right)^3 \frac{1}{4!} \mathrm{r_c} \left(\mathrm{r_0}^2 - \mathrm{r_0 r_c} + \frac{\mathrm{r_c}^2}{6}\right) \mathrm{E^3} + \cdots \end{array} \right\} \tag{19}$$

It can be concluded that photogeneration efficiency approaches unity provided that photogenerated carriers diffuse apart a distance larger than $\mathrm{r_c}$ before they thermalize. Otherwise geminate recombination reduces the creation of free carrier pairs. Since the rate of energy loss for a hot carrier is expected to be high due to the short mean free path, a substantial amount of excess kinetic energy is needed to prevent thermalization of carriers at a distance shorter than $\mathrm{r_c}$. This predicts the dependency of photogeneration efficiency on photon energy, external electric field and temperature [34].

Appendix B

Calculating electric field when charge accumulates at PI/a-Se interface

It was experimentally verified that there is no significant charge accumulation at PI/a-Se interface by pulsing the light on and off and observing the amplitude of the photocurrent. In order to determine whether the light intensity used in our experiment could create a significant drop in the electric field if charge accumulation occurred at the PI/a-Se interface, we solved Poisson's equation [119, 120] in the a-Se layer. The following assumptions have been made in this case:

- All photogenerated electrons are trapped (due to the presence of PI layer) uniformly within the absorption depth (43nm). All photogenerated holes are assumed to get collected without getting trapped.
- Only the effect of the electrons on the electric field is considered (i.e., the effect of photogenerated and travelling holes on the electric field is not considered).
- The light, incident on the same side of the a-Se as the PI, is shined with a constant intensity.
- Each incident photon generates an electron-hole pair and the recombination of electrons and holes is neglected.

The parameters used for the calculation are summarized in Table 16 and Table 17. Figure 71 shows the cross section of a vertical device structure and the changes in the electric field within a-Se layer. The negative charge at the a-Se/PI interface increases as a function of time since the light is shined continuously and the electrons are accumulating.

Table 16: Light parameters.

Parameter	**Value**
Wavelength	468 nm (blue light)
Intensity	170 $\mu W/cm^2$

Table 17: a-Se parameters.

Parameter	**Value**
Thickness, L	15 μm
Absorption depth, t_{abs}	43 nm (for 468 nm wavelength light)
Relative permittivity	6.7
Applied electric field	9 V/μm

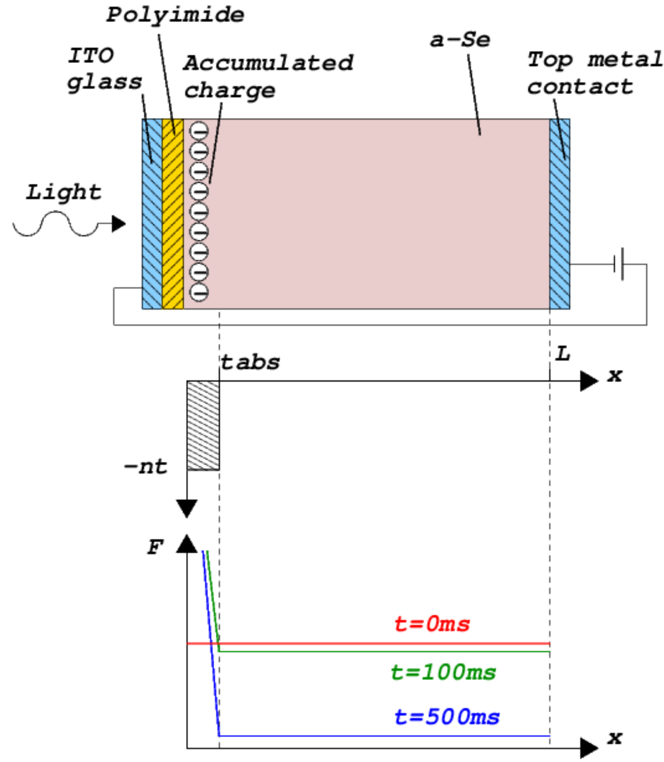

Figure 71: Electric field within the vertical device structure. Note that the curves in this figure are not to scale, they are approximations for visualization purposes.

In order to solve Poisson's equation, first the concentration of the trapped electrons was calculated (n_t) based on the incident light intensity:

$$n_t = N_{\mathrm{ph}} / t_{abs} = 9.33 \times 10^{19} \times t \ (\mathrm{cm}^{-3})$$

where N_{ph} is the number of incident photons per unit area and t is the light exposure time. The concentration increases linearly with the time the light is left on. Based on the calculated value of n_t, it is possible to calculate and plot the electric field as a function of depth, x:

$$\frac{\partial F}{\partial x} = -\frac{e}{\varepsilon} n_t \qquad (20)$$

where F is electric field, x is distance along a-Se thickness, and ε is permittivity. It was found that $\partial F/\partial x = -2.52 \times 10^{17} \times t$ (V/m^2). Since ∂x = 43 nm, the absorption depth, and the trapped concentration was assumed to be uniform in ∂x, then $\partial \mathrm{F} = -1.08 \times 10^{10} \times t$ (V/m). Solving for the boundary condition equation [119, 120] will give the absolute value of the electric field over L:

$$\int_0^L F dx = V_{appl} \tag{21}$$

where V_{appl} is the applied voltage to the a-Se layer. For 9 V/μm, we need 135 V (= V_{appl}). Using the above equation, the electric field in the a-Se bulk, F_b can be found (see Figure 72).

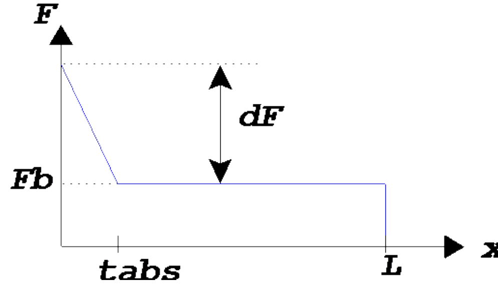

Figure 72: Electric field within vertical device structure, indicating the field within the a-Se bulk, F_b.

The electric field in the bulk can then be determined for different exposure times. From Table 18 it can be seen that if the photogenerated electrons had accumulated at the PI/a-Se interface, the electric field within the a-Se layer would have significantly diminished after approximately 500 ms. However, for the experiment the light was pulsed for 7 s and no significant degradation in the photocurrent was observed, suggesting that charge accumulation at the a-Se/PI interface was not significant.

Table 18: Bulk electric field in a-Se for different light exposure times.

Exposure time, *t* (ms)	**a-Se bulk electric field, F_b (V/μm)**
0	9
100	7.45
500	1.26

Appendix C

Additional notes for electric field simulation

In order to estimate the electric field within the selenium layer from the voltage that was applied across the device (PI/a-Se structure), the device was simulated using MEDICI, Synopsis Inc. In the simulation the electric field within the a-Se layer is calculated from the partial capacitances of the PI/a-Se structure. However, it should be noted that the simulation does not include the resistivity of PI and a-Se and the resistivity changes as a function of electric field. In this case the contribution of change in hole mobility to the conductivity is:

$$\sigma = e\mu_h P = e\mu_h \left(N_v e^{-\frac{E_f - E_v}{KT}} \right) \tag{22}$$

where the effective density of states in a-Se is $N_v = N_c = 10^{19}/cm^3$, $kT = 0.0256\, e\text{V}$, and $0.1 \leq \mu_h \leq 1$. As it is shown in Table 19**,** one order of magnitude increase in the hole mobility leads to one order of magnitude decrease in the a-Se resistivity. As a consequence, if the change in the resistivity of a-Se is taken into account, the electric field within a-Se does not increase linearly with increasing biasing voltage.

Table 19: Parameters used for resistance calculation

Relative permittivity (ε_{PI})	2.9	**Relative permittivity (ε_{a-Se})**	6.7
Thickness (d_{PI})	0.0001 cm	**Thickness (d_{a-Se})**	0.0016 cm
Area (A_{PI})	0.01 cm^2	**Area (A_{a-Se})**	0.01 cm^2
		$E_f - E_v$	1 eV
		σ (μ_h=0.1)	1.735E-18 $(\Omega.\text{cm})^{-1}$
		Resistance (μ_h=0.1)	9.21E16 Ω
		σ (μ_h=1)	1.735E-17 $(\Omega.\text{cm})^{-1}$
		Resistance (μ_h=1)	9.21E15 Ω

It should be noted that the electric field will saturate at a value E_{max}, which means a higher electric field could not be achieved within a-Se by increasing the biasing voltage. The value of E_{max} depends on the thickness of a-Se (E_{max} decreases as the thickness of a-Se increases) and its doping level [53]. The reason for saturation of the electric field within the a-Se layer is due to the initiation of impact ionization by electrons. As the biasing voltages increase, electrons will have enough energy to start impact ionization and at some field the number of electron-hole pairs created by the electrons will be

greater than the number of photogenerated holes. As a consequence, the highest electric field achievable within a-Se will be limited. In the case of the fabricated PI/a-Se structure, it is believed that $E<E_{max}$ for all the tested biasing voltages since no impact ionization was observed in dark and the device structure did not contain an electron blocking layer. In order to calculate E_{max}, the quantum efficiency for holes and electrons should be experimentally measured by illuminating the device from its positively and negatively biased electrodes, respectively. The details of the E_{max} calculation can be found in [53].

References

[1] A. R. Cowen, S. M. Kengyelics and A. G. Davies, "Solid-state, flat-panel, digital radiography detectors and their physical imaging characteristics," *Clin. Radiol.,* vol. 63, pp. 487-498, 2008.

[2] G. Zentai, "Photoconductor-based (direct) large-area x-ray imagers," *J. Soc. Inf. Display,* vol. 17, pp. 543-550, 2009.

[3] W. Zhao and J. A. Rowlands, "Large-area solid state detector for radiology using amorphous selenium," *Proc. SPIE: Medical Imaging,* vol. 1651, pp. 134-143, 1992.

[4] D. L. Y. Lee, L. K. Cheung and L. S. Jeromin, "New digital detector for projection radiography," in *Proc. SPIE: Medical Imaging,* 1995, pp. 237-249.

[5] N. Allec, S. Abbaszadeh and K. S. Karim, "Single-layer and dual-layer contrast-enhanced mammography using amorphous selenium flat panel detectors," *Phys. Med. Biol.,* vol. 56, pp. 5903, 2011.

[6] N. Allec, S. Abbaszadeh, A. Fleck, O. Tousignant and K. S. Karim, "K-Edge Imaging Using Dual-Layer and Single-Layer Large Area Flat Panel Imagers," *IEEE Trans. Nucl. Sci.,* vol. 59, pp. 1856-1861, 2012.

[7] S. Kasap, J. B. Frey, G. Belev, O. Tousignant, H. Mani, J. Greenspan, L. Laperriere, O. Bubon, A. Reznik and G. DeCrescenzo, "Amorphous and polycrystalline photoconductors for direct conversion flat panel X-ray image sensors," *Sensors,* vol. 11, pp. 5112-5157, 2011.

[8] C. R. Ronda, *Luminescence: From Theory to Application.* WILEY-VCH, 2007.

[9] M. J. Weber, "Inorganic scintillators: today and tomorrow," *J. Lumin.,* vol. 100, pp. 35-45, 2002.

[10] B. Liu and C. Shi, "Development of medical scintillator," *Chinese Sci. Bull.,* vol. 47, pp. 1057-1063, 2002.

[11] M. Nikl, "Scintillation detectors for x-rays," *Meas. Sci. Technol.,* vol. 17, pp. 37, 2006.

[12] H. G. Chotas, J. T. Dobbins and C. E. Ravin, "Principle of digital radiography with large-area, electronically readable detectors: a review of the basics," *Radiology,* vol. 210, pp. 595-599, 1999.

[13] C. W. E. v. Eijk, "Inorganic scintillators in medical imaging," *Phys. Med. Biol.,* vol. 47, pp. R85-R106, 2002.

[14] M. Ishii and M. Kobayashi, "Single crystal for radiation detector," *Prog. Cryst. Growth Ch.,* vol. 23, pp. 245-311, 1992.

[15] S. Tavernier, A. Gektin, B. Grinyov and W. W. Moses, *Radiation Detectors for Medical Applications.* Spinger, 2006.

[16] M. Yoshimi, T. Ishiko, K. Hattori, H. Okamoto and Y. Hamakawa, "Photocurrent multiplication in a hydrogenated amorphous silicon‐ based p‐ i‐ n junction with an a‐ SiN:H layer," *J. Appl. Phys.,* vol. 72, pp. 3186-3193, 1992.

[17] P. Bhattacharya, *Semiconductor Optoelectronic Devices.* Prentice-Hall, 1997.

[18] A. Rose, *Concepts in Photoconductivity and Allied Problems.* Interscience Publishers, 1963.

[19] G. Juška and K. Arlauskas, "Impact ionization and mobilities of charge carriers at high electric fields in amorphous selenium," *Phys. Stat. Sol. (a),* vol. 59, pp. 389-393, 1980.

[20] Canadian Institute for Health Information, http://www.cihi.ca/CIHI-ext-portal/internet/EN/TabbedContent/types+of+care/specialized+services/medical+imaging/cihi010642.

[21] J. Yorkston and J. A. Rowlands, "Flat panel detector for digital radiography," in *Handbook of Medical Imaging*, J. Beutel, H. L. Kundel and R. L. Van Metter, Eds. SPIE Press, 2000, pp. 223-328.

[22] L. W. Goldman, "Principles of CT and CT technology," *J. Nucl. Med. Technol.,* vol. 35, pp. 115-128, 2007.

[23] I. A. Cunningham and P. F. Judy, "Computed tomography," in *The Biomedical Engineering Handbook*, J. D. Bronzino, Ed. CRC Press LLC, 2000.

[24] T. G. Flohr, S. Schaller, K. Stierstorfer, H. Bruder, B. M. Ohnesorge and U. J. Schoepf, "Multi–Detector Row CT Systems and Image-Reconstruction Techniques1," *Radiology,* vol. 235, pp. 756-773, 2005.

[25] D. J. Dowsett, P. A. Kenny and R. E. Johnston, *The Physics of Diagnostic Imaging.* London: Hodder Arnold, 2006.

[26] M. Korner, C. H. Weber, S. Wirth, K. Pfeifer, M. F. Reiser and M. Treitl, "Advances in Digital Radiography: Physical Principles and System Overview," *Radiographics,* vol. 27, pp. 675-686, 2007.

[27] D. Jaffray and J. Siewerdsen, "Cone-beam computed tomography with a flat-panel imager: initial performance characterization," *Med. Phys.,* vol. 27, pp. 1311, 2000.

[28] D. A. Jaffray, J. H. Siewerdsen, J. W. Wong and A. A. Martinez, "Flat-panel cone-beam computed tomography for image-guided radiation therapy," *Int. J. Radiat. Oncol.,* vol. 53, pp. 1337-1349, 2002.

[29] R. Gupta, A. C. Cheung, S. H. Bartling, J. Lisauskas, M. Grasruck, C. Leidecker, B. Schmidt, T. Flohr and T. J. Brady, "Flat-Panel Volume CT: Fundamental Principles, Technology, and Applications1," *Radiographics,* vol. 28, pp. 2009-2022, 2008.

[30] S. Hung, C. Lin, W. Guo, F. Chang, C. Luo, M. M. Teng and C. Chang, "Toward the Era of a One-Stop Imaging Service Using an Angiography Suite for Neurovascular Disorders," *BioMed Research International,* vol. 2013, pp. 873614, 2013.

[31] S. Sauerbier, F. Duttenhoefer, E. Sachlos, J. Haberstroh, C. Scheifele, K. Wrbas, P. J. Voss, E. Veigel, J. Smedek and P. Ganter, "Evaluation of bone substitute materials: Comparison of flat-panel based volume CT to conventional multidetector CT," *Journal of Cranio-Maxillofacial Surgery,* 2013.

[32] S. Kasap, J. B. Frey, G. Belev, O. Tousignant, H. Mani, L. Laperriere, A. Reznik and J. A. Rowlands, "Amorphous selenium and its alloys from early xeroradiography to high resolution X-ray image detectors and ultrasensitive imaging tubes," *Phys. Stat. Sol. (B),* vol. 246, pp. 1794-1805, 2009.

[33] W. Que and J. A. Rowlands, "X-ray photogeneration in amorphous selenium: Geminate versus columnar recombination," *Phys. Rev. B,* vol. 51, pp. 10500-10507, 1995.

[34] D. M. Pai and R. C. Enck, "Onsager mechanism of photogeneration in amorphous selenium," *Phys. Rev. B,* vol. 11, pp. 5163-5174, 1975.

[35] J. Mort and D. M. Pai, *Photoconductivity and Related Phenomena.* Elsevier, 1976.

[36] G. Belev and S. O. Kasap, "Amorphous selenium as an X-ray photoconductor," *J. Non-Cryst. Solids,* vol. 345, pp. 484-488, 2004.

[37] M. Yunus, "Monte Carlo modeling of the sensitivity of x-ray photoconductor," *Masters Dissertation, University of Saskatchewan,* pp. 49, Apr. 2005.

[38] S. M. Sze and K. K. Ng, *Physics of Semiconductor Devices.* John Wiley & Sons, 2007.

[39] C. Vautier, D. Carles and C. Viger, "Localized states in the gap of amorphous selenium," in *International Conference on the Physics of Selenium and Tellurium,* 1979, pp. 219-221.

[40] J. L. Hartke, "Drift mobilities of electrons and holes and space-charge-limited current in amorphous selenium films," *Phys. Rev.,* vol. 125, pp. 1177-1192, 1962.

[41] K. C. Kao and W. Hwang, *Electrical Transport in Solids: With Particular Reference to Organic Semiconductors.* Pergamon Press (Oxford and New York), 1981.

[42] G. Pfister and A. I. Lakatos, "One-Carrier and Two-Carrier Steady-State Space-Charge-Limited Currents in Amorphous Selenium Films," *Phys. Rev. B,* vol. 6, pp. 3012-3018, 1972.

[43] R. E. Johanson, S. O. Kasap, J. Rowlands and B. Polischuk, "Metallic electrical contacts to stabilized amorphous selenium for use in X-ray image detectors," *J. Non-Cryst. Solids,* vol. 227-230, pp. 1359-1362, 1998.

[44] B. Polischuk, Z. Shukri, A. Legros and H. Rougeot, "Selenium direct converter structure for static and dynamic x-ray detection in medical imaging applications," *Proc. SPIE,* vol. 3336, pp. 494-504, 1998.

[45] S. A. Mahmood, M. Z. Kabir, O. Tousignant, H. Mani, J. Greenspan and P. Botka, "Dark current in multilayer amorphous selenium x-ray imaging detectors," *Appl. Phys. Lett.,* vol. 92, pp. 223506-1-223506-3, 2008.

[46] C. Haugen, S. O. Kasap and J. Rowlands, "Charge transport and electron-hole-pair creation energy in stabilized a-Se x-ray photoconductors," *J. Phys. D: Appl. Phys.,* vol. 32, pp. 200-207, 1999.

[47] H. Scher and E. W. Montroll, "Anomalous transit-time dispersion in amorphous solids," *Phys. Rev. B,* vol. 12, pp. 2455-2477, 1975.

[48] M. Abkowitz and D. M. Pai, "Photoelectronic behavior of a-Se and some a-Se: As alloys in their glass transition regions," *Phys. Rev. B,* vol. 18, pp. 1741-1750, 1978.

[49] G. Juška and K. Arlauskas, "Impact ionization and mobilities of charge carriers at high electric fields in amorphous selenium," *Phys. Stat. Sol. (a),* vol. 59, pp. 389-393, 1980.

[50] J. B. Frey, G. Beleve, O. Tousignant, H. Mani, L. Laperriere, A. Reznik, J. A. Rowlands and S. O. Kasap, "Amorphous selenium and its alloys from early xeroradiography to high resolution X-ray image detectors and ultrasensitive imaging tubes," *Phys. Stat. Sol. (B),* vol. 246, pp. 1794-1805, 2009.

[51] N. Mail, P. O'Brien and G. Pang, "Lag correction model and ghosting analysis for an indirect conversion flat panel imager," *J. Appl. Clin. Med. Phys.,* vol. 8, pp. 137-146, 2007.

[52] B. Zhao and W. Zhao, "Temporal performance of amorphous selenium mammography detectors," *Med. Phys.,* vol. 32, pp. 128-136, 2005.

[53] G. Juška and K. Arlauskas, "Feature of hot carriers in a-Se," *Phys. Stat. Sol. (a),* vol. 77, pp. 387-391, 1983.

[54] K. Tanioka, J. Yamazaki, K. Shidara, K. Taketoshi, T. Kawamura, S. Ishioka and Y. Takasaki, "An avalanche-mode amorphous Selenium photoconductive layer for use as a camera tube target," *IEEE Electron Device Lett.,* vol. 8, pp. 392-394, 1987.

[55] E. Maruyama, "Amorphous Built-in-Field Effect Photoreceptors," *Jpn. J. Appl. Phys.,* vol. 21, pp. 213-223, 1982.

[56] K. Tanioka, "High-Gain Avalanche Rushing amorphous Photoconductor (HARP) detector," *Nucl. Instrum. Meth. A,* vol. 608, pp. S15-S17, 9/1, 2009.

[57] B. J. M. Lui, D. C. Hunt, A. Reznik, K. Tanioka and J. A. Rowlands, "X-ray imaging with amorphous selenium: Pulse height measurements of avalanche gain fluctuations," *Med. Phys.,* vol. 33, pp. 3183-3192, 2006.

[58] M. M. Wronski, "Development of a flat panel detector with avalanche gain for interventional radiology," *Ph. D. Dissertation, University of Toronto,* 2009.

[59] M. M. Wronski, W. Zhao, A. Reznik, K. Tanioka, G. DeCrescenzo and J. A. Rowlands, "A solid-state amorphous selenium avalanche technology for low photon flux imaging applications," *Med. Phys.,* vol. 37, pp. 4982-4985, 2010.

[60] A. Reznik, W. Zhao, Y. Ohkawa, K. Tanioka and J. Rowlands, "Applications of avalanche multiplication in amorphous selenium to flat panel detectors for medical applications," *J. Mater. Sci.-Mater. El.,* vol. 20, pp. 63-67, 2009.

[61] A. Reznik, S. Baranovskii, O. Rubel, K. Jandieri, S. Kasap, Y. Ohkawa, M. Kubota, K. Tanioka and J. Rowlands, "Avalanche multiplication in amorphous selenium and its utilization in imaging," *J. Non-Cryst. Sol.,* vol. 354, pp. 2691-2696, 2008.

[62] T. Watabe, M. Goto, H. Ohtake, H. Maruyama, M. Abe, K. Tanioka and N. Egami, "New signal readout method for ultrahigh-sensitivity CMOS image sensor," *IEEE Trans. Electron Devices,* vol. 50, pp. 63-69, 2003.

[63] S. Kasap, J. A. Rowlands, S. D. Baranovskii and K. Tanioka, "Lucky drift impact ionization in amorphous semiconductors," *J. Appl. Phys.,* vol. 96, pp. 2037-2048, 2004.

[64] V. I. Arkhipov and S. O. Kasap, "Is there avalanche multiplication in amorphous semiconductors?" *J. Non-Cryst. Solids,* vol. 266-269, pp. 959-963, 2000.

[65] A. Reznik, S. D. Baranovskii, O. Rubel, G. Juska, S. O. Kasap, Y. Ohkawa, K. Tanioka and J. A. Rowlands, "Avalanche multiplication phenomenon in amorphous semiconductors: Amorphous selenium versus hydrogenated amorphous silicon," *J. Appl. Phys.,* vol. 102, pp. 053711, 2007.

[66] O. Rubel, S. D. Baranovskii, I. P. Zvyagin, P. Thomas and S. O. Kasap, "Lucky-drift model for avalanche multiplication in amorphous semiconductors," *Phys. Stat. Sol. (C),* vol. 1, pp. 1186-1193, 2004.

[67] G. Belev, "Electrical properties of amorphous selenium based photoconductive devices for application in x-ray image detector," *Ph D Dissertation, University of Saskatchewan,* 2007.

[68] A. K. Bandyopadhyay and L. C. Ming, "Pressure-induced phase transformations in amorphous selenium by x-ray diffraction and Raman spectroscopy," *Phys. Rev. B,* vol. 54, pp. 12049-12056, 1996.

[69] R. E. Tallman, B. A. Weinstein, A. Reznik, M. Kubota, K. Tanioka and J. A. Rowlands, "Photo-crystallization in a-Se imaging targets: Raman studies of competing effects," *J. Non-Cryst. Sol.,* vol. 354, pp. 4577-4581, 2008.

[70] S. O. Kasap and G. Belev, "Progress in the science and technology of direct conversion X-ray image detectors: The development of a double layer a-Se based detector," *J. Optoelectron. Adv. Mat.,* vol. 9, pp. 1-10, 2007.

[71] J. B. Frey, G. Belev, O. Tousignant, H. Mani, L. Laperriere and S. O. Kasap, "Dark current in multilayer stabilized amorphous selenium based photoconductive x-ray detectors," *J. Appl. Phys.,* vol. 112, pp. 014502-014502-9, 2012.

[72] B. Polischuk, "Direct conversion digital X-ray detector with inherent high voltage protection for static and dynamic imaging," U. S. Patent 6 353 229, Mar. 5, 2002.

[73] L. Cheung and Z. Jing, "Amorphous selenium flat panel x-ray imager for tomosynthesis and static imaging," U. S. Patent 7 303 308, Dec. 4, 2007.

[74] K. Ogusu, O. Nakane, Y. Igasaki, Y. Okamura, S. Yamada and T. Hirai, "Advanced a-Se film with high sensitivity and heat resistance for x-ray detectors," *Proc. SPIE: Medical Imaging,* vol. 7258, pp. 72583M, 2009.

[75] G. Zentai, L. Partain, M. Richmond, K. Ogusu and S. Yamada, "50 µm pixel size a-Se mammography imager with high DQE and increased temperature resistance," *Proc. SPIE: Medical Imaging,* vol. 7622, pp. 762215, 2010.

[76] F. Nariyuki, S. Imai, H. Watano, T. Nabeta and Y. Hosoi, "New development of large-area direct conversion detector for digital radiography using amorphous selenium with a C60-doped polymer layer," *Proc. SPIE: Medical Imaging,* vol. 7622, pp. 762240, 2010.

[77] I. H. Campbell, "Improving the spectral response of amorphous selenium Se photodetectors using organic semiconductor," *Appl. Phys. Lett.,* vol. 4, pp. 063303-063303-3, 2011.

[78] G. P. Lindberg, R. E. Tallman, B. A. Weinstein, S. Abbaszadeh, K. S. Karim and A. Reznik, "Substrate- and interface-mediated photocrystallization in a-se films and multi-layers," in *Bul. Am. Phys. Soc,* 2012.

[79] S. Abbaszadeh, K. Rom, O. Bubon, B. A. Weinstein, K. S. Karim, J. A. Rowlands and A. Reznik, "The effect of the substrate on transient photodarkening in stabilized amorphous selenium," *J. Non-Cryst. Solids,* vol. 358, pp. 2389-2392, 2012.

[80] G. P. Lindberg, T. O'Loughlin, N. Gross, A. Reznik, S. Abbaszadeh, K. S. Karim, G. Belev, D. M. Hunter and B. A. Weinstein, "Raman and AFM Mapping Studies of Photo-induced Crystallization in a-Se Films: Substrate-Strain and Thermal Effects," *Can. J. Phys.,* 2013.

[81] K. Kikuchi, Y. Ohkawa, K. Miyakawa, T. Matsubara, K. Tanioka, M. Kubota and N. Egami, "Hole-blocking mechanism in high gain avalanche rushing amorphous photoconductor (HARP) film," *Phys. Stat. Sol. (C),* vol. 8, pp. 2800-2803, 2011.

[82] Y. Xu and M. A. A. Schoonen, "The absolute energy positions of conduction and valance bands of selected semiconducting minerals," *Am. Mineral.,* vol. 85, pp. 543-556, 2000.

[83] T. D. Heidel, D. Hochbaum, J. M. Sussman, V. Singh, M. E. Bahlke, I. Hiromi, J. Lee and M. A. Baldo, "Reducing recombination losses in planar organic photovoltaic cells using multiple step charge separation," *J. Appl. Phys.,* vol. 109, pp. 104502, 2011.

[84] S. A. Kafafi, "The ionization potential, electron affinity and energy gap of polyimide," *Chem. Phys. Lett.,* vol. 169, pp. 561-563, 1990.

[85] K. Wang, S. Abbaszadeh, K. S. Karim, J. A. Rowlands and A. Reznik, "Ion beam assisted deposition of a mixed cerium oxide hole blocking contact for multilayer amorphous selenium devices," in *16th Canadian Semiconductor Science and Technology Conference,* 2013.

[86] K. Tsuji, Y. Takasaki, T. Hirai and K. Taketoshi, "Impact Ionization Process in Amorphous Selenium," *J. Non-Cryst. Solids,* vol. 114, pp. 94-96, 1989.

[87] D. C. Hunt, K. Tanioka and J. A. Rowlands, "X-ray imaging using avalanche multiplication in amorphous selenium: Investigation of intrinsic avalanche noise," *Med. Phys.,* vol. 34, pp. 4654-4663, 2007.

[88] O. Bubon, G. DeCrescenzo, W. Zhao, Y. Ohkawa, K. Miyakawa, T. Matsubara, K. Kikuchi, K. Tanioka, M. Kubota, J. A. Rowlands and A. Rezik, "Electroded avalanche amorphous selenium (a-Se) photosensor," *Curr. Appl. Phys.,* vol. 12, pp. 983-988, 2012.

[89] K. Wang, C. Feng, G. Belev, S. O. Kasap and K. S. Karim, "Lateral metal–semiconductor–metal photodetectors based on amorphous selenium," *Appl. Phys. Lett.,* vol. 95, pp. 013505-013505-3, 2009.

[90] K. Wang, M. Y. Yazdandoost, R. Keshavarzi, K. Shin, C. Hristovski, S. Abbaszadeh, F. Chen, S. H. Majid and K. S. Karim, "Integration of an amorphous silicon passive pixel sensor array with a lateral amorphous selenium detector for large area indirect conversion x-ray imaging applications," *Proc. SPIE: Medical Imaging,* vol. 7961, pp. 79610V, 2011.

[91] R. Keshavarzi, K. Wang, M. Y. Yazdandoost, K. Shin, F. Chen, S. H. Majid, S. Abbaszadeh and K. S. Karim, "Performance of a prototype 32x32 pixel indirect x-ray imager based on a lateral selenium passive pixel sensor," *Proc. SPIE: Medical Imaging,* vol. 8313, pp. 83135O, 2012.

[92] S. Abbaszadeh, N. Allec, K. Wang, F. Chen and K. S. Karim, "Study of gain phenomenon in lateral metal-semiconductor-metal detectors for indirect conversion medical imaging," *Proc. SPIE: Medical Imaging,* pp. 79614P, 2011.

[93] C. Juhasz, S. A. Vaezi-Nejad and S. O. Kasap, "Electron and hole drift mobility in amorphous selenium-based photoreceptors," *J. Imaging Sci.,* vol. 29, pp. 144-148, 1985.

[94] C. Haugen and S. O. Kasap, "Langevin recombination of drifting electrons and holes in stabilized a-Se (Cl-doped a-Se:0.3% As," *Philos. Mag. B,* vol. 71, pp. 91-96, 1995.

[95] S. A. Mahmood and M. Z. Kabir, "Dark current mechanisms in stabilized amorphous selenium based n-i detectors for X-ray imaging applications," *J. Vac. Sci. Technol. A, Vac. Surf. Films,* vol. 29, pp. 031603, 2011.

[96] S. Abbaszadeh, N. Allec, Kai Wang and K. S. Karim, "Low Dark-Current Lateral Amorphous-Selenium Metal–Semiconductor–Metal Photodetector," *IEEE Electron Device Lett.,* vol. 32, pp. 1263-1265, 2011.

[97] A. V. Kolobov, Ed., *Photo-Induced Metastability in Amorphous Semiconductor.* Germany: WILEY-VCH, 2003.

[98] A. Reznik, B. J. M. Lui, V. Lyubin, M. Klebanov, Y. Ohkawa, T. Matsubara, K. Miyakawa, M. Kubota, K. Tanioka, T. Kawai and J. A. Rowlands, "The effect of temperature on photoinduced metastability in avalanche a-Se layers," *J. Non-Cryst. Sol.,* vol. 352, pp. 1595-1598, 2006.

[99] K. Tanaka and K. Shimakawa, *Amorphous Chalcogenide Semiconductors and Related Material.* New York: Springer, 2011.

[100] A. Reznik, B. J. M. Lui, J. A. Rowlands, S. D. Baranovskii, O. Rubel, V. Lyubin, M. Klebanov, S. O. Kasap, Y. Ohkawa, T. Matsubara, K. Miyakawa, M. Kubota, K. Tanioka and T. Kawai, "Kinetics of the photostructural changes in a-Se films," *J. Appl. Phys.,* vol. 100, pp. 113506, 2006.

[101] B. A. Weinstein, R. E. Tallman, G. P. Lindberg, J. A. Rowlands, A. Reznik, M. Kubota and K. Tanioka, "Photocrystalization in a-Se film with and without As-Se buffer layers," *APS Bull. Amer. Phys. Soc.,* vol. 56, pp. Y31, 2011.

[102] K. Shimakawa, N. Nakagawa and T. Itoh, "The origin of stretched exponential function in dynamic response of photodarkening in amorphous chalcogenides," *Applied Physics Letters,* vol. 95, pp. 051908, 2009.

[103] J. O. Rawlings, S. G. Pantula and D. A. Dickey, *Applied Regression Analysis: A Research Tool.* New York: Springer, 1998.

[104] R. B. Stephens, "Stress-enhanced crystallization in amorphous selenium films," *J. Appl. Phys.,* vol. 51, pp. 6197-6201, 1980.

[105] J. M. Harnly and R. E. Fields, "Solid-state array detectors for analytical spectrometry," *Appl. Spectrosc.,* vol. 51, pp. 334A-351A, 1997.

[106] X. Zhang and V. Karanassios, "Rapid prototyping of solar-powered, battery-operated, atmospheric-pressure, sugar-cube size microplasma on hybrid, 3D chips for elemental analysis of liquid microsamples using a portable optical emission spectrometer," *Proc. SPIE,* vol. 8366, pp. 83660D, 2012.

[107] S. Weagent, V. Chen and V. Karanassios, "Battery-operated, argon–hydrogen microplasma on hybrid, postage stamp-sized plastic–quartz chips for elemental analysis of liquid microsamples using a portable optical emission spectrometer," *Anal. Bioanal. Chem.,* vol. 401, pp. 2865-2880, 2011.

[108] A. R. Hoskinson, J. Hopwood, N. W. Bostrom, J. A. Crank and C. Harrison, "Low-power microwave-generated helium microplasma for molecular and atomic spectroscopy," *J. Anal. At. Spectrom.,* vol. 26, pp. 1258-1264, 2011.

[109] C. K. Eun and Y. B. Gianchandani, "Microdischarge-Based Sensors and Actuators for Portable Microsystems: Selected Examples," *IEEE J. Quantum Electron.,* vol. 48, pp. 814-826, 2012.

[110] I. Saito, W. Miyazaki, M. Onishi, Y. Kudo, T. Masuzawa, T. Yamada, A. Koh, D. Chua, K. Soga, M. Overend, M. Aono, G. A. J. Amaratunga and K. Okano, "A transparent ultraviolet triggered amorphous selenium p-n junction," *Appl. Phys. Lett.,* vol. 98, pp. 152102-152102-3, 2011.

[111] A. K. Bhatnagar, K. V. Reddy and V. Srivastava, "Optical energy gap of amorphous selenium: Effect of annealing," *J. Phys. D: Appl. Phys.,* vol. 18, pp. L149-L153, 1985.

[112] J. Orchard, H. Y. Kim and J. T. Yeow, "Plausibility of Image Reconstruction Using a Proposed Flexible and Portable CT Scanner," *Open Med. Imag. J.,* vol. 6, pp. 1-11, 2012.

[113] F. Sauli, "GEM: A new concept for electron amplification in gas detectors," *Nucl. Instrum. Meth. A,* vol. 386, pp. 531-534, 1997.

[114] D. L. Y. Lee, "Selenium detector with a grid for selenium charge gain," *Proc. SPIE: Medical Imaging,* vol. 5745, pp. 216-222, 2005.

[115] A. H. Goldan and W. Zhao, "A field-shaping multi-well avalanche detector for direct conversion amorphous selenium," *Med. Phys.,* vol. 40, pp. 010702, 2013.

[116] S. Ghanbarzadeh, S. Abbaszadeh, M. Adachi and K. S. Karim, "Low dark current and high dynamic range a-Si:H MSM photodetector for large area medical imaging," *Proc. SPIE,* vol. 8668, pp. 86683U, 2013.

[117] S. Ghanbarzadeh, S. Abbaszadeh and K. S. Karim, "Low dark current amorphous silicon metal-semiconductor-metal photodetector for digital imaging applications," *IEEE Electron Device Lett.,* 2014.

[118] K. Wang, F. Chen, K. Shin, N. Allec and K. S. Karim, "Lateral amorphous selenium metal-semiconductor-metal photodetector for large-area high-speed indirect-conversion medical imaging applications," *Proc. SPIE,* vol. 7622, pp. 762217-762217-9, 2010.

[119] S. Mahmood, M. Kabir, O. Tousignant, H. Mani, J. Greenspan and P. Botka, "Dark current in multilayer amorphous selenium x-ray imaging detectors," *Appl. Phys. Lett.,* vol. 92, pp. 223506-223506, 2008.

[120] F. Manouchehri, M. Kabir, O. Tousignant, H. Mani and V. Devabhaktuni, "Time and exposure dependent x-ray sensitivity in multilayer amorphous selenium detectors," *J. Phys. D,* vol. 41, pp. 235106, 2008.